UNIVERSITY OF CALIFORNIA
RIVERSIDE

Enhancing Cost Effectiveness, Reliability, and Resiliency of Distributed Energy Resources-Integrated Building Microgrids

A Dissertation submitted in partial satisfaction
of the requirements for the degree of

Doctor of Philosophy

in

Electrical Engineering

by

A S M Jahid Hasan

September 2022

Dissertation Committee:
Dr. Sadrul Ula, Co-Chairperson
Dr. Matthew Barth, Co-Chairperson
Dr. Hamed Mohsenian-Rad

The Dissertation of A S M Jahid Hasan is approved:

_____

_____

Committee Co-Chairperson

_____

Committee Co-Chairperson

University of California, Riverside

Acknowledgement

First and foremost, I would like to thank almighty Allah. Then my sincerest gratitude is towards my Ph.D. supervisor Dr. Sadrul Ula. He guided me throughout these past five years with highly valuable knowledge and research direction. The suggestions I received from him were not limited to academics only but also encompasses a lot of aspects of life. He constantly supported me from day one of my time as a PhD student. His research outlook has helped me a lot to improve my analytical approach. I am truly grateful to do research under the supervision of a person with such a brilliant mind and wonderful soul.

I would like to thank the co-chairperson of my committee Dr. Matthew J. Barth for his insightful inputs towards my dissertation. I would like to thank my dissertation committee member Dr. Hamed Mohsenian-Rad. I learned a lot from them by attending multiple courses they taught and working on different research projects with them. I am also grateful to my co-author and research partner Jubair Yusuf for his help, support and motivation. I would also like to thank other members of our research group Luis Enriquez-Contreas and Henry Gomez for being immensely helpful.

I would like to thank my mother Ferdousi Khanam, who is the biggest inspiration for me to do a Ph.D. I would like to remember my deceased father AKM Shafiqul Islam, who I believe would be very proud of my PhD. I would like to thank my elder brothers Didarul Hasan and Zaved Hasan, who have tutored me and paved the way to become an engineer. I would like to thank my sisters, Farzana Islam and Sultana Islam for their constant love and support. Last but not the least, I would like to thank my loving wife Marzia Israt, who has been tremendously supportive and patient.

Dedicated to my family.

ABSTRACT OF THE DISSERTATION

Enhancing Cost Effectiveness, Reliability, and Resiliency of Distributed Energy Resources-Integrated Building Microgrids

by

A S M Jahid Hasan

Doctor of Philosophy, Graduate Program in Electrical Engineering
University of California, Riverside, September 2022
Dr. Sadrul Ula, Co-Chairperson
Dr. Matthew Barth, Co-Chairperson

The ever-increasing need for energy coupled with environment concerns due to emissions from fossil fuel-based sources have created a major dilemma for experts searching for a solution. The adoption of Distributed Energy Resources (DERs) combining renewable sources such as solar, wind, and distributed storages into the grid along with energy efficiency of large consumers like commercial buildings have the potential to resolve this. Large deployment of commercial building microgrids integrated with DERs can achieve both. But high installation, operation and maintenance (O&M) costs as well as unexpected grid operational challenges emerging from them are preventing the large-scale real-world adoption and implementation. In this dissertation solutions to three aspects of these problems are offered.

First, cost optimization of commercial building microgrids with DERs is implemented from a utility tariff perspective. This effort includes developing a universal optimization framework that addresses the diversity and complexity of tariffs implemented

by utilities. Changes in tariffs are also analyzed so that users can determine the best possible scenario for them. A novel dynamic tariff is proposed that can help the utilities deal with the "Duck Curve" problem that causes grid operation challenge due to high solar penetration.

Next, a novel data-driven approach is proposed for predictive maintenance of Battery Energy Storage System (BESS), an important DER component in a commercial building microgrid. This approach uses readily available electrical and thermal property data of the BESS and applies the proposed statistical analysis to identify the bad cells in the BESS. Performance comparison of different machine learning algorithms are also compared along with the application of non-conventional features for better state of charge (SOC) estimation results.

Finally, a methodology is developed for sustaining a commercial building microgrid in an islanded condition through the incorporation of several DERs including Vehicle to Grid (V2G) operation of Electric Vehicles. Results from microgrid islanding operation were analyzed and validated against several outage scenarios relevant to California grid to demonstrate the effectiveness of the developed method.

Table of Contents

List of tables

List of figures

1 Introduction

1.1 Background and Motivation

The growing population and associated economic development throughout the world have created a colossal need for energy. The U.S. Energy Information Agency's (EIA) projection shows that by 2050, the energy consumption in the world would increase by nearly 50 percent [1]. Further, Greenhouse Gas (GHG) emissions have increased around 90 percent over the past century [2]. Therefore, we need a sustainable and environment friendly solution for this energy problem. Integration of renewable energy and energy efficiency is the most feasible way to achieve this sustainable goal. Governments are adopting policies that enables such a sustainable roadmap. The International Energy Agency (IEA) predicts that between 2023 and 2025, the additional generation capacity of combined solar and wind in the world will range from 130 GW to 165 GW, surpassing the capacity of generation from coal [3]. According to EIA, renewable energy sources accounted for about 12.6% of total US energy consumption and about 19.8% of electricity generation in 2020 [4]. Electricity generation from solar in the US has increase from 5 million kWh to 133 billion kWh within the last 35 years [5]. The U.S. Department of Energy's (DOE) energy efficiency programs on buildings has achieved $730 millions estimated lifetime energy savings [6].

On the other hand, this continuously increasing renewable integration has introduced new challenges to the grid operations. One such challenge is the modified shape

of the daily electricity demand exemplified in California in the shape of a “Duck Curve”. Grids in places with high solar PV penetration such as California or Hawaii face a problem with high generation ramp rate at evening hours, especially in summer. At that time the solar starts to decrease while building loads stay high due to continuing cooling demands. The net demand, which is the difference between electricity demanded by the load minus renewable generation, increases rapidly within a few hours resulting in the need for rapid ramp up of generation from other power sources. But increasing generation at this fast rate is challenging for these sources with generally inherent slower response time of thermal system. The net demand curve resembles the shape of a duck and is termed as “Duck Curve” [7]. Every year with the increasing solar penetration the CAISO’s net demand ramp rate requirement is getting worse. Table 1-1 shows the three-hour ramp rate of the duck curve (4 PM to 7 PM) on August 15 for the last four years.

Table 1-1 CAISO Net Demand Three Hour Ramp Rate

Year	Three Hour Average Ramp (MW)
2018	6,809
2019	7,680
2020	8,547
2021	9,588

The buildings sector is the highest electricity user and one of the highest total energy users in the U.S. They are responsible for 76 percent of the total electricity use and 40 percent of the total primary use [8]. Among them, commercial buildings constitute a significant portion, accounting for 35 percent of the total electricity consumption in the U.S. They also have a big impact on the environment as they are liable for 16 percent of

all the CO_2 emissions in the U.S. [9]. The U.S. Environmental Protection Agency (EPA) estimates that, on average, 30 percent of the energy used in commercial buildings are wasted. Therefore, they offer great opportunity for energy efficiency and emission reduction. Even a small reduction in energy usage of commercial buildings would have an immensely positive impact on the energy security and the environment.

One possible way to reduce this energy usage and carbon emissions is through the integration of renewable distributed energy resources (DER) into commercial buildings. US DOE defines DERs as [10],

> *"Distributed energy resources are small, modular, energy generation and storage technologies that provide electric capacity or energy where you need it. Typically producing less than 10 megawatts (MW) of power, DER systems can usually be sized to meet your particular needs and installed on site."*

Of the 133 billion kWh solar electricity generation, 31 percent came from distributed small-scale Photovoltaic (PV) generation system, most of which are installed in buildings [5]. But renewable DERs are mostly weather dependent and intermittent in nature. To make this intermittent energy available at the time of need, storage devices are used. The most common storage device is the battery energy storage systems (BESS). Commercial buildings equipped with such DERs are said to be in a "microgrid" setup. US DOE defines microgrids as [11],

"a group of interconnected loads and distributed energy resources within clearly defined electrical boundaries that acts as a single controllable entity with respect to the grid. A microgrid can connect and disconnect from the grid to enable it to operate in both grid-connected or island mode."

Microgrids can help to increase energy efficiency by optimization and coordination of DERs and by reducing transmission and distribution losses through localization of generation with demand. They also provide system resiliency by ensuring supply of power to the critical loads and controlling power quality and reliability at a local level, while facilitating grid operations through involving customers with demand side management (DSM) and providing ancillary services like voltage regulation, frequency regulation, spinning reserve, etc. [11].

While the renewable DERs have significantly low impact on the environment, they may not offer the lowest cost electricity generation option. These DERs can comprise 30-40% of the total microgrid setup cost [11]. The installation cost of renewable DERs can range from $1,000 to $13,000 per kW. The operation and maintenance (O&M) cost is dependent on the DER size with variable O&M cost ranging between $0.002-$0.03/kWh and fixed O&M cost around $10/kW-year [10,12].

Optimal operation of DERs in microgrids can make them profitable for the customers within their lifetime. Proper and low-cost operation and maintenance of the DERs is also desired for their profitable outcome besides their safe and reliable operation.

Thus, optimal DER operation along with low-cost O&M solutions are essential for achieving the sustainable energy goals.

1.2 Contributions

Commercial building microgrids equipped with DERs can perform the demand management and energy efficiency on their own along with providing grid ancillary services. However, for widespread adoption of microgrids in commercial buildings, cost effectiveness and improved maintenance of DER assets are necessary. The key contributions of this dissertation are:

- A tariff-unified framework has been developed for load optimization of commercial building microgrids with DERs. This effort includes designing a universal optimization cost function that is applicable to any type of commercial utility tariff exercised on commercial buildings. Different possible changes in utility tariffs have been identified and their impacts on the optimization of commercial building loads have also been analyzed.
- A data-driven approach has been employed for the maintenance and monitoring of a BESS, an essential DER component. A novel predictive maintenance method based on the statistical analysis of the electrical and thermal properties of the BESS cells has been proposed. Performance of different machine learning methods are compared to determine the best method to estimate BESS state-of-charge (SOC). The use of selected non-conventional features along with conventional features has been examined to see how much they can boost the performance of SOC estimation.

- A methodology is developed for a real-world demonstration of microgrid islanding experiment and then performed on a commercial building microgrid with DERs. The microgrid testbed has a state-of-the-art setup containing bidirectional grid-interactive and grid-forming BESS, PV generation with curtailment ability, and a Vehicle to Grid (V2G) inverter. This unique setup with the exceptional capabilities of the system components have been leveraged for designing experiment swhere real system limitations and constraints are taken into account. The experiment results are compared with different outage scenarios in the major IOU territories of California for validation of microgrid resiliency.

1.3 Organization

This dissertation is organized as follows: Chapter 2 provides the research background on the related topics of this dissertation and performs literature review on them. Chapter 3 demonstrates the proposed modeling and optimization of the commercial buildings with DERs and analyzes the different impacts on the optimization results due to changes in utility tariffs. Chapter 4 describes the proposed predictive maintenance method to identify the faulty cells in BESS using the statistical analysis of electrical and thermal properties and the comparative analysis of machine learning methods for SOC estimation for monitoring. Chapter 5 depicts the islanding experiment of a commercial building with DERs and validates the results using resiliency indices. Chapter 6 draws the conclusions of this dissertation, lists the publications that came out of this research, and discusses possible future work that can be done to extend this research.

2 Research Background and Literature Review

As discussed in the previous chapter, renewable energy and energy efficiency are helping to reach the sustainability goals and combat climate change. Microgrids and DERs are playing a key role in that aspect of renewable integration and energy efficiency. But high installation and O&M costs are creating an obstacle to those. Furthermore, inadequate number of real microgrid deployments and insufficient available experimental data are making achieving sustainability goals even more challenging. Researchers are working on enhancing the savings by optimizing building microgrid loads through controlled DER operation, with grid or as an island isolated from grid, using both simulation and practical demonstrations. The upcoming sections of this chapter discusses the contemporary research works on these aspects with a view to identifying the unaddressed issues and scope of improvements.

2.1 Optimization of Commercial Building Loads

The nature and pattern of electrical loads have changed significantly over the years. The utilities have developed numerous types of tariffs accordingly that would facilitate their operation with the existing generation, transmission, and distribution resources. Concepts such as Time of Use (TOU) and different types of energy and demand charges have been introduced to mitigate the limitations of these resources. Additionally, highly distinctive load patterns and consumption amount have motivated the utilities to introduce separate tariffs for residential and commercial sectors.

The recent adoption of high renewable penetration into the grid has made the change in electrical load even more severe and rapid. To accommodate these fundamental

and long-lasting changes both TOU time periods and rate structure are being changed by various utilities. For example, the highest cost On-Peak period used to be 12 noon to 6 PM which is now shifted to 4 PM to 9 PM in response to high solar production in California. Innovative tariffs such as Critical Peak Pricing (CPP) are introduced to encourage the customers reduce their regular consumption on specific hours of specific days experiencing higher grid stress. Customers are being offered choices between options with high energy charge, low demand charge or high demand charge, low energy charge. Additionally, these tariffs go through changes in prices frequently.

As mentioned in chapter 1, commercial buildings are one of the largest electricity users in the U.S. as they consume about 35% of the total electricity consumption [9]. As one of the largest electricity users in the U.S., commercial building loads offer great potential for optimization with the help of distributed energy resources (DERs) such as solar generation and battery energy storage systems (BESS) that would largely benefit both the customers behind the meter and utility operators. But these extremely diverse and highly complex tariffs create a major challenge for formulating appropriate optimization strategy for such DER integrated buildings. Moreover, changes that the tariffs go through can have significant impact over the DER optimization of building loads that eventually lead to DER investment and grid operation decisions of customers and utilities, respectively. Therefore, in order to design an optimal strategy for reducing building loads with DERs, utility tariff is an important aspect that needs to be considered. A universal objective function that captures all the different components of these tariffs can be highly beneficial to reduce the complexity of optimization that arises with the diversity of the

tariffs. A universal objective function that captures all the different components of these tariffs can be highly beneficial to reduce the complexity of optimization that arises with the diversity of the tariffs.

Many research works have been done on the optimization of the building or other loads using DERs such as solar generation, BESS, and electric vehicles (EV). Minimizing the energy cost of the building-integrated microgrid is the main objective in most of the literature. Two-layer optimization is performed on a commercial building microgrid that minimizes utility billing cost through optimal BESS scheduling and investment cost through optimal BESS sizing [13]. Thermal modeling and interactive load management of buildings through bidirectional information exchange with grid is shown in [14]. The compromise between user comfort and energy optimization is executed for commercial buildings in terms of electricity prices to provide least cost solutions regardless of environment conditions [15-18]. Deployment of vehicle-to-grid (V2G) strategies with coordinated EV charging on commercial building load optimization are assessed for different charging levels and tariffs from different utilities [19-21]. However, all these works deal with TOU energy costs only. While most commercial tariffs include demand cost which charges for the peak demand that occurs within the whole billing month or a specific period of the day within the billing month.

Demand charges are also analyzed in a limited number of works. Effects of the tariffs on the optimal PV generation sizing and economic feasibility of different BESS technologies are also shown for commercial building loads [22-24]. Optimal BESS dispatch strategy is explored for commercial buildings with various types of tariffs [25-

27]. Bi-level optimization is executed to achieve electricity cost reduction by coordinated BESS dispatch and temperature setpoint control of a commercial building [25]. Break-even analysis of a BESS integrated to a commercial building is presented with comparison to tariffs from two different utilities [26]. Results of electricity cost savings optimization are analyzed to attain the ideal BESS ratings for a commercial tariff user [27]. Nonlinear energy conversion processes of multi-energy systems (MES) have been modeled as piece-wise linear process and then used to optimize the utility costs of building loads along with possible carbon tax costs [28]. The tariff types used in these works are diverse. TOU energy rate with a single time independent demand charge is used in [13], TOU energy charge with TOU demand charge is applied in [12, 14, 15, 17], TOU energy charge with both TOU demand and time independent demand charge is adopted in [16] and flat energy charge with a time independent demand charge is exercised in [11]. These works handle the optimizations using various unrelated approach, thereby, necessitating an optimization fuunction that is able to deal with these varying demand charges in a consistent way.

CPP has been introduced by the utilities to provide monetary rewards to the consumers for reducing their usage during grid congestion. The impacts of V2G on commercial buildings are investigated during CPP events [29]. However, only the effect of a high CPP energy rate is presented in the paper during the CPP event hours while the benefits derived from lower demand charge at non-CPP event hours are not shown.

Efforts have been placed on designing new tariffs based on the modification of the current ones to achieve deeper interactions between customers and utilities and better grid management. In [30-31], sensitivity analysis of net grid power with maximum demand

charge is performed to find a suitable tariff pricing that maximizes customer profit and grid capacity release. Incentive pricing to maximize the benefits from participating in energy communities are also studied [32-33]. A fair pricing mechanism based on forecasted power demand is used to reduce bills for low energy consumers [34]. Adjustment of tariff levels is also explored to increase the penetration of DER [35]. A segmented energy tariff is designed to flatten the load demand profile [36]. But these proposed electricity tariffs are modified over and compared to TOU energy charges alone or TOU energy charges with a single time independent peak demand charge. Without comparing them to the other major rate categories that are offered by most utilities, the potential benefit of these tariffs will not be fully explored. This comparison can be performed easily through a universal cost function.

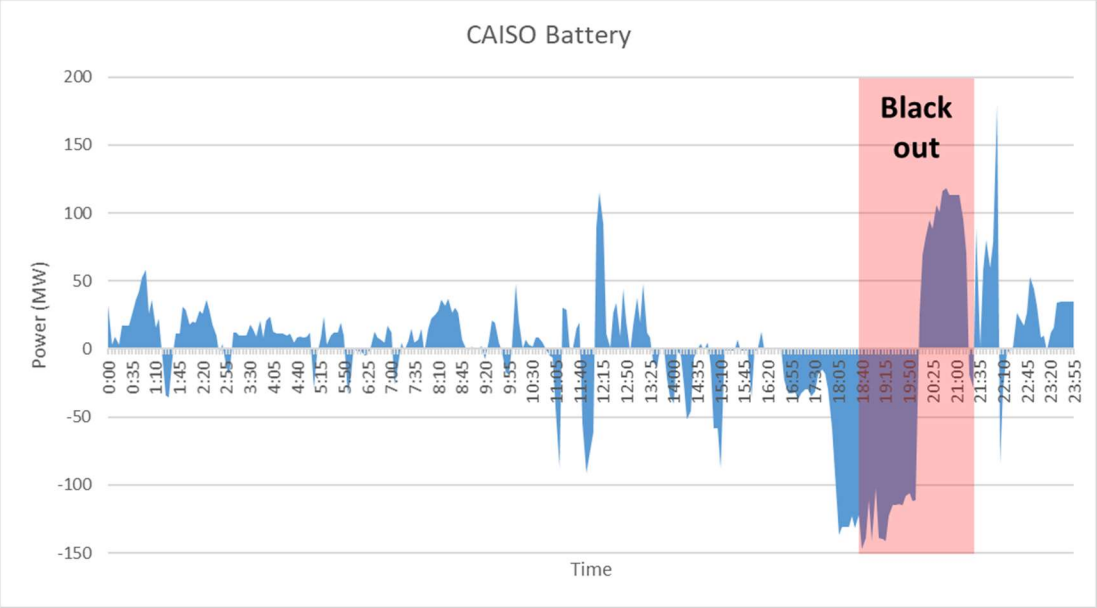

Figure 2-1 CAISO Battery Plots on a Blackout Day (08-14-2020)

In the summer of 2020, California saw an upsurge in the electricity demand due to the extreme and long duration heat waves. The Duck Curve problem on these hottest days in California becomes more severe. As the installed generation capacity was unprepared and unable to satisfy this peak demand and ramp rate requirements, CAISO declared a Stage 3 power emergency and directed the utilities to shed their loads in a rotating manner [37-38]. Though California being a leading state in the U.S. for the deployment of DERs, lack of proper operational strategy is noticeable when these type of situation arises. Figure 2-1 shows the aggregated battery charge and discharge plot from the CAISO during one of the rotating blackout days (08-14-2020) [39]. Table 2-1 shows the information about the customers of different IOUs under CPUC jurisdiction that were affected by the blackout on that day [40].

Table 2-1 CPUC Jurisdictional Customers Affected by 08-14-2020 Blackout

Utility	No. of Customers	CAISO Initiated Rotating outage (MW)	IOU Actual Response (MW)	Time (min)	Start	Finish
Southern California Edison (SCE)	132,000	400	400	63	6:56 PM	7:59 PM
Pacific Gas and Electric (PG&E)	300,600	460	588	150	6:38 PM	9:08 PM
San Diego Gas and Electric (SDG&E)	59,000	71.6	84	15-60		

While the lack of proper operational strategy can be seen from the arbitrary charge and discharge patterns of figure 2-1 throughout the day, the higher discharging mode at about 6 PM (18:00 hrs) is in response to CAISO's dispatch of demand response. However, batteries immediately went into charging mode at 7:50 PM even though PG&E's blackout continued till 9:08 PM as listed in table 2-1. Therefore, to satisfy grid requirements better, a coordinated operation of the battery and other DER assets is required. It is possible to design a new tariff for the large commercial users with BESS and other DERs, so that the cost optimization of the net load can assist the utilities in adjusting their operations on high demand days besides creating producing savings for the users, thereby avoiding similar blackouts in the future.

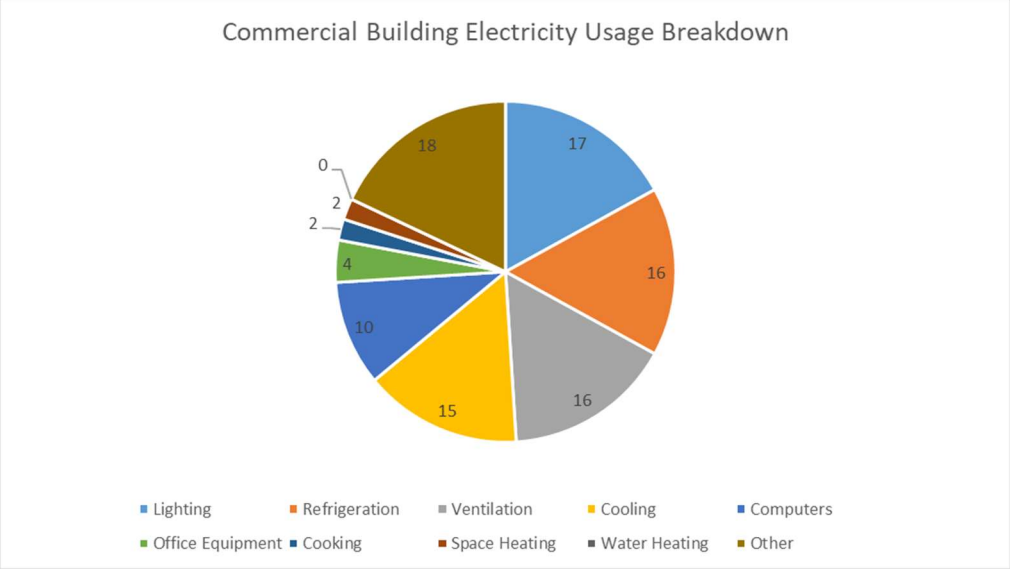

Figure 2-2 Commercial Building Electricity Usage Breakdown

Figure 2-1 shows the electricity usage breakdown in commercial buildings [41]. As we can see heating, cooling and ventilation require a significant part of total electricity usage in commercial buildings, about 33 percent. HVAC stands for Heating, ventilation

and air conditioning. HVAC is used for controlling the environmental comfort (temperature, humidity and air quality) of indoor spaces by using the flow of air. According to the Pacific Gas and Electric, 45% of residential and 54% of commercial Investor-Owned Utility (IOU) summer peak demand is caused by HVAC air conditioning loads in California. As space heating and cooling comprises a large portion commercial electricity use, HVAC has great potential for energy saving through optimization. A slight reduction in HVAC load will offer a significant savings in electricity use compared to other loads.

A fair amount of research on building energy optimization have focused intensively on HVAC optimization. Several household loads, which are time shiftable, have been modeled along with the activity detection using machine learning. Then the aggregated load has been optimized according to the real-time pricing (RTP) for demand response in [42]. But their consideration of HVAC loads was not based on any model rather some measurements on an actual HVAC unit. Manganelli et al. [43] studied the potential of controlling HVAC and other smart appliances to get a flexible load profile in a common electrical node of a microgrid connecting one or multiple nearly zero energy buildings (NZEB). Model predictive control (MPC) is another widely used approach for optimal control of HVACs [44-46]. Most of them have considered a linear relationship of power with temperature to model HVAC consumption. But in reality, Variable Air Volume (VAV) type HVAC units are most commonly found everywhere especially in commercial buildings, which actually has a bilinear relationship with temperature. The bilinear relationship makes the optimization problem nonconvex and previously this type of

problem was not computationally solvable. That's why modeling for VAV units has not been accomplished before to the best of the authors' knowledge.

To get around this complexity, data-driven approaches have been pursued in many recent works. One study has shown the effect of increasing the HVAC set points by 1°F-5°F over demand response event periods by showing how much energy is saved and how much the peak is reduced [47]. In [20], both internal (HVAC, lights, and plug loads) and external loads (EV, battery energy storage) are taken into account with building-integrated solar, and optimization is executed with a view to minimizing the total energy cost of the building. Here, the HVAC load was modeled with a curve fitting of temperature and power consumption data. In reference [48], based on occupancy information, temperature setpoints are obtained to achieve a Predicted Mean Vote (PMV) of zero to achieve thermal comfort and the energy saving is calculated by comparing with a base case. Neural networks are used to model HVAC consumption for optimization in references [49-50]. Reinforcement learning has recently gained attention for HVAC energy optimization [51-53].

2.2 Battery Energy Storage Systems (BESS): An Overview

Electrical Energy Storage (EES) refers to the process of converting electrical energy into a stored form that can later be converted back into electrical energy when needed. Battery Energy Storage Systems (BESS) are the most common form of EES. They store the electrical energy by converting to chemical form and then convert back to electrical form at the time of need. In 2021, a total of 1,363 energy storage projects were operational globally with 11 projects under construction. 40% of operational projects are

located in the US of which 64 percent of them belong to electrochemical technology or BESS type [54]. According to EIA, the total large-scale BESS capacity in the California is 1,022 MW and small-scale BESS capacity is 402 MW [55]. Especially over the last decade, Lithium-ion batteries have experienced a sharp decline in cost, more than 70%, due to technological advances in battery chemistry and manufacturing [56].

Higher capacity battery energy storage that interacts with the utility grid, ranging from a few hundred kilowatt-hours to hundreds of megawatt-hours, are usually referred to as utility-scale or grid-scale battery energy storage. The battery energy storage needs supplementary equipment that enables delivering or storing power to or from the grid as needed such as bidirectional inverters, control software, etc. This total package is generally referred to as Battery Energy Storage System or BESS. Over the years the potentiality of diverse functions of Utility-Scale BESS has been studied for grid integration [57-61]. These are now being deployed all over the world, with an installed capacity of more than 10 GW. Besides energy shifting and peak reduction capabilities [62-64], they are being utilized for frequency regulation [65-67], black start services [68], and providing flexible ramping [69-71] in situations such as California's duck curve. International Renewable Energy Agency (IRENA), says that by 2030, there will be a capacity growth of 44% for Utility-Scale BESS [72].

As a component of the utility grid that has increasing significance and growth, the reliability of BESS is a very crucial matter. Since BESS is composed of a large number of battery cells and even one damaged cell can compromise the reliability of the system drastically as mentioned above, each individual cell's reliability is of high importance too.

Predictive maintenance of the BESS cells using statistical analysis can offer great potential in this case. Even though bad cell identification of a BESS is critical, there are hardly any published works that focus on identifying the individual cell that may fail in the future based on analysis of real data. Most of the works have been done on the online fault detection of the whole pack [73-75]. Though one study shows the fault detection of individual cells, it is also an online detection of the fault [76]. The limitation with online fault detection is that warning is provided when the system is already operational, which is not desired for maintaining the operational integrity. Whereas predictive maintenance through statistical analysis presents the likelihood of failure of system components and can be used to easily identify the bad cells and replace them, ensuring operational integrity. Another research analyzes the fault detection of an individual cell but takes only into account electrical property while thermal perspective is completely ignored [77]. While analysis of electrical property can be useful for ensuring the proper function and performance, the thermal property can aid in ensuring a safe operation. Though they have taken a statistical approach in their work, it could have been improved through the addition of thermal property analysis. One other work tries to identify the low-capacity cells that limit the total capacity of the whole pack [78]. But their method requires a full charging and discharging cycle of the BESS, which may need interruption of regular operation for the identification. This work focuses on the electrical properties alone without considering the thermal properties, as well.

The quantity that is most used to indicate how much energy is stored at any particular moment is the battery's state of charge (SOC). But a major problem is that there

is no way to measure SOC directly. There are methods for determining SOC such as voltage-based measurement, current-based measurement, internal impedance-based measurement, etc. but these are all used with assumption that SOC changes linearly with the quantity concerned. In practice SOC does not change linearly with these quantities. Factors such as usable capacity, charge/discharge rate, temperature, cell age, self-discharge etc. also affect the SOC of battery [79]. Because of these factors there is no straightforward way that can calculate SOC directly.

Because of the nonlinear property of SOC of the batteries, machine learning methods have been used previously for calculating SOC. A significant number of works have focused on artificial neural network (ANN) for SOC calculation [80-82]. Many works have shown the effect of support vector machines (SVM) for estimating SOC [83-85]. Extreme learning machines (ELM), which uses only the feedforward neural network have also been applied in some of the works [86-88]. Another work has used K-nearest neighbor (KNN) for this purpose with particle swarm optimization [89]. One of the works here has shown that by selecting certain features or input it is possible to achieve higher accuracy [82]. They have used: current, terminal voltage, ampere hour, time average voltage, time derivative of voltage and second time derivative of voltage. This study investigates the effect of both conventional and nonconventional features. Some of the features mentioned here (present in both conventional and nonconventional) are highly correlated. Sometimes this leads to a phenomenon called multicollinearity. Ridge regression and lasso regression methods have shown to give good performance in case of multicollinearity [90-91]. But these methods have not been explored for SOC estimation.

2.3 Microgrid Testbeds and Experiments: An Overview

Microgrids are becoming popular and many microgrids have been deployed in the recent years. Of the current total 575 microgrid installation sites in the US, 80% of them have been deployed within the last decade [92]. Table in the next page shows the summary of these microgrid installations based on the technology types.

Table 2-2 Microgrid Installations in the US by Technology Type [69]

	CHP		Solar		Wind		Hydro		Non- CHP Fuel Cell		Non-CHP Combustion		Storage		Unknown	
Primary Application	**Sites**	**MW**	**Sites**	**MW**	**Sites**	**MW**	**Sites**	**MW**	**Sites**	**MW**	**Sites**	**MW**	**Sites**	**MW**	**Sites**	**MW**
Agriculture	2	4.0	9	2.2	2	1.1	-	-	1	0.03	6	2.4	9	1.2	-	-
City/Community	13	386.2	36	44.3	11	15.9	4	69.6	3	1.4	34	163.8	38	27.6	2	0.2
College/University	61	1,156.3	19	39.2	5	3.4	1	1.2	1	0.2	27	153.1	13	17.8	3	54.6
Commercial	17	92.8	35	13.3	8	0.4	1	0.1	7	12.5	160	222.7	36	17.5	1	0.3
Hospital/Healthcare	59	446.0	10	1.5	-	-	-	-	1	0.4	7	21.9	8	1.1	1	0.3
Military	15	125.5	24	124.8	6	3.2	-	-	-	-	51	650.6	21	28.1	7	24.0
Multi-Family	22	61.8	6	1.0	1	0.1	-	-	1	0.4	4	2.0	6	0.8	-	-
Public Institution	6	68.6	12	5.9	2	1.0	1	0.3	-	-	4	10.1	11	3.2	-	-
Research Facility	3	17.4	10	3.2	2	1.5	-	-	1	0.02	7	9.9	12	12.0	1	0.2
Schools (K-12)	1	0.1	26	5.0	1	0.002	-	-	-	-	-	-	25	3.8	-	-
Water Treatment/Utility	3	9.0	3	4.5	1	1.0	-	-	-	-	10	56.1	2	5.7	-	-
Other	-	-	5	3.6	-	-	-	-	-	-	3	20.0	4	0.1	-	-
Total*	**202**	**2,368**	**195**	**249**	**39**	**27**	**7**	**71**	**15**	**15**	**313**	**1,313**	**185**	**119**	**15**	**80**

These microgrids are deployed in various applications and diverse types of experiments are performed on these. Many of these state-of-the-art microgrids are installed and operating in California. Sacramento Municipal Utility District (SMUD) microgrid has been used to see the effect of high penetration renewable energy on driving point impedance and voltage regulator performance [93]. Santa Rita Jail microgrid project has demonstrated the seamless islanding capability within 8 milliseconds with application of reverse power relay and over current protection devices [94]. It has also made many energy efficiency improvements to reduce peak load. The University of California-Irvines' campus microgrid with Southern California Edison's (SCE) partnership has many DER assets of diverse nature. They are aiming to reduce the campus energy consumption by 20 percent as a part of DOE's Better Buildings Initiative. They have demonstrated the DR capability of 700 kW through their microgrid system [94]. The Borrego Springs microgrid project, supported by DOE, California Energy Commission (CEC) and San Diego Gas and Electric (SDG&E), has performed three microgrid islanding tests. These tests vary in number of circuits, from one to three and duration of the experiment, from one to four hours [95]. Alcatraz island is one of the largest microgrid in the US. This microgrid, separated from the mainland grid connections has 305 kW of solar, 1,920 kWh of BESS, 2 diesel generators and 8 inverters of 100 kW each, all connected with a central controller. This microgrid has achieved a fuel consumption reduction of 45 percent which has been replaced with power generated from solar PV system [96].

Some other microgrids worthy of mention outside of California are Fort Collins, Fort Carson microgrids of Colorado and Illinois Institute of Technology's microgrid. The

first two primarily take part in peak reduction and islanding tasks, the last one has multiple capabilities ranging from building DR participation, automatic system reconfiguration with Volt-Var management, service restoration, emergency response and integration of different types of DERs [94].

Theoretical and simulation-based research works on microgrids can be found in bulk numbers. But real-world demonstrations present the practical challenges that are not apparent on theoretical or simulation-based works. Though there are many real-world demonstrations of these microgrids being performed now, it is still an emerging technology. More experiments must be designed using these real-world microgrids to understand and overcome the practical challenges associated with them.

The rotating blackouts of August 2020, first since 2001, showed that California's grid infrastructure is not strong enough to deal with these peak demands. Another problem faced by California is the old transmission and distribution lines causing fires during strong, dry windy conditions by conductors touching each other. Utilities are forced to shut power to these lines by using Public Safety Power Shutdowns (PSPS) approved by the regulators.

As grid infrastructure may need significant amounts of both time and resources to upgrade, microgrids can meanwhile help to ameliorate this condition. A microgrid equipped with proper renewable generation and energy storage with ability to island from the utility grid can sustain through these types of rotating blackouts and PSPS. This resiliency of microgrids can be further augmented by use of Vehicle to Grid (V2G) power

transfers. Recently V2G has garnered increased attention due to the higher sales and use of environmental friendly electric vehicles (EV).

Recent literatures show a fair amount of works done with V2G and microgrids. While [97] discusses the potentiality of V2G to regulate the frequency of microgrids, they do not present any cases where V2G was actually used to regulate the frequency of a microgrid. A work showed the impacts of EV penetration of V2G on voltage and frequency of a microgrid [98]. But it was a simulation work where the assumptions of solar and wind power generation does not reflect real world characteristics. Another study presented the effects of different charging/discharging strategies of EV's on microgrid loads [99]. Though the data is from a real microgrid, the work simulated the results by scaling the load to 1/15 of it's original value to show the effects. An experimental work investigated the power quality issues of integrating V2G to a microgrid, but the demonstration was lab-scale rather than an actual microgrid [100]. An actual design and implementation of a microgrid with V2G was shown in details in [101], but the vehicles used here were not EV's. They used engines of military vehicles to run transmission-integrated generators (TIG), which were used as the source of V2G. Another work discusses their system architecture and control strategy of their real microgrid system with V2G but does not show any results [102]. Two real microgrid systems of significant size located on two islands, with provision for V2G is described in two separate publications. While one discussed the optimal sizing of microgrid [103], other discussed the possibilities of a Virtual Power Plant (VPP) [104]. Neither of them show any results related to V2G operation in their microgrids. Real EV charging data for a microgrid testbed has been analyzed and the impacts are

presented in [105]. But the grid to vehicle or G2V impacts were the main focus of the study. Much more attention is needed to be paid to the impacts of V2G on a microgrid due to the potentiality of V2G as an essential component of microgrids.

3 Modeling and Optimization of Distributed Energy Resources (DER) Integrated Commercial Building Microgrids

3.1 Background and Problem Statement

From the discussions in section 2.1 of the previous chapter, we can see that there are ample research works on the electricity cost optimization of building loads using DERs. However, they have overlooked to address the fact that there are numerous tariffs of diverse types that require distinct optimization objective function based on their type. These works only focus on one or at most two types of tariffs for their optimization. Much attention is needed on this topic since an optimization strategy for one type of tariff will not be suitable for the other types and may end up incurring a higher non-optimal cost. One may ask several questions in terms of the tariffs and optimization: 1) How can we address the diversity of tariffs when formulating an optimization strategy for buildings equipped with DERs such as solar and BESS? 2) How various tariff components impact the costs and savings from the optimization of different buildings? 3) How different changes in tariffs impact the results of the optimization? This chapter of the dissertation tries to answer all these questions and bridge the gap that persist in the existing literature. Though there are a number of works that can be found on individual tariff-based optimizations, to the best of the authors' knowledge no work has been done yet on a comprehensive optimization framework that addresses the issue of this complexity and diversity of utility tariffs and aims to solve it. The author would like to emphasize that the goal of the work is not to

propose a new optimization algorithm that delivers higher precision or faster convergence, rather to address the issue of diversity of tariff types that have not been considered in prior works. For any demand management scheme to work effectively, kW demand and kWh energy costs have to reflect time sensitive value. Using average values for both demand and energy costs fails to represent the fact that each of these costs may be going through at most four different values in a day. Sections 3.2 and 3.3 deal with effects of these various aspects of commercial building load optimization with DERs. The main tasks done in these two sections are listed below:

1) Classifying commercial tariffs to universal types by reviewing tariffs from multiple utilities and deriving convex optimization objective function for each type,

2) Proposing a comprehensive framework for building load optimization using DERs through derivation of a universal cost function, ubiquitous to available commercial tariffs, and

3) Performing impacts analysis of different changes in tariffs to examine their level of influence on optimization results, study the observations and proposing a modified tariff that improves upon existing ones over desired benefits.

This work can help on making investment decisions or resource planning for the commercial building owners and help utilities to develop improved tariffs for better grid operations. Researchers active in this field can benefit by utilizing the optimization formulation presented here that considers the diversity of commercial tariff types.

The data-driven approach for HVAC load optimization in other research works is has been discussed in chapter 2. The problems associated with data-driven approaches for

HVAC load optimization in commercial buildings have also been discussed. The main problem with the data driven HVAC optimization is that they are not universal and are data hungry. In addition to that, data-driven models for HVAC power consumption are mostly site-specific. We would have to collect, store, and process a huge amount of data to establish an acceptable model through a data-driven approach.

The newer versions of optimization solvers now allow nonconvex optimization with bilinear constraints. Using this ability to our advantage, we can now minimize the power consumption of widely used VAV type HVAC units. This method is developed and implemented in section 3.3 of this chapter. The main tasks performed in section 3.3 are listed below:

(i) Developing a detailed thermal model of a commercial building with VAV type HVAC units and

(ii) Formulation and solution of a nonconvex optimization problem that minimizes the overall power consumption by the building HVAC system.

3.2 Modeling and Optimization of External Electrical Load of a DER Integrated Commercial Building Microgrid

3.2.1 Methodology

In this section we summarize the methodology used in this study. The methods are described in detail in subsequent sections. Commercial tariffs currently exercised by 13 large investor-owned utilities (IOU) were reviewed to understand various types of rate schedules in the USA. Ten of them rank among the largest ones in the USA and three of them are among the largest ones in California by revenue. One is the local municipal utility

of the City of Riverside. After thorough examination they were categorized into six universal types. Despite their differences in terminologies, values, periods, etc., their core concepts remain the same, and we can cover all commercial utility tariffs with these six types. These are:

A. Multiple Time of Use (TOU) energy charges with a single time independent peak demand charge,
B. Multiple TOU energy charges with Multiple TOU demand charges,
C. Multiple TOU energy charges with both multiple TOU demand charges and a time independent peak demand charge,
D. Critical Peak Pricing (CPP) rate,
E. A simple flat energy with time independent demand charge, and
F. TOU energy charges only.

Then we derive objective functions for each of these rates and consequently the universal objective function. We integrate the universal objective function along with our system model to formulate the optimization problem. The building load and solar generation data are then used to solve the optimization problem to obtain the optimal results by following the steps of ours proposed algorithm. Figure 3-1 presents an illustrated depiction of this methodology.

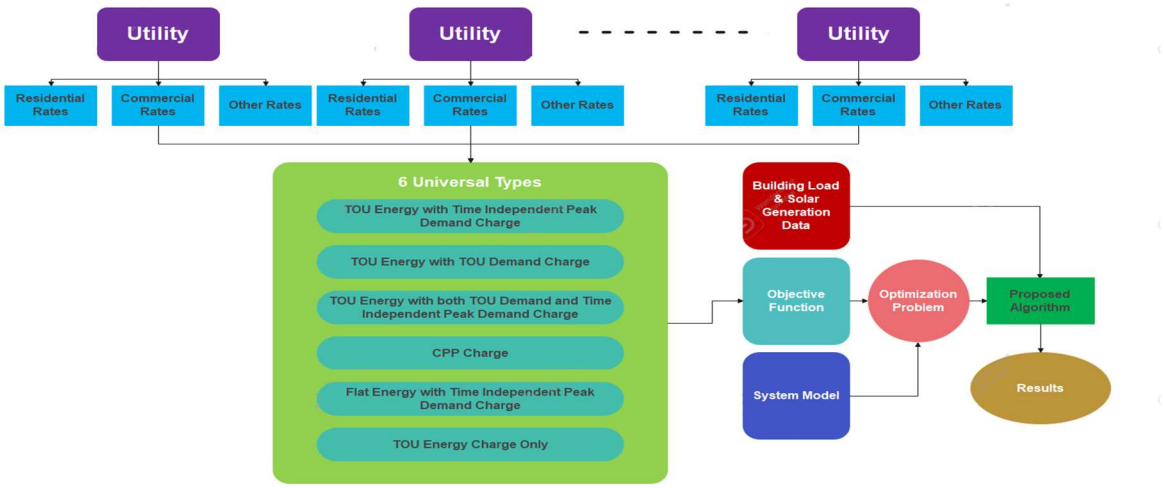

Figure 3-1 Illustration showing methodology of this study.

Data for five commercial buildings are collected for applying this optimization method. All these buildings fall under different types of commercial tariffs. These buildings differ in electrical usage and functionality. Among these three buildings, all have actual onsite solar generation and two of them have actual BESS integrated system. All the building loads that are used are actual building load data. For the buildings which did not have solar or BESS, National Renewable Energy Laboratory's (NREL) REopt was used to find the ideal solar or BESS size for the corresponding building [106]. The actual building load data and if available, actual solar data were given as inputs to obtain ideal size of solar or BESS. As the recommended sizes of solar or BESS from the simulated output value may not be commercially available in the real world, reasonably close available sizes were selected. Building 5 is a relatively small commercial building and for this one ideal BESS size was unavailable. Thus, Tesla's Powerwall's BESS size was used for this one. Then NREL's System Advisor Model (SAM) was used to generate the solar profile for the site

where a solar generation was absent [107]. These buildings are located within different utility territories in California and are eligible to participate in California Public Utility Commission's (CPUC) Net Energy Metering (NEM) program. NEM program allows customers to export excess renewable energy to the grid and reduce utility cost by receiving credits for the exported energy at the retail rate of their respective tariff. Table 3.1 summarizes the characteristics of the buildings that were used for the optimization which are: average daily energy usage, load factor (average load divided by maximum load over a billing month period), tariff type, solar and BESS size.

Table 3-1 Characteristics of the Buildings Used in Optimization

Characteristics	Building 1	Building 2	Building 3	Building 4	Building 5
Average Daily Usage (kWh)	11,223	1,660	13,451	805	108
Load Factor	0.283	0.341	0.811	0.411	0.326
If Real Solar	Yes	Yes	No	Yes	No
If Real BESS	No	Yes	No	Yes	No
Solar Size (Real)	800 kW	220 kW	-	180 kW	-
BESS Size (Real)	-	100 kW/ 500 kWh	-	100 kW/ 500 kWh	-
Solar Size (Simulated)	-	-	650 kW	-	7 kW
BESS Size (Simulated)	150 kW/ 500 kWh	-	120 kW/ 320 kWh	-	10 kW/13.5 kWh
Tariff Type	Type A	Type B	Type C	Type E	Type F

3.2.2 System Configuration and Modeling

3.2.2.1 Overview of the System

The system we are considering here is a commercial building equipped with a renewable generation such as solar and BESS. Figure 3-2 shows the block diagram of the system configuration. A portion of the building load is satisfied by the power drawn from the utility grid. The remaining portion is satisfied by a fraction of the renewable generation

(solar in this case) and power discharged from the BESS. The power generated from the solar inverter is branched out to two portions. One branch delivers power directly to the building load as mentioned. The other branch charges the BESS. The BESS then discharges power to the building load as required. This configuration allows higher system efficiency by reducing power conversion-associated losses since part of the solar serves the building load directly. To ensure a higher percentage of renewable generation within the power mix, the BESS does not store any energy from the grid to avoid energy produced from fossil fuel.

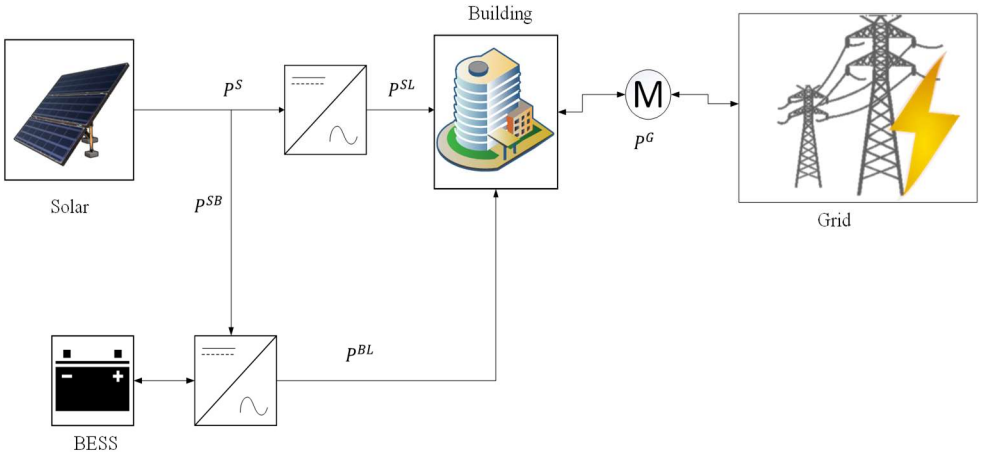

Figure 3-2 System Configuration Block Diagram

3.2.2.2 Battery Energy Storage System (BESS) Modeling

The BESS is modeled by taking many real-world operational constraints into considerations. The stored energy at each time step can be calculated with the following equation:

$$E_{t+1}^B = (1-\gamma)E_t^B + P_t^B.\Delta t \qquad (3.1)$$

The relationship between state of charge (SOC) and stored energy is mostly linear except for very low and very high SOC levels. Therefore, when we consider a small timestep duration, we can assume a linear relationship. The typical value for the self-discharge rate, γ for Li-ion battery is 1-2% over a month [108]. So, if Δt becomes small like 15 minute or 1-minute then γ≈0 and we can rewrite the equation as:

$$E_{t+1}^{B} = E_{t}^{B} + P_{t}^{B}.\Delta t \tag{3.2}$$

To expand the lifetime and maintain heath of the BESS battery cells, certain limits are imposed on the range of SOC or depth of charge and discharge. The battery must maintain its stored charge within a certain limit during every time step. Then,

$$E^{Bmin} \leq E_{t}^{B} \leq E^{Bmax} \tag{3.3}$$

The BESS power can be written in terms of charging and discharging power separately as:

$$P_{t}^{B} = P_{t}^{B+} - P_{t}^{B-} \tag{3.4}$$

These two power quantities should also be within some limitations depending on the size, application, and manufacturer specification of the BESS inverter. It can be modeled with the following inequality conditions:

$$0 \leq P_{t}^{B+} \leq P^{B+max} \tag{3.5}$$

$$0 \leq P_{t}^{B-} \leq P^{B-max} \tag{3.6}$$

But charging and discharging cannot happen simultaneously. This condition can be modeled by the following equation:

$$P_{t}^{B+} P_{t}^{B-} = 0 \tag{3.7}$$

3.2.2.3 System Power Balance

As mentioned in subsection 3.1, the building load is served by drawing power from the grid, a part of solar power and the power discharged from the BESS. The rest of the solar power is used to charge the battery. So, for each time step t, the system should obey the following power balance equations:

$$P_t^{B+} = \eta^+ P_t^{SB} \tag{3.8}$$

$$P_t^S = P_t^{SB} + P_t^{SL} \tag{3.9}$$

$$P_t^L = P_t^{SL} + P_t^{BL} + P_t^G \tag{3.10}$$

$$P_t^{BL} = \eta^- P_t^{B-} \tag{3.11}$$

$$P_t^{SL} \geq 0 \tag{3.12}$$

3.2.3 Objective Function Formulation

In this section, the cost functions or the objective functions of the optimization problems are formulated for different utility tariffs. The following subsections show detailed formulations for each of the six types of tariffs mentioned in section 3.2.1. Each subsection describes in detail how each type of tariff works and then a cost function is derived mathematically based on that along with the universal cost function by combining each of their unique tariff component. Some jargons' used in the tariffs may vary by utility company and location, but the main idea remains the same. This paper uses the traditional technical terms such as On-Peak, Mid-Peak, and Off-Peak times, etc. While formulating the cost functions, careful attention is paid to derive them in a way so that they become

convex and can be solved conveniently and efficiently with the available optimization tools. Only the costs related to usage are taken into account, fixed costs such as line or meter charge, taxes, etc., are not considered.

3.2.3.1 Type A: Multiple Time of Use (TOU) Energy Charges with a Single Time Independent Demand Charge

In this utility rate the energy charge is decided based on the period of the day and how much stressed the grid is during that period. Typically, they are separated into three nonoverlapping time periods: On-Peak, Mid-Peak, and Off-Peak where the value of the energy charge is from highest to lowest, respectively. In some cases, even lower energy charge time period can be found termed as Super Off-Peak period. Customer is billed based on total energy consumed at each period over the billing cycle. For demand, utilities measure the moving average of the load in kW for a certain duration, usually 15 minutes. The maximum demand that occurs within the billing month, irrespective of the time period, is multiplied by the demand charge in $/kW to obtain the demand cost of that month. Then both energy and demand cost are added to get the total bill for monthly usage.

The set of all timestamps $\boldsymbol{T^{tot}}$ can be written as,

$$\boldsymbol{T^{tot}} = \boldsymbol{T^{On}} \cup \boldsymbol{T^{Mid}} \cup \boldsymbol{T^{Off}} = \{0,1, \dots, T' - 1\} \tag{3.13}$$

Where,

$$\boldsymbol{T^{On}} \cap \boldsymbol{T^{Mid}} = \boldsymbol{T^{Mid}} \cap \boldsymbol{T^{Off}} = \boldsymbol{T^{Off}} \cap \boldsymbol{T^{On}} = \emptyset \tag{3.14}$$

Energy charge α_t can be written as,

$$\alpha_t = \begin{cases} \alpha^{On}, & t \in \boldsymbol{T^{On}} \\ \alpha^{Mid}, & t \in \boldsymbol{T^{Mid}} \\ \alpha^{Off}, & t \in \boldsymbol{T^{Off}} \end{cases} \tag{3.15}$$

Then we can write the cost function or the objective function as:

$$f(P_t^G) = \Delta t \sum_{t=0}^{T\prime-1} \alpha_t P_t^G + \beta max(\mathbb{P}^{\boldsymbol{G}}) \tag{3.16}$$

Where set of grid power values,

$$\mathbb{P}^{\boldsymbol{G}} = \{P_t^G | t \in \boldsymbol{T^{tot}}\} \tag{3.17}$$

α_t and P_t^G can be written in vectorized form as,

$$\begin{bmatrix} \alpha_0 \\ \alpha_1 \\ . \\ . \\ \alpha_{T-1} \end{bmatrix} \text{and } \boldsymbol{P^G} = \begin{bmatrix} P_0^G \\ P_1^G \\ . \\ . \\ P_{T-1}^G \end{bmatrix} \tag{3.18}$$

Then we can write the cost function as:

$$f(\boldsymbol{P^G}) = \Delta t\, \boldsymbol{\alpha^T P^G} + \beta \max(\boldsymbol{P^G}) \tag{3.19}$$

3.2.3.2 Type B: Multiple TOU Energy Charges and Multiple TOU Demand Charges

Just like the energy charge mentioned in subsection 3.2.3.1, the demand charge is also time-dependent in this case. Instead of the maximum demand within the whole billing period, the customer is billed for the maximum demand of each of the three peak periods within the billing month. The main complexity here is that instead of the largest power value from the vector $\boldsymbol{P^G}$ we have to pick the maximum value from each of the TOU time periods and then minimize each of them in a way so that the total cost becomes minimum. To resolve it, this paper proposes to introduce three diagonal matrices $\boldsymbol{\beta^{On}}$, $\boldsymbol{\beta^{Mid}}$ and $\boldsymbol{\beta^{Off}}$ to represent On-peak, Mid-Peak and Off-Peak period demand charges, respectively.

$$\boldsymbol{\beta^{On}} = \begin{bmatrix} \beta_0^{On} & \cdots & 0 \\ \vdots & \ddots & \vdots \\ 0 & \cdots & \beta_{T'-1}^{On} \end{bmatrix}, \boldsymbol{\beta^{Mid}} = \begin{bmatrix} \beta_0^{Mid} & \cdots & 0 \\ \vdots & \ddots & \vdots \\ 0 & \cdots & \beta_{T'-1}^{Mid} \end{bmatrix} and$$

$$\boldsymbol{\beta^{Off}} = \begin{bmatrix} \beta_0^{Off} & \cdots & 0 \\ \vdots & \ddots & \vdots \\ 0 & \cdots & \beta_{T'-1}^{Off} \end{bmatrix} \tag{3.20}$$

Where, the diagonal entries of these matrices can be written as:

$$\begin{aligned} \beta_t^{On} &= \begin{cases} \beta^{On}, & t \in \boldsymbol{T^{On}} \\ 0, & otherwise \end{cases} \\ \beta_t^{Mid} &= \begin{cases} \beta^{Mid}, & t \in \boldsymbol{T^{Mid}} \\ 0, & otherwise \end{cases} \\ \beta_t^{Off} &= \begin{cases} \beta^{Off}, & t \in \boldsymbol{T^{Off}} \\ 0, & otherwise \end{cases} \end{aligned} \tag{3.21}$$

The off-diagonal elements in these matrices are all zero. Now, the cost function can be written as:

$$f(\boldsymbol{P^G}) = \Delta t\, \boldsymbol{\alpha^T P^G} + \max(\boldsymbol{\beta^{On} P^G}) + \max\left(\boldsymbol{\beta^{Mid} P^G}\right) + \max(\boldsymbol{\beta^{Off} P^G}) \tag{3.22}$$

Sometimes depending on the season, the tariff may have demand charge component of only one or two time periods. In those cases, we can similarly formulate the cost function, by removing the unnecessary term in equation 3.22 if required.

3.2.3.3 Type C: Multiple TOU Energy Charges with Multiple TOU Demand Charges and an Additional Time Independent Demand Charge

This rate is a combination of the rates described in the previous two subsections. It has both TOU demand charges for the maximum demand of each of the peak periods in the billing month and a time independent demand charge for the maximum peak happening anytime within the billing month. We can write the cost function for this rate as:

$$f(\boldsymbol{P^G}) = \Delta t\ \boldsymbol{\alpha^T P^G} + \max(\boldsymbol{\beta^{On} P^G}) + \max\left(\boldsymbol{\beta^{Mid} P^G}\right) + \max\left(\boldsymbol{\beta^{Off} P^G}\right) + \beta\max(\boldsymbol{P^G}) \quad (3.23)$$

where, the notations have the same meaning as shown in the previous two subsections.

Similar to type B, some TOU demand charge components may not be present depending on the season. By simply removing that demand charge part from equation 3.23 it can be applied.

3.2.3.4 Type D: Critical Peak Pricing Rate

Critical Peak Pricing or CPP rates offer lower demand rates in non-CPP event days in exchange for very high energy rates in CPP event days. CPP events are usually called when electricity demand peaks due to extreme or unusual grid operating conditions. They are usually the hottest summer days, occurring 12-15 days within the summer season determined by the utility company. The CPP event hours comprise the evening hours and early part of the night namely 4 PM to 9 PM. The customers are generally notified a day before the CPP event day.

A non-CPP day will have the energy charge vector $\boldsymbol{\alpha_{non-CPP}} = \boldsymbol{\alpha}$ just like the other rates. For a CPP day, we modify $\boldsymbol{\alpha}$ as $\boldsymbol{\alpha_{CPP}}$ where the energy charge α_t for timestep t needs to be modified when t is within the CPP event hours. The CPP event hours may overlap with part of the other TOU periods. Thus, the energy charge α_t for a CPP event day can be written as:

$$\alpha_t = \begin{cases} \alpha^{On}, & t \in \boldsymbol{T^{On}} \backslash \boldsymbol{T^{CPP}} \\ \alpha^{Mid}, & t \in \boldsymbol{T^{Mid}} \backslash \boldsymbol{T^{CPP}} \\ \alpha^{Off}, & t \in \boldsymbol{T^{Off}} \backslash \boldsymbol{T^{CPP}} \\ \alpha^{CPP}, & t \in \boldsymbol{T^{CPP}} \end{cases} \tag{3.24}$$

The demand charge matrices for the non-CPP days $\boldsymbol{\beta^{On}_{non-CPP}}, \boldsymbol{\beta^{Mid}_{non-CPP}}$ and $\boldsymbol{\beta^{Off}_{non-CPP}}$ need to be modified. We can do that by replacing the t-th diagonal element in the demand charge matrices from the previous subsections with the actual charge minus the discount charge offered by the utility company when t falls under the CPP event hours. The On-Peak demand charge β_t^{On} for a non-CPP event day can be written as:

$$\beta_t^{On} = \begin{cases} \beta^{On}, & t \in \boldsymbol{T^{On}} \backslash \boldsymbol{T^{CPP}} \\ \beta^{On} - \beta^{CPP}, & t \in \boldsymbol{T^{On}} \cap \boldsymbol{T^{CPP}} \\ 0, & otherwise \end{cases} \tag{3.25}$$

The Mid-Peak and Off-Peak demand charges β_t^{Mid} and β_t^{Off} for timestep t can be derived in a similar manner.

The same matrices for CPP days $\boldsymbol{\beta^{On}_{CPP}}, \boldsymbol{\beta^{Mid}_{CPP}}$ and $\boldsymbol{\beta^{Off}_{CPP}}$ are the same as the other TOU demand matrices shown in the previous subsections. So, we get two cost functions:

$$\begin{aligned} f(\boldsymbol{P^G}) = \Delta t\, \boldsymbol{\alpha_{non-CPP}}^{\boldsymbol{T}} \boldsymbol{P^G} &+ \max\left(\boldsymbol{\beta^{On}_{non-CPP}} \boldsymbol{P^G}\right) \\ &+ \max\left(\boldsymbol{\beta^{Mid}_{non-CPP}} \boldsymbol{P^G}\right) + \max\left(\boldsymbol{\beta^{Off}_{non-CPP}} \boldsymbol{P^G}\right) \\ &+ \beta \max(\boldsymbol{P^G}) \end{aligned} \tag{3.26}$$

$$\begin{aligned} \text{and } f(\boldsymbol{P^G}) = \Delta t\, \boldsymbol{\alpha_{CPP}}^{\boldsymbol{T}} \boldsymbol{P^G} &+ \max\left(\boldsymbol{\beta^{On}_{CPP}} \boldsymbol{P^G}\right) + \max\left(\boldsymbol{\beta^{Mid}_{CPP}} \boldsymbol{P^G}\right) \\ &+ \max\left(\boldsymbol{\beta^{Off}_{CPP}} \boldsymbol{P^G}\right) + \beta \max(\boldsymbol{P^G}) \end{aligned} \tag{3.27}$$

Where equations 3.26 and 3.27 represent the cost functions for non-CPP days and CPP days, respectively. We should note that, the discounted rates at non-CPP days are also

provided during the same hours as the CPP event hours at CPP days. Similar to equation 3.22, we can also modify 3.26 and 3.27 if some other TOU demand charge is absent in the tariff.

3.2.3.5 Type E: A Simple Flat Energy Charge with a Time Independent Demand Charge

For a flat energy rate with a monthly peak demand charge the variable α_t becomes a constant independent of time and we can replace the energy charge vector $\boldsymbol{\alpha}$ with a single scalar value α. The cost function then becomes:

$$f(\boldsymbol{P^G}) = \Delta t.\alpha\,.\,\mathbf{1}^{\boldsymbol{T}}\boldsymbol{P^G} + \beta\max(\boldsymbol{P^G}) \tag{3.28}$$

Where 1 denotes a vector of size T' with all elements as 1.

3.2.3.6 Type F: TOU energy charges only

This tariff type has no demand charges. The energy charge part is similar to type A. We can just remove the demand charge component from equation 3.19 and the cost function then becomes:

$$f(\boldsymbol{P^G}) = \Delta t\ \boldsymbol{\alpha}^{\boldsymbol{T}}\boldsymbol{P^G} \tag{3.29}$$

3.2.3.7 Universal cost function

The universal cost function can now be represented with a similar format like that of equations 23, 26 and 27 which captures all the energy and demand charge components. We just need to apply the appropriate equation based on whether the tariff type is CPP or not, whether the day of optimization is a CPP event day or not and which of the energy or demand charge components are present with the modifications described above. Based on the tariff type and component we can just insert the applicable energy and demand charge

values if present or make them zero if absent. Table 3.2 summarizes the tariff components for each of the tariff type which we can use to apply to our universal cost function.

Table 3-2 Summary of tariff components of different tariff types

Tariff Component		Type A	Type B	Type C	Type D	Type E	Type F
Energy Charge	On-Peak	✓	✓	✓	✓	×	✓
	Mid-Peak	✓	✓	✓	✓	×	✓
	Off-Peak	✓	✓	✓	✓	×	✓
	CPP	×	×	×	✓	×	×
	Flat	×	×	×	×	✓	×
Demand Charge	Time Independent	✓	×	✓	✓	✓	×
	On-Peak	×	✓/×	✓/×	✓/×	×	×
	Mid-Peak	×	✓/×	✓/×	✓/×	×	×
	Off-Peak	×	✓/×	✓/×	✓/×	×	×
	CPP Discount	×	×	×	✓	×	×

* ✓: Present, ×: Absent, ✓/×: May or may not be present

3.2.4 Optimization problem formulation

Using the universal cost function formulated in section 3.2.3 as the objective function and the BESS modelling and power balance equations from subsection 3.2.2.2 and 3.2.2.3 as constraints, we can now derive the optimization problem for each of the tariffs described before.

But equation 3.7 in the model is a nonlinear equality condition which makes the problem nonconvex and difficult to solve. We can resolve it by introducing a binary variable $\delta_t \in \{0,1\}$ to the power limit constraints of equation 3.5 and 3.6 and perform a convex relaxation on the binary variable. So, we reformulate them as:

$$0 \leq P_t^{B+} \leq \delta_t P^{B+max} \quad (3.30)$$

$$0 \leq P_t^{B-} \leq (1-\delta_t) P^{B-max} \quad (3.31)$$

$$0 \leq \delta_t \leq 1 \quad (3.32)$$

We can now write the optimization problem as shown below:

$$\min_{\boldsymbol{P^G}} f(\boldsymbol{P^G})$$

subject to:

$$E_{t+1}^B = E_t^B + P_t^B . \Delta t, \forall t \in \boldsymbol{T^{tot}} \quad (3.2)$$

$$E^{Bmin} \leq E_t^B \leq E^{Bmax}, \forall t \in \boldsymbol{T^{tot}} \quad (3.3)$$

$$P_t^B = P_t^{B+} - P_t^{B-}, \forall t \in \boldsymbol{T^{tot}} \quad (3.4)$$

$$0 \leq P_t^{B+} \leq \delta_t P^{B+max}, \forall t \in \boldsymbol{T^{tot}} \quad (3.30)$$

$$0 \leq P_t^{B-} \leq (1-\delta_t) P^{B-max}, \forall t \in \boldsymbol{T^{tot}} \quad (3.31)$$

$$0 \leq \delta_t \leq 1, \forall t \in \boldsymbol{T^{tot}} \quad (3.32)$$

$$P_t^{B+} = \eta^+ P_t^{SB}, \forall t \in \boldsymbol{T^{tot}} \quad (3.8)$$

$$P_t^S = P_t^{SB} + P_t^{SL}, \forall t \in \boldsymbol{T^{tot}} \quad (3.9)$$

$$P_t^L = P_t^{SL} + P_t^{BL} + P_t^G, \forall t \in \boldsymbol{T^{tot}} \quad (3.10)$$

$$P_t^{BL} = \eta^- P_t^{B-}, \forall t \in \boldsymbol{T^{tot}} \quad (3.11)$$

$$P_t^{SL} \geq 0 \quad (3.12)$$

By applying the appropriate parameter values, we can use this optimization model to obtain the optimal operation, for any commercial tariff, given a building load and a solar generation profile.

3.2.5 Algorithm

For our proposed method we do the optimization on a day-by-day basis instead of doing a monthly optimization. We do this for a couple of reasons. Firstly, the day ahead prediction of load and solar can be produced more accurately and easily for a shorter time resolution such as 15 minutes. For this sort of time resolution, month ahead prediction will contain more inaccuracy. By doing a day ahead prediction we can also easily determine the operation of the BESS for the next day. Secondly, doing a monthly optimization with this

15-minute data resolution would be computationally exhaustive. Without a very high processing power and large memory device, the optimization will require much more computational time to solve.

Since we are doing a daily optimization, the total number of timesteps considered T' will be 96 in the case of 15-minute resolution. The vectors and matrices introduced in section 3.2.3 will have corresponding sizes. We can write the daily building load profile and solar generation profile in vectorized form as:

$$\boldsymbol{P^L} = \begin{bmatrix} P_0^L \\ P_1^L \\ . \\ . \\ P_{T'-1}^L \end{bmatrix} \text{ and } \boldsymbol{P^S} = \begin{bmatrix} P_0^S \\ P_1^S \\ . \\ . \\ P_{T'-1}^S \end{bmatrix} \tag{3.33}$$

In this section, we will refer to the daily energy charge and demand charges as $\boldsymbol{\alpha}$ and $\boldsymbol{\beta}$ in general. To calculate the actual monthly usage bill, we will need to get new vectors and matrices that will accommodate the monthly calculation. If the number of total days in the monthly billing cycle is D, then we can create the new matrices of size $(D \times T', D \times T')$ and vectors of length $D \times T'$ for the monthly bill calculation.

When we are doing the optimization, we must consider the day of the week and the season. On-Peak, Mid-Peak and Off-Peak hours and prices typically vary depending on day of the week and season. Consequently, the elements of the sets $\boldsymbol{T^{On}}$, $\boldsymbol{T^{Mid}}$, and $\boldsymbol{T^{Off}}$ will be different though the elements of $\boldsymbol{T^{tot}}$ will be the same. Similarly, energy charges α^{On}, α^{Mid}, and α^{Off} and demand charges β^{On}, β^{Mid}, and β^{Off} will also vary. Typically, government holidays also have identical periods and prices similar to weekends.

The energy charge vector for the month $\boldsymbol{\alpha_{month}}$will then become:

$$\boldsymbol{\alpha_{month}} = [\boldsymbol{\alpha_0^T}\ \boldsymbol{\alpha_1^T} \dots \dots \boldsymbol{\alpha_{D-1}^T}]^T \tag{3.34}$$

where,

$$\boldsymbol{\alpha_d} = \begin{cases} \boldsymbol{\alpha_{weekday}}, & d\ is\ a\ weekday \\ \boldsymbol{\alpha_{weekend}}, & d\ is\ a\ weekend/holiday \end{cases} \tag{3.35}$$

We can get the On-Peak TOU demand charge matrix for the month $\boldsymbol{\beta_{month}^{On}}$ by:

$$\boldsymbol{\beta_{month}^{On}} = \begin{bmatrix} \boldsymbol{\beta_0^{On}} & \cdots & \mathbf{0} \\ \vdots & \ddots & \vdots \\ \mathbf{0} & \cdots & \boldsymbol{\beta_{D-1}^{On}} \end{bmatrix} \tag{3.36}$$

where,

$$\boldsymbol{\beta_d^{On}} = \begin{cases} \boldsymbol{\beta_{weekday}^{On}}, & d\ is\ a\ weekday \\ \boldsymbol{\beta_{weekend}^{On}}, & d\ is\ a\ weekend/holiday \end{cases} \tag{3.37}$$

Similarly, we can find the other TOU demand matrices $\boldsymbol{\beta_{month}^{Mid}}$ and $\boldsymbol{\beta_{month}^{Off}}$, which represent the Mid-Peak and Off-Peak TOU demand charge matrix for the billing month, respectively.

If we are dealing with a CPP rate structure in the summer season, then equations 3.34 and 3.36 will be a little different. The $\boldsymbol{\alpha_d}$ will be $\boldsymbol{\alpha_{CPP}}$ if d-th day is a CPP event day. On the other hand, $\boldsymbol{\beta_d^{On}}, \boldsymbol{\beta_d^{Mid}}$ and $\boldsymbol{\beta_d^{Off}}$ will be replaced by $\boldsymbol{\beta_{non-CPP}^{On}}, \boldsymbol{\beta_{non-CPP}^{Mid}}$ and $\boldsymbol{\beta_{non-CPP}^{Off}}$, respectively if d-th day is a non-CPP event day.

We can then calculate the monthly usage bills by using the applicable cost function just by using the appropriate power vector of the right size and parameters $\boldsymbol{\alpha_{month}}$ and $\boldsymbol{\beta_{month}}$.

$$Monthly\ Usage\ Bill = f(\boldsymbol{X}; \boldsymbol{\alpha_{month}}, \boldsymbol{\beta_{month}}) \tag{3.38}$$

Where **X** is the appropriate power vector of length $D \times T'$. We can now calculate the monthly usage bill for a building load alone, a building net load with solar or net load with solar and BESS optimization. To better understand the effects of the optimization, we define two types of savings, $Savings^{Solar}$ and $Savings^{BESS}$. $Savings^{Solar}$ shows the savings if only the solar is added without any BESS optimization. $Savings^{BESS}$ shows the effect of BESS optimization that is the additional savings we made through BESS optimization when solar is already present in the system. We can write them as:

$$Savings^{Solar} = f\left(\boldsymbol{P}^{\boldsymbol{L}}_{\boldsymbol{month}}; \boldsymbol{\alpha}_{\boldsymbol{month}}, \boldsymbol{\beta}_{\boldsymbol{month}}\right) - f(\boldsymbol{P}^{\boldsymbol{L}}_{\boldsymbol{month}} - \boldsymbol{P}^{\boldsymbol{S}}_{\boldsymbol{month}}; \boldsymbol{\alpha}_{\boldsymbol{month}}, \boldsymbol{\beta}_{\boldsymbol{month}}) \quad (3.39)$$

$$Savings^{BESS} = f\left(\boldsymbol{P}^{\boldsymbol{L}}_{\boldsymbol{month}} - \boldsymbol{P}^{\boldsymbol{S}}_{\boldsymbol{month}}; \boldsymbol{\alpha}_{\boldsymbol{month}}, \boldsymbol{\beta}_{\boldsymbol{month}}\right) - f(\boldsymbol{P}^{\boldsymbol{G}}_{\boldsymbol{month}}; \boldsymbol{\alpha}_{\boldsymbol{month}}, \boldsymbol{\beta}_{\boldsymbol{month}}) \quad (3.40)$$

To run the optimization, we have to get values of the other parameters E^{Bmax}, E^{Bmin}, E^{B}_{init}, P^{B+max}, P^{B-max}, η^{+} and η^{-}. Variables $\boldsymbol{P^{SL}}$, $\boldsymbol{P^{SB}}$, $\boldsymbol{P^{B+}}$ and $\boldsymbol{P^{B-}}$ need to be declared similar to vectors shown in equation 3.33 which represent the solar power fed to the load, BESS power fed to the load, BESS charging and discharging power vectors for the day, respectively.

Now that we have described all the necessary variables and parameters, the algorithm for the optimization process can be written as:

Algorithm

1: Select the type of tariff
2: Select Season
3: Get parameters E^{Bmax}, E^{Bmin}, E^{B}_{init}, P^{B+max}, P^{B-max}, η^{+} and η^{-}.
4: **if** (Tariff type=CPP rate) and (Season=Summer) then:
5: Get $\boldsymbol{\alpha_{CPP}}$, $\boldsymbol{\beta_{CPP}}$, $\boldsymbol{\alpha_{non-CPP}}$, and $\boldsymbol{\beta_{non-CPP}}$
6: **else**
7: Get $\boldsymbol{\alpha}$, $\boldsymbol{\beta}$
8: **endif**
9: Declare empty vectors $\boldsymbol{P^{G}_{month}} = [\ \ ]$, $\boldsymbol{P^{L}_{month}} = [\ \ ]$, $\boldsymbol{P^{S}_{month}} = [\ \ ]$
10: **for** each day d=0,1, ……., D-1 do:
11: **if** (Tariff Type=CPP) then:
12: **if** (Day d=CPP Event Day) then:
13: Get $\boldsymbol{\alpha_{CPP}}$, $\boldsymbol{\beta_{CPP}}$
14: **else**
15: Get $\boldsymbol{\alpha_{non-CPP}}$, $\boldsymbol{\beta_{non-CPP}}$
16: **endif**
17: **elseif** (Day d==weekday) then:
18: Get $\boldsymbol{\alpha}$, $\boldsymbol{\beta}$ for weekday
19: **else**
20: Get $\boldsymbol{\alpha}$, $\boldsymbol{\beta}$ for weekend and holiday
21: **endif**
22: Get $\boldsymbol{P^{L}}$, $\boldsymbol{P^{S}}$ for day d
23: Declare the other variables $\boldsymbol{P^{SL}}$, $\boldsymbol{P^{SB}}$, $\boldsymbol{P^{B+}}$ and $\boldsymbol{P^{B-}}$
24: Initialize $E^{B}_{0}=E^{B}_{init}$
25: Run Optimization
26: Run the optimum BESS operation according to $\boldsymbol{P^{B+}}$ and $\boldsymbol{P^{B-}}$
27: Update $\boldsymbol{P^{G}_{month}} = \begin{bmatrix} \boldsymbol{P^{G}_{month}} \\ \boldsymbol{P^{G}} \end{bmatrix}$
28: Update $\boldsymbol{P^{L}_{month}} = \begin{bmatrix} \boldsymbol{P^{L}_{month}} \\ \boldsymbol{P^{L}} \end{bmatrix}$ and $\boldsymbol{P^{S}_{month}} = \begin{bmatrix} \boldsymbol{P^{S}_{month}} \\ \boldsymbol{P^{S}} \end{bmatrix}$
29: Update $E^{B}_{init}=E^{B}_{T-1}$
30: **endfor**
31: Calculate the unoptimized monthly cost $f(\boldsymbol{P^{L}_{month}}; \boldsymbol{\alpha_{month}}, \boldsymbol{\beta_{month}})$
32: Calculate the unoptimized monthly cost is solar is added $f(\boldsymbol{P^{L}_{month}} - \boldsymbol{P^{S}_{month}}; \boldsymbol{\alpha_{month}}, \boldsymbol{\beta_{month}})$
33: Calculate the optimized monthly cost with solar and BESS $f(\boldsymbol{P^{G}_{month}}; \boldsymbol{\alpha_{month}}, \boldsymbol{\beta_{month}})$
34: Calculate $Savings^{Solar} = f\left(\boldsymbol{P^{L}_{month}}; \boldsymbol{\alpha_{month}}, \boldsymbol{\beta_{month}}\right) - f(\boldsymbol{P^{L}_{month}} - \boldsymbol{P^{S}_{month}}; \boldsymbol{\alpha_{month}}, \boldsymbol{\beta_{month}})$ and
$Savings^{BESS} = f\left(\boldsymbol{P^{L}_{month}} - \boldsymbol{P^{S}_{month}}; \boldsymbol{\alpha_{month}}, \boldsymbol{\beta_{month}}\right) - f(\boldsymbol{P^{G}_{month}}; \boldsymbol{\alpha_{month}}, \boldsymbol{\beta_{month}})$

3.2.6 Results

Using the data and parameters collected and simulated for the four buildings mentioned in section 3.2.1, the building load optimizations were performed for their corresponding tariffs for a month. All data used are from the summer months and the rates used were summer season rates. For all these rates the daily On-Peak hours were from 12 PM to 6 PM on weekdays, Mid-Peak hours were from 8 AM to 12 PM and from 6 PM to 11 PM on weekdays and the remaining hours are all Off-Peak Hours. At the start of each

simulation, it is assumed that all the BESS have their initially stored energy E_{init}^{B} at 50% of the total capacity. The limits for maximum and minimum stored energy for each BESS E^{Bmax} and E^{Bmin} is assumed to be 90% and 20% of their total capacity, respectively. For the simulations in this work MATLAB based convex optimization toolbox CVX have been used [109]. The running time of the optimization for different tariffs ranges from 1 minute 28 seconds to 2 minute 4 seconds. The configuration of the PC used for optimization was Intel Core i-7 processor (6th generation 2.6 GHz), 16 GB RAM and 8 GB GPU).

Since type D or CPP is a more recent concept, the utilities normally give customers with an option that they can either move to CPP or can stay under the existing tariff. It may be opt-in or opt-out. In this paper, building 1 is chosen for CPP rate simulation and the rates for the CPP option of that tariff are applied here. It has four months in the summer season (June to September) and total 12 CPP event days in the summer season. So, on average each month will have three CPP days. The three highest demand days (day numbers 9, 12, and 20) for building 1 are selected as CPP event days in this simulation. The CPP event hours take place from 4 PM to 9 PM.

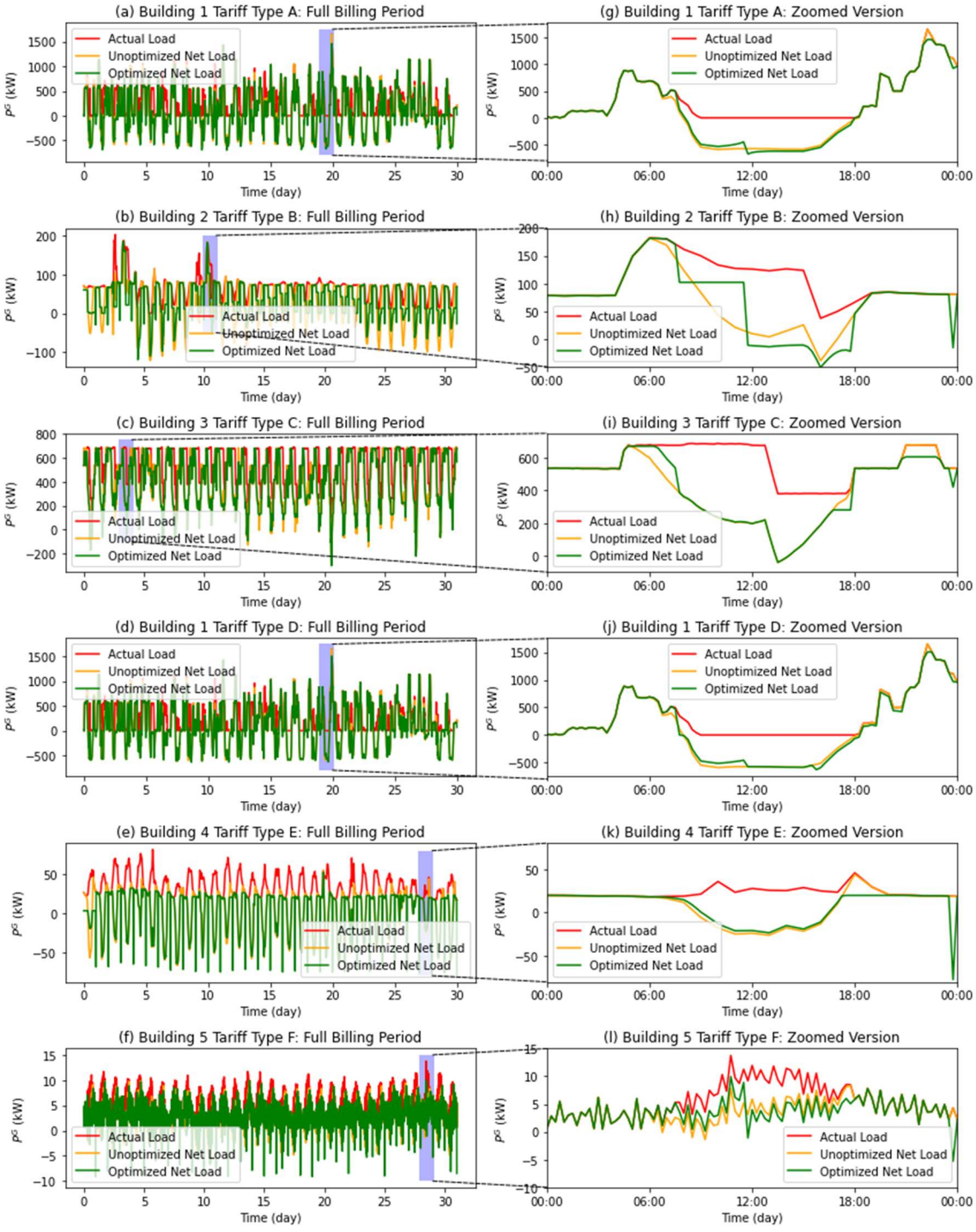

Figure 3-3 Results from optimization showing the power drawn from grid before optimization (actual load), after adding solar (unoptimized net load) and after optimization with solar and BESS (optimized net load) with zoomed in versions for a day

Figure 3-3 shows the results of the optimization for each type of tariffs for a month. Effects of the optimization can be observed by comparing the power drawn from the grid if no action is taken, if solar is added and if solar and BESS optimization is performed, which are termed as the actual building load, the unoptimized net load and the optimized net load, respectively. For better understanding, zoomed in versions of the plots for a day are also presented. The energy shifts can be observed in subplots (g)-(l). We can notice the optimized net load is higher than unoptimized net load during early morning Mid-Peak hours and lower starting from midday On-Peak hours. These correspond to the charging and discharging of BESS, respectively. We can also see the peak reduction activities of BESS in the subplots. The actual loads and unoptimized net loads of subplots (g) and (j) are identical as these are from the same building. But the optimized net loads subplot (j) is different from subplot (g) since the cost functions are different. Unlike subplot (g), no BESS discharge is noticed between 12-4 PM in subplot (j), while higher discharge can be seen between 4-9 PM. This is because of the much higher On-Peak energy rate during 4-9 PM of CPP rate. In subplot (k) peak reduction can be overserved more than energy shifting. This is due to flat energy rate of tariff type E. While in subplot (l) energy shifting is observed to be more prominent than the peak reduction.

Table 3-3 Summary of Optimization Results

Optimization Parameters and Results	Type A	Type B	Type C	Type D	Type E	Type F
Building	Building 1	Building 2	Building 3	Building 1	Building 4	Building 5
Energy Charge ($/kWh)	On-Peak: 0.3397 Mid-Peak: 0.13837 Off-Peak: 0.07637	On-Peak: 0.35987 Mid-Peak: 0.1007 Off-Peak: 0.03545	On-Peak: 0.10258 Mid-Peak: 0.07566 Off-Peak: 0.05727	On-Peak: 0.07817 Mid-Peak: 0.07422 Off-Peak: 0.0724 CPP: 0.4	Flat rate: 0.0139	On-Peak: 0.22617 Mid-Peak: 0.18317 Off-Peak: 0.15457
Demand Charge ($/kW)	Monthly Peak: 11.87	On-Peak: 7.06 Mid-Peak: 3.13 Off-Peak: 1.53	On-Peak: 21.73 Mid-Peak: 4.17 Monthly Peak: 19.02	On-Peak: 16 Mid-Peak: 5.16 Monthly Peak: 17.52 CPP discount: 4.11	Monthly Peak: 10.58	-
Unoptimized Cost ($)	47,884	9,278	61,704	79,714	4,218	654
Unoptimized Cost with Solar ($)	13,908	1,911	50,766	68,778	1,122	384
Optimized Cost with Solar and BESS ($)	9,646	1,497	47,956	62,825	991	361
$Savings^{Solar}$ ($)	33,977 (70.96%)	7,367 (79.73%)	10,938 (17.73%)	10,936 (13.72%)	3,096 (73.39%)	270 (41.28%)
$Savings^{BESS}$ ($)	4,261 (8.9%)	414 (4.46%)	2,810 (4.55%)	5,953 (7.47%)	131 (3.11%)	23 (3.52%)

Table 3.3 summarizes the optimization results from all the simulations. We can see that building 3 has a much higher actual cost than building 1 despite having much lower energy charges and a comparable daily average usage. This can be attributed to the TOU demand charges and higher time independent demand charge. We can observe that $Savings^{Solar}$ percentage values for type A, B and, E are very high. The $Savings^{Solar}$ percentage of type C and D are quite low while type F has a moderate value. The reason behind this for A and B can be considerably higher On-Peak energy charges of these tariffs. As the On-Peak period is from 12 to 6 PM, when most of the solar is produced, savings from solar can be sizable for this period. As for type E, the size of the solar capacity connected to the building is significantly larger compared to the building load. By comparing percentages of $Savings^{BESS}$ or additional savings with the presence of BESS, we see that adding a BESS would be most beneficial to type A rates. The reason type B's $Savings^{BESS}$ percentage being lower can be due to the fact that, type A has a time independent demand charge while type B has TOU demand charges. Reducing the highest peak in the month would result in large savings for type A while reducing the On-Peak highest demand would result in increasing the demand in other periods, which in turn decreases the savings compared to type A. Also, the difference in demand charge prices among the peak periods is not as significant in type B compared to other types. Though type C has significant difference between the TOU demand charges of different periods, the lower savings percentage could be attributed to a large time independent peak demand charge and a high load factor. As the average to maximum load ratio is high, there is not much scope for savings from peak reduction in this case. Even if some peak is shifted to a

lower price Mid-Peak period, the time independent demand charge will result in a very high cost. Type D also results in a good amount of savings from BESS. Since the CPP event hours have a considerably higher energy price and occur when solar generation keeps going down, energy shifting from BESS can reduce much cost while savings from solar becomes much lower than other types. The reason for type E having a low $Savings^{BESS}$ is because the highest peak in the month happens at 2 PM when there is abundant solar. Also, flat energy rate does not achieve any savings from energy shift. Type F also has a low $Savings^{BESS}$ percentage as there is cost reduction opportunity comes only from energy shift and the small differences of the peak period prices lessens the magnitude of it. By comparing the results for types A and D, we see that choosing the CPP option would result in loss for the customer, even with solar or BESS. Although if it were made mandatory, then adding BESS would serve to be beneficial if solar was present.

3.3 Impacts Analysis of Tariff Changes on Commercial Building Load Optimization using DERs

In this section, we will analyse how different changes in utility tariffs impact the optimization results discussed in the previous section. For this purpose, we will investigate the effects of three different changes. First, how the periodical price change of the energy and demand charges impact the savings. Second, how the choice of demand charge heavy or energy charge heavy rate options plays out for different building types. Lastly, how the time shifts in the rates affects the building net load. The first two scenarios are analysed from the perspective of building user benefit. The last scenario is analysed from the perspective of utility's interest. The analyses are presented in the following subsections.

3.3.1 Impacts due to the Periodical Price Changes

An important issue with the utility rates is that the prices of these charges often change. To understand how these changes impact the savings and how much benefit we can receive in the future from this optimization, an analysis was done on the building 2 load data using historical and forthcoming values of tariff Type B published by the utility. This tariff has three energy and three demand charge components, a total of six. The year of our actual analysis in previous sections is chosen as the base year values. Five years of tariff data is available and price of each tariff component has increased every year. We choose one component and change its values for the past and future years, while keeping the other components fixed at the base year values. We run the optimization and compare the results for all the different cases. The base year is denoted as year 0 while negative and positive values denote past and future values, respectively. Figure 3-4 shows the energy and demand charge values for each year.

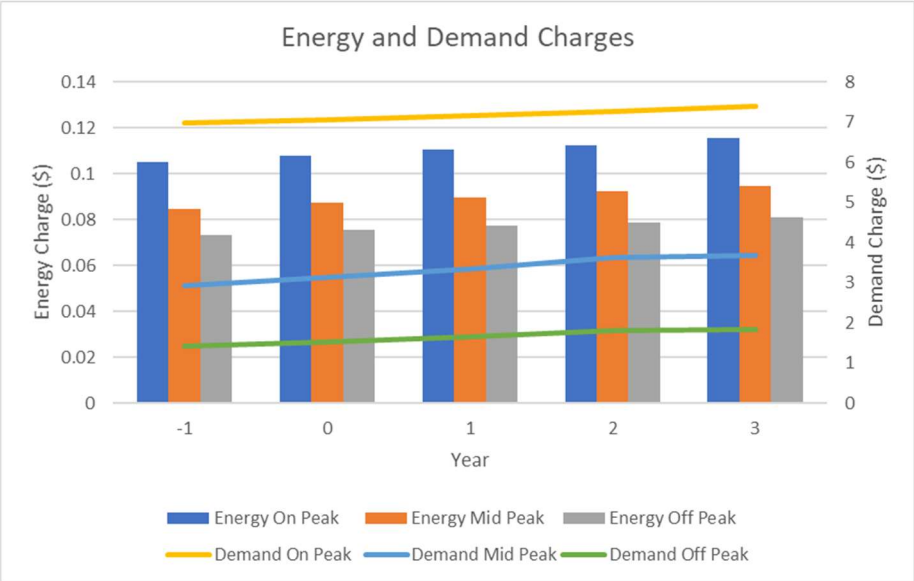

Figure 3-4 Energy and Demand Charge Values for Past and Future Years

Figure 3-5 shows the effect of price on $Savings^{Solar}$, that is, savings from solar. It can be seen that the $Savings^{Solar}$ values are highly impacted by On-Peak energy and demand charge changes. It is somewhat less impacted by Mid-Peak energy and demand charge changes. There is almost no change in $Savings^{Solar}$ values due to Off-Peak energy and demand charge changes. This is expected since most of the solar is produced during the On-Peak period, while the solar production is much less in the Mid-Peak period and there is almost no solar production during Off-Peak period.

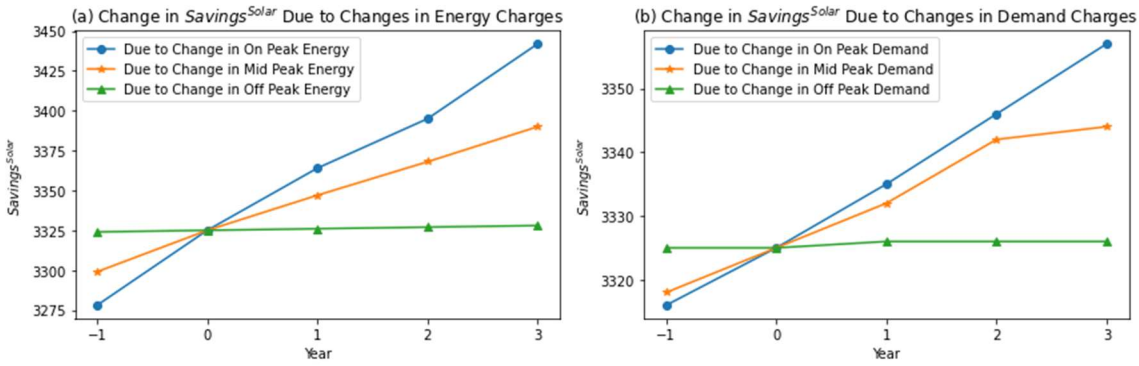

Figure 3-5 $Savings^{Solar}$ Due to Changes in Energy Charges and Demand Charges

Figure 3-6 shows the effect of price on $Savings^{BESS}$. Here we see that increase in On-Peak energy charge causes $Savings^{BESS}$ to decrease while Mid-Peak energy charge causes it to increase. This scenario is reversed in the case of demand charges. Savings stays same for Off-Peak energy and demand charge change as shifting energy or peak from this period does not result in any additional savings from optimization. The reason behind the unexpected behavior of On and Mid-Peak change is because energy and peak reduction from one period through battery optimization causes to increase the energy and peak in other periods, which makes it less obvious if our optimal solution will end up with a higher

or lower savings. Here, this type of analysis can be very useful as we can predict the future possible savings by assessing the trend.

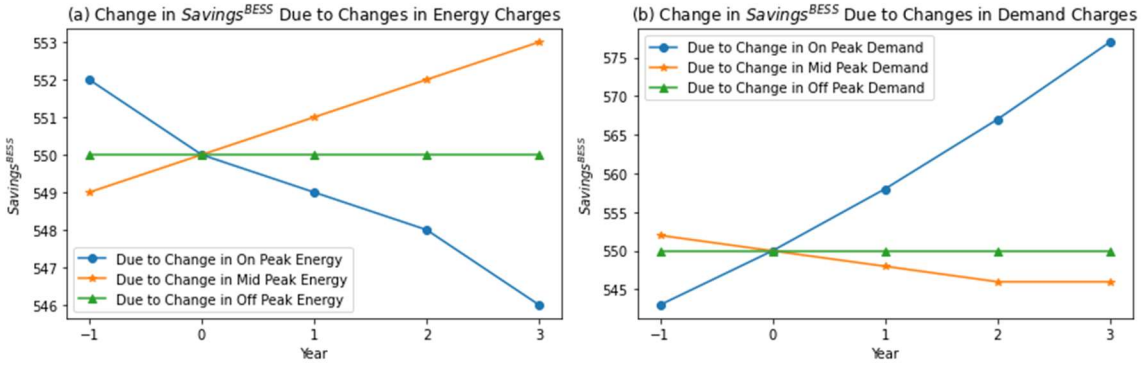

Figure 3-6 $Savings^{BESS}$ Due to Changes in Energy Charges and Demand Charges

3.3.2 Impacts due to Changes between the Energy Charge Heavy and Demand Charge Heavy Options

Utilities sometimes provide options under the same tariff. One option contains higher demand charges and lower energy charges while the other contains higher energy charges and lower demand charges. To compare the user benefits between these two options we use both for our optimization on buildings 1 and 3 and compare the savings. These two buildings were chosen since they have similar daily consumption but differing load factors. Load factor is an indicator of how efficiently the energy is used. A low load factor means that the average load is lower compared to the peak load within a period. This translates to the fact that while the average consumption of the building can be satisfied with a lower capacity system, the utility needs to increase the capacity to accommodate the peak load. A high load factor implies that the capacity to satisfy the peak load does not need to be increased compared to the low load factor scenario. We apply the optimization

using the options that is found in a type C rate. Table 3-4 shows the prices for these options. The option with higher demand charges is named as demand option while the option with higher energy charges is named as energy option. The TOU demand charge in this rate is On-Peak Demand charge only.

Table 3-4 Demand heavy and Energy heavy Options applied to Type C rate

Charge	Demand Option	Energy Option
On Peak Energy ($/kWh)	0.12158	0.49669
Mid Peak Energy ($/kWh)	0.11337	0.19008
Off Peak Energy ($/kWh)	0.0867	0.12325
Time Independent Peak Demand ($/kW)	14.98	10.3
On-Peak Demand ($/kW)	34.68	4.98

Table 3-5 summarizes the results of the optimization on buildings 1 and 3 using the rates shown in table 3-4.

Table 3-5 Optimization results for demand heavy and energy heavy options

Building	Building 1		Building 3	
Option	Demand Option	Energy Option	Demand Option	Energy Option
Unoptimized Cost ($)	115,990	117,200	77,701	104,460
Unoptimized Cost with Solar ($)	81,921	65,476	62,871	67,551
Optimized Cost with Solar and BESS ($)	76,052	61,645	58,604	64,492
$Savings^{Solar}$ ($)	34,070 (29.37%)	51,725 (49.25%)	14,830 (19.01%)	36,911 (35.33%)
$Savings^{BESS}$ ($)	5,869 (5.06%)	3,831 (3.27%)	4,267 (5.49%)	3,059 (2.92%)

We analyse the results from two perspectives: first, we assume that the customers can choose between the options. Comparing the unoptimized costs in table 3.5 we see that, without any DERs, buildings with low load factor do not benefit much from the choice

between the options. Though buildings with high load factors can benefit from choosing the demand option. Buildings who have existing solar generation should choose the energy option if their load factor is low but should choose the demand option if their load factor is high, which would result in lowering their cost. Buildings with both solar and BESS should also make the same decision based on load factors. Now we assume that the utility decides for the customers which option they fall under, and customers do not have any authority over it. Buildings with low load factors receive higher benefits from adding solar than buildings with high load factors, regardless of the rate option. The savings is considerable for buildings with low load factors falling under the energy option but less attractive for buildings with high load factor falling under demand option. The additional benefit from BESS does not vary for higher or lower load factor which is counterintuitive. Their added benefit is not as significant as the benefit of adding solar for buildings with low load factors. Though buildings with high load factors that fall under demand option might consider adding BESS because the total savings from solar and BESS is a considerable improvement over only having solar.

3.3.3 Impacts due to the Shifts in Time of Use Periods

As discussed in chapter 1, the CAISO Duck Curve poses a challenge to the utility operators due to high ramp rate requirements to counter rapid decline in solar PV production in the evening period. To alleviate this condition the utilities are introducing completely new or adjusting existing TOU time periods. This shift in time is supposed to help reduce the high ramp rate through demand response of customers with load shifting abilities, such as commercial buildings with DERs. This is done by mainly bringing a shift

in the legacy 12 to 6 PM On-Peak period in the weekdays. The newly introduced TOU period is administered by defining the On-Peak period from 4 PM to 9 PM and rest of the hours as Mid-Peak on weekdays and making the 4 to 9 as the Mid-Peak period and keeping rest of the hours as Off-Peak on weekends. To examine the effect of this time shift on commercial buildings we apply both the rates with conventional and new time periods into our optimization using building 1 data for tariff type A. We also propose a dynamic rate with varying prices to reduce ramp rates in the evenings. Figure 3-7 shows the traditional or legacy rate, newly introduced current rate and the dynamic rate proposed by the author.

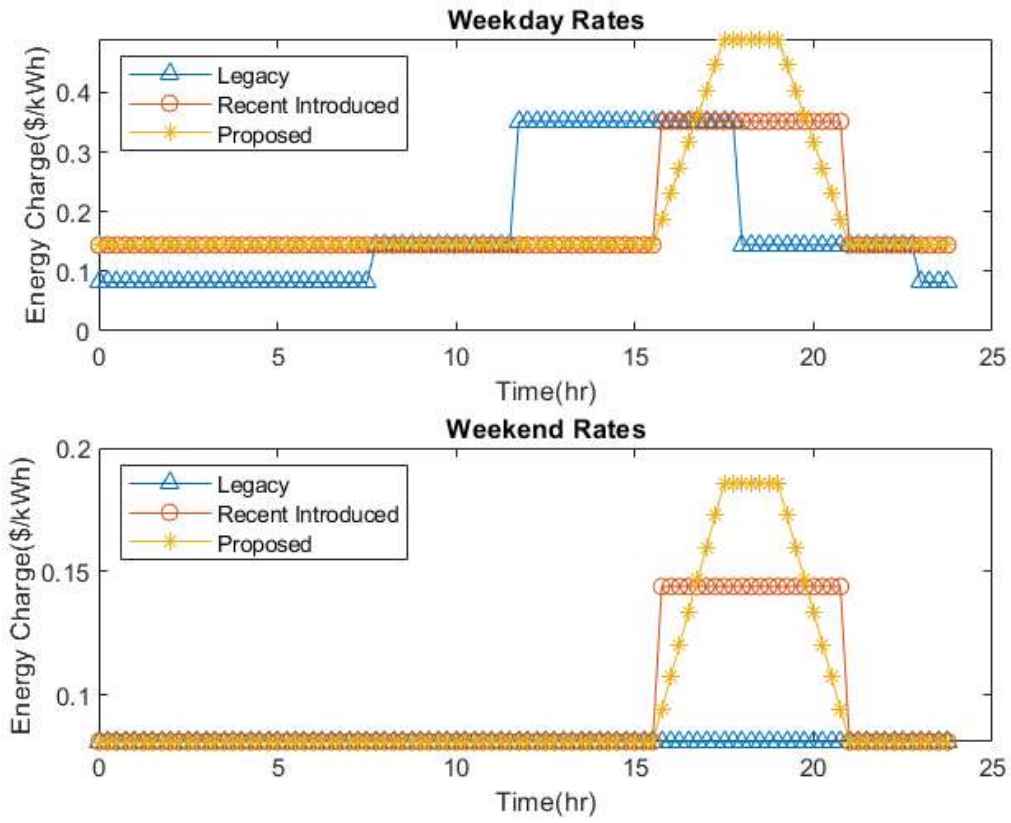

Figure 3-7 Legacy, Recent Introduced and Proposed Rate

From this figure we see that, in both of the legacy and recently introduced rate, the change in energy price takes place as a large step. Instead, the proposed dynamic rate increases the value linearly for a duration of time, followed by a steady value and finally decrease linearly again for the remaining time, all within the highest cost On-Peak period. The particular durations maybe chosen by the utilities according to the needs of the system resource constrains and Duck Curve requirements. As an example, we have chosen the following dynamics and durations for this study: linear rate increase in the first two hours, then steady rate value for the next hour and decrease linearly again for the last two hours within the ON-Peak period in our proposed rate. This way a sharp change in energy price is avoided and smoothing effect is brought into the price change. To make the proposed rate equivalent to the recent introduced one, we define the On-Peak price in weekdays in a way so that for same energy use within the period, the total energy cost would be same. We do that by keeping the area under the curve during this 5 hour, 4 PM to 9 PM period, same for both cases. As mentioned earlier in this section, during the weekend the same 5 hour time period is considered as Mid-Peak prices. For optimization purposes this weekend Mid-Peak prices follows the same methodology as weekday's On-Peak prices.

The steady On-Peak price for the 6 PM to 7 PM period, $\alpha^{On,proposed}$ can be found by:

$$\frac{1}{2}\left(\alpha^{On,proposed}-\alpha^{Mid}\right)(24\Delta t)=\left(\alpha^{On}-\alpha^{Mid}\right)(20\Delta t) \tag{3.41}$$

By solving equation 3.41 we get:

$$\alpha^{On,proposed}=\frac{5\alpha^{On}-2\alpha^{Mid}}{3} \tag{3.42}$$

For our proposed rate, the energy cost at time step t during the 4 PM to 9 PM period on weekdays can be modified as:

$$\alpha_t = \begin{cases} \alpha^{Mid} + \dfrac{\left(\alpha^{On,proposed} - \alpha^{Mid}\right)}{8}(t-64), 64 \le t < 72 \\ \alpha^{On,proposed}, 72 \le t \le 76 \\ \alpha^{On,proposed} + \dfrac{\left(\alpha^{On,proposed} - \alpha^{Mid}\right)}{8}(t-84), 76 < t \le 84 \end{cases} \quad (3.43)$$

Similarly, we can define the Mid-Peak Prices in weekends during similar 4 to 9 PM period.

The daily average net load after optimization for these three rates are shown in figure 3-8.

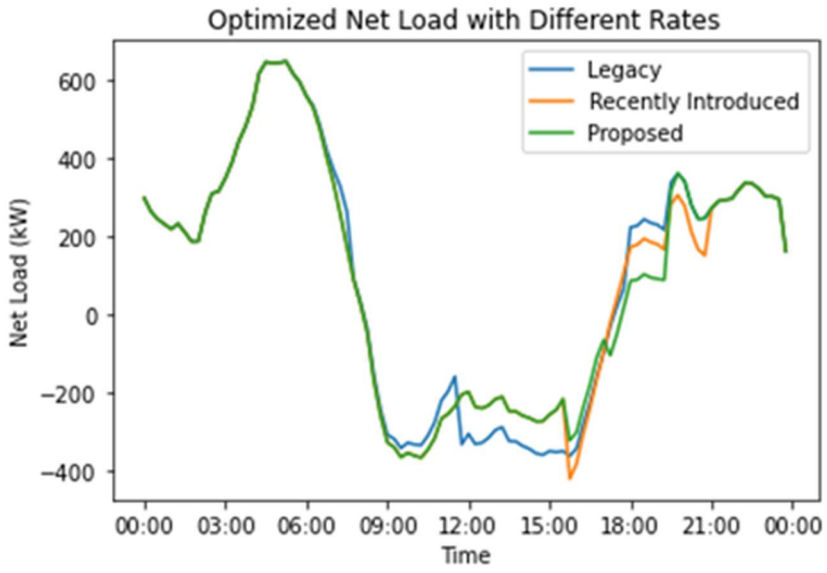

Figure 3-8 Optimized Net Loads for the Three TOU Periods

CAISO uses the three-hour ramp rate between 4 PM and 7 PM to assess the severity of the ramp rate requirements of the Duck Curve. The same three-hour ramp rates of the optimized daily average net load for the three rates are presented in table 3-7.

Table 3-6 Three Hour (4PM to 7PM) Ramp Rate for the Three Rates

Rate	Three Hour Average Ramp (kW)
Legacy	572.92
Recent Introduced	561.8
Proposed	393.1

As we can see from figure 3-8 and table 3-6, the recent introduced rate does not help much in reducing the ramp rates (2% decrease) while the proposed rate shows a significant improvement (31% decrease) over the other. This is due to the fact that step change and steady value of the legacy and recent introduced rate drives the BESS to discharge power with a sharp change at the transition time between the periods and then continues discharging power at a steady rate. In contrast, a linearly changing rate enables BESS to increase or decrease the discharging power gradually which helps to reduce the fast ramp rate of the net load or the Duck Curve. Utilities can introduce the proposed rate for the commercial buildings with solar and BESS to offset the high Duck Curve ramp rates.

One possible real-world application of this proposed novel rate could be the prevention of the rotating blackouts discussed in chapter 2. To satisfy grid requirements better, a coordinated operation of the battery and other DER assets is required. By implementing the proposed tariff to the large commercial users with BESS and other DERs, the cost optimization of the net load can assist the utilities in adjusting their operations on high demand days, thereby avoiding similar blackouts in future.

3.4 Modeling and Optimization of Commercial Building Heating, Ventilation and Air Conditioning (HVAC) Loads

3.4.1 System Description

The building considered here is a commercial building situated in the University of California, Riverside's (UCR) research facility called College of Engineering - Center for Environmental Research and Technology (CE-CERT). It is used as office spaces for research staff, administrators, and students along with multiple conference rooms. The area of the building is about 20,000 square feet and is one-storied. The whole building is divided into 16 thermal zones where each zone is served by one HVAC unit. The zones vary in size, occupancy, and types of activities depending on the purpose of use. Zone 1 to 7 and zone 11 are used as office spaces for the research staff. Zone 8 is the lunchroom. Zone 9 and 12 are used for conference meeting purposes with medium and small gatherings respectively. Zone 10 is used as office space by the administrative staff. Zone 13 is the copier room. Zone 14 contains the reception area and a small library. Zone 15 is used as the server room for keeping the IT equipment. Figure 2 shows the layout of the building and the various thermal zone areas. The colors are provided for presenting the separation among different zones. Symbols mean that they are used for office purposes and level of occupancy.

Figure 3-9 Building layout and thermal zones

3.4.2 Modeling of the System

3.4.2.1 Heat Balance Equation for the Zones

The thermal load that must be served by the HVAC system at any instance in a particular zone at a certain temperature is equal to the sum of heat gains from different sources in that zone at that instance for that zone temperature. The main sources of heat gain in a typical commercial building include the people, outside environment, equipment, and lighting. So, the heat balance equation for a zone at any instance can be written as:

$$\dot{Q^t_{load,k}} = \dot{Q^t_{light,k}} + \dot{Q^t_{ppl,k}} + \dot{Q^t_{eqp,k}} + \dot{Q^t_{env,k}} \quad (3.44)$$

Where,

$\dot{Q^t_{load,k}}$ = Required thermal load at time t for zone k, W

$\dot{Q^t_{light,k}}$= Heat gain from lights in zone k at time t, W

$\dot{Q^t_{ppl,k}}$ = Heat gain from people in zone k at time t, W

$\dot{Q^t_{eqp,k}}$= Heat gain from equipment in zone k at time t, W

$\dot{Q}^{t}_{env,k}$= Heat gain from the outside environment in zone k at time t, W

3.4.2.2 Heat Gain from Lights

According to a study by U.S. Energy Information Administration (EIA), ten percent of the total building load is consumed by the lighting system for a commercial building and fluorescent lights are the most dominating of the light sources [110]. Twenty percent of the total electrical input of typical fluorescent lights is converted into visible radiation and the rest are converted into radiative and convective heat gain [111]. Using this information, the lighting gain for the zones are calculated by distributing the lighting power according to the square footage and illuminance requirement, based on the window luminance provision of each zone. Authors acknowledge the fact that reference 16, EIA's Commercial Buildings Energy Consumption Survey 2012 (CBECS 2012), used data from surveys conducted in 2013 and is representative of commercial buildings in 2012. There have been some changes in the lighting system of a building in the meantime such as retrofit buildings with LED bulbs. But CBECS 2012 still remains the most updated and reliable source of building energy consumption as CBECS 2018 has not been released yet.

3.4.2.3 Heat Gain from People

Due to human metabolism, heat is generated from the occupants of a building which acts as one of the heat gain sources in a zone. The sensible (radiation plus convection) heat gain from occupants is a complex function of metabolic rate and environmental conditions which is modeled by fitting a polynomial curve using the heat gain data of different temperatures and average adjusted metabolic rates [112]. The sensible heat gain of a typical adult male can thus be expressed as:

$$S = 6.461927 + 0.946892M + 0.0000255737M^2 + 7.139322T - 0.0627909TM + 0.0000589172TM^2 - 0.19855T^2 + 0.000940018T^2M - 0.00000149532T^2M^2 \quad (3.45)$$

Where,

M= Metabolic rate, W

T=Surrounding air temperature, ℃

S=Sensible heat gain

Though metabolic rate can vary from person to person, the average metabolic rates for different activities for a person do not vary widely and is used for this modeling [113]. The average metabolic rate for an adult male doing office activities is 126 W. While the average for an adult female is typically 0.85 times the average metabolic rate of an adult male. Using this information the sensible heat gain equation for males and females in an office building is as follows:

$$S_{male} = 126.18 + 0.16T - 0.104T^2 \quad (3.46)$$

$$S_{female} = 108.167 + 1.09T - 0.115T^2 \quad (3.47)$$

If T was in Fahrenheit instead of Celsius then the equations would be:

$$S_{male} = 90.564 + 2.137T - 0.032T^2 \quad (3.48)$$

$$S_{female} = 52.433 + 2.878T - 0.0356T^2 \quad (3.49)$$

So, the heat gain of a zone from people can be expressed as:

$$\dot{Q}^t_{ppl,k} = \left(90.564 + 2.137T^t_{z,k} - 0.032{T^t_{z,k}}^2\right) N^t_{male,k} + \left(52.433 + 2.878T^t_{z,k} - 0.0356{T^t_{z,k}}^2\right) N^t_{female,k} \quad (3.50)$$

Where, $N^t_{male,k}$ and $N^t_{female,k}$ is the number of males and females in zone k at time t, respectively and $T_{z,k}$ is the temperature of zone k at time t in Fahrenheit.

Figure 3 shows the occupancy profiles of the different zones on weekdays. Zones 1-7 and 11 are office spaces used by research staff and are typically occupied at regular hours and partially occupied after office hours. Zone 8 is the lunchroom. Zone 10, 14, and 15 are used by the administrative staff and follow the regular office hour pattern. Zones 9, 12, and 13 are normally unoccupied and used only if needed for a brief period, thus they have no regular occupancy pattern. The occupancy of these zones is assumed zero here. On weekends and holidays, the building is usually unoccupied and the occupancy of all the zones on those days is assumed zero.

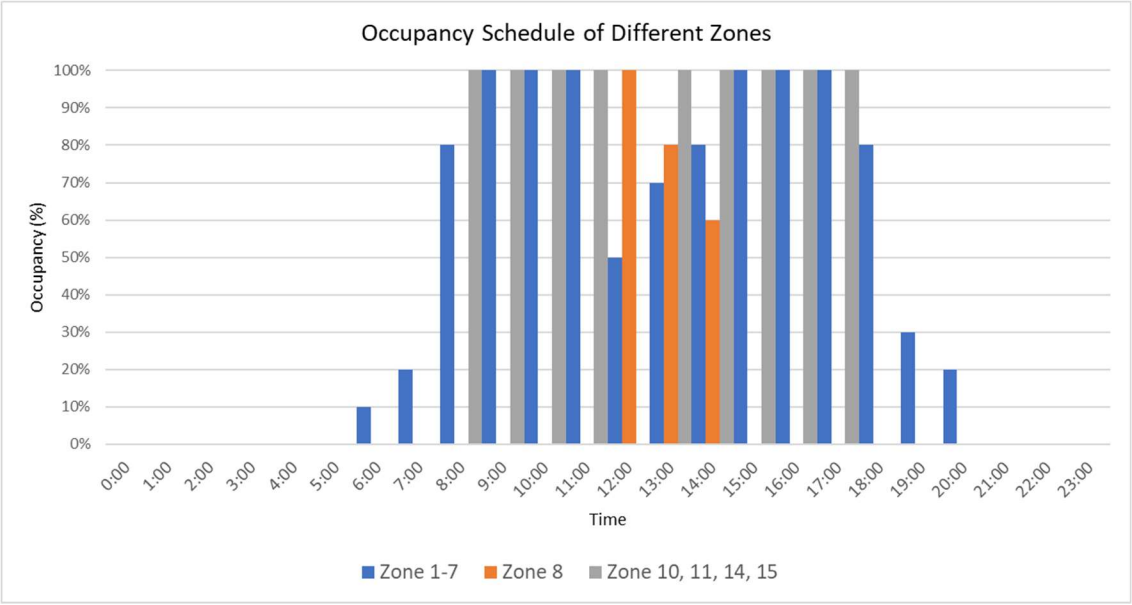

Figure 3-10 Occupancy Profile of Different Zones

3.4.2.4 Heat Gain from Environment

Heat conduction from outside can be modeled in several ways such as the state-space model and the Laplace method [114-115]. These methods can generate the transient behavior of heat conduction through the walls. But these models require detailed information such as wall design and construction materials. Since we use one minute timestep in our analysis, it is rational to assume that the heat conduction behavior does not change much within this period and we can use a simplified linear model instead [116]. This method uses an overall heat transfer coefficient that captures the aggregated effect of a multilayered wall composed of various materials of different heat transfer coefficients. The heat gain from the outside environment through conduction of walls can be found by:

$$\dot{Q^t_{env,k}} = \frac{5}{9} U_k A_k \left(T^t_{out} - T^t_{z,k}\right) \tag{3.51}$$

where,

U_k= Overall heat transfer coefficient of the wall in zone k exposed to the outside environment, W/(m^{2}K)

A_k= Area of the wall in zone k exposed to the outside environment, m^2

T^t_{out} = Outside temperature at time t, °F

Factor $\frac{5}{9}$ comes due to the conversion of Fahrenheit to Kelvin. The convenience of this model is that the overall heat transfer coefficient of common building elements can be easily found in reference [116] which relieves us of the need to know the types of wall construction and design. The overall heat transfer coefficient is calculated by using the following equation [117]:

$$\frac{1}{U} = \frac{1}{h_i} + \frac{d}{k} + \frac{1}{h_o} \tag{3.52}$$

where,

h_i= Convection heat transfer coefficient of fluid surrounding inside wall, W/(m^{2}K)

h_o= Convection heat transfer coefficient of fluid surrounding outside wall, W/(m^{2}K)

k = Thermal conductivity of the wall, W/(mK)

d = Wall thickness, m

3.4.2.5 Heat Gain from Equipment

Several research projects conducted by the American Society of Heating, Refrigeration, and Air-Conditioning (ASHRAE) and other researchers listed the heat gain values from different equipment that are found in a typical office building [118]. A survey was conducted to find out what types of equipment and appliances existed in each zone and their quantity. Then heat gain from the equipment was calculated for each zone using this information and validated with [118].

3.4.2.6 HVAC Fan Power and Cooling Load

To meet the zone conditioning requirements the HVAC system must provide the cooling or heating load needed by the zone. This can be modeled with the equation:

$$\dot{Q^t_{load,k}} = Q^t_{sys,k} = \frac{5}{9} C_p \rho (\eta_c \dot{V_{max}})(T_{z,k} - T_{sup}) \tag{3.53}$$

where,

$Q^t_{sys,k}$= Cooling power provided to zone k at time t by the HVAC system, W

C_p= Air specific heat, J/(kg.K)

ρ= Air density, kg/m^3

η_c=Cooled air supply fraction

$\dot{V_{max}}$= Maximum airflow from the air control system, m^3/s

T_{sup}= Cooling coil supply temperature, °F

The HVAC fan power is given by:

$$P_{fan} = \frac{(\eta_c \dot{V_{max}})\Delta Pr f_{pl}}{\varepsilon} \tag{3.54}$$

where,

P_{fan}= HVAC electrical input fan power, W

ΔPr= Fan design pressure rise, Pa

f_{pl}= Fan part load factor

ε= Fan efficiency

We can now write the thermal load requirement as:

$$\dot{Q_{load,k}} = \frac{5}{9} C_p \rho \frac{P_{fan}\varepsilon}{\Delta Pr f_{pl}} \left(T_{z,k} - T_{sup}\right) \tag{3.55}$$

If there are multiple HVAC units in the zone, then the previous equation can be written as:

$$\dot{Q^t_{load,k}} = \frac{5}{9} C_p \rho \left(\sum_{j=1}^{N_{Fan,k}} \frac{P^t_{Fan,k,j}\varepsilon_{k,j}}{\Delta Pr_{k,j} f_{pl,k,j}}\right)\left(T^t_{z,k} - T_{sup}\right) \tag{3.56}$$

where, $N_{Fan,k}$ denotes the number of fan units in zone k.

3.4.3 Optimization Problem Formulation

Based on the modeling of the system an optimization problem has been formulated that aims to minimize the total fan power of all the zones. We need to find the optimal zone

temperature setpoint $T_{z,k}^{t}$ and for each of the zones and fan power $P_{Fan,k,j}^{t}$ for all the HVAC fan units for all instances. For each time step t= 1, 2,……T and zones k=1,2,….. N_{zone} the optimization problem can be written as:

$$\min_{T_{z,k}^{t}, P_{Fan,k,j}^{t}} \left(\sum_{k=1}^{N_{zone}} \sum_{j=1}^{N_{Fan,k}} P_{Fan,k,j}^{t} \right)$$

Subject to:

$$\dot{Q_{load,k}^{t}} = \dot{Q_{light,k}^{t}} + \dot{Q_{ppl,k}^{t}} + \dot{Q_{eqp,k}^{t}} + \dot{Q_{env,k}^{t}} \quad (2.38)$$

$$\dot{Q_{ppl,k}^{t}} = \left(90.564 + 2.137T_{z,k}^{t} - 0.032{T_{z,k}^{t}}^{2}\right) N_{male,k}^{t} + \left(52.433 + 2.878T_{z,k}^{t} - 0.0356{T_{z,k}^{t}}^{2}\right) N_{female,k}^{t} \quad (2.44)$$

$$\dot{Q_{env,k}^{t}} = \frac{5}{9} U_k A_k \left(T_{out}^{t} - T_{z,k}^{t}\right) \quad (2.45)$$

$$\dot{Q_{load,k}^{t}} = \frac{5}{9} C_p \rho \left(\sum_{j=1}^{N_{Fan,k}} \frac{P_{Fan,k,j}^{t} \varepsilon_{k,j}}{\Delta Pr_{k,j} f_{pl,k,j}}\right) \left(T_{z,k}^{t} - T_{sup}\right) \quad (2.50)$$

$$T_{low} \leq T_{z,k}^{t} \leq T_{high} \quad (2.51)$$

$$P_{minFan,k,j} \leq P_{Fan,k,j}^{t} \leq P_{maxFan,k,j} \quad (2.52)$$

where,

T_{low}= Lower temperature limit of thermal comfort, °F

T_{hig} = Lower temperature limit of thermal comfort, °F

$P_{minFan,k,j}$= Minimum fan power of fan unit j in zone k, W

$P_{maxFan,k,j}$= Maximum fan power of fan unit j in zone k, W

The constraints 1, 7, 8 and 13 in the optimization problem stems from the system thermal model discussed in the previous section. Constraint 14 makes sure that the temperature set points in each zone stay within the range of human thermal comfort all the time. A minimum amount of airflow must always be maintained, so the fan units must draw

a minimum amount of power. Also, they cannot go beyond their rated input power. Constraint 15 states these conditions. Constraint 7 is a quadratic equality constraint and constraint 13 has a bilinear term in it. On top of that, the temperature setpoint variables are integers, since we can not set them to a fractional value in real systems. Constraint 7, 13 and the integer variables make the optimization problem nonconvex. Previously it was not possible to solve this type of nonconvex problem and find a globally optimum solution. The optimization solver Gurobi 9.0 version has the ability to solve optimization problems to the global optimum solution with these types of nonconvexities [119]. The problem was modeled with Gurobi 9.0 in the Python environment and solved. The configuration of the computer used was: 64 bit Intel Core i-7 3.2GHz processor with 16 GB RAM and 12 GB NVIDIA GeForce GPU.

3.4.4 Results

The optimization problem was simulated on 90 minutes of data using the outside temperature profile of August 30, 2019, from a nearby weather station. The weather station provides temperature data of 1-hour intervals for some part of the day and 20-minute interval data for other parts. Here, we have used 20-minute interval data of 90-minute duration and applied linear interpolation to get 5 minutes interval data. It was assumed that the temperature stays stable within any 5 minute period. Unoptimized data were collected through commercially available open-source components, which perform the control and data acquisition of the HVAC units and building thermal zones. Figure 4 shows the resulting HVAC load profile for optimized and unoptimized data.

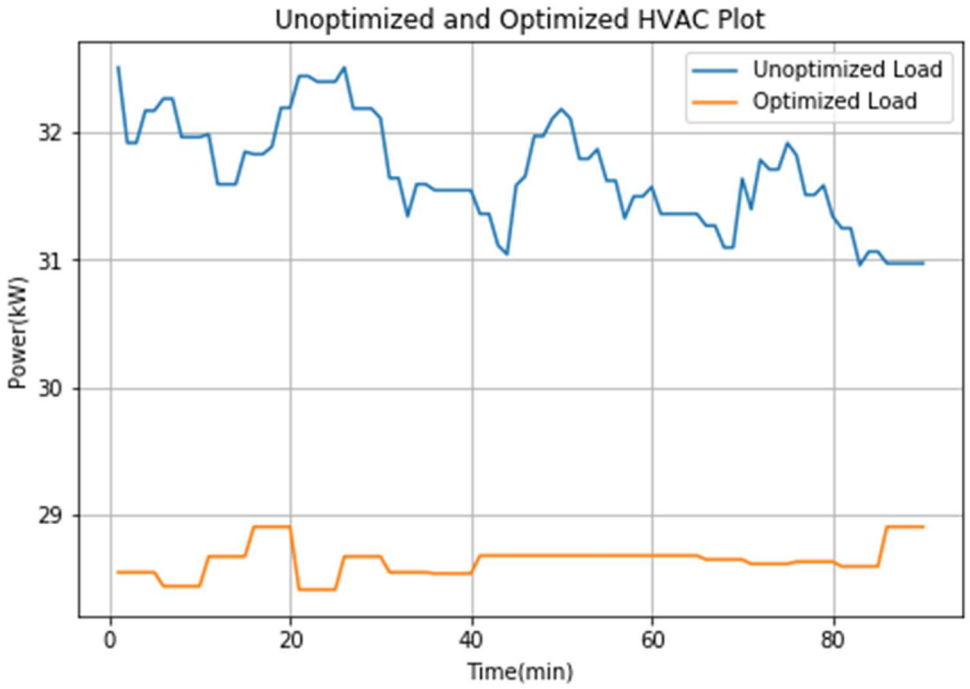

Figure 3-11 Unoptimized and Optimized HVAC Load in kW

The unoptimized load consumes 47.53 kWh, whereas, the optimized load consumes 45.66 kWh in this 90 minute period that results in an energy savings of 3.91%. The peak for the unoptimized and optimized load is 32.51 kW and 30.72 kW respectively, which provides a 5.55% peak reduction. Figures 5 and 6 respectively show the unoptimized and optimized zone temperature setpoints. As we can see from these figures the optimized zone temperature setpoints are mostly higher than that of the unoptimized one, though they still are within the range of human thermal comfort. It can also be seen that the unoptimized set points frequently change while the optimized ones result in a more stable and consistent profile.

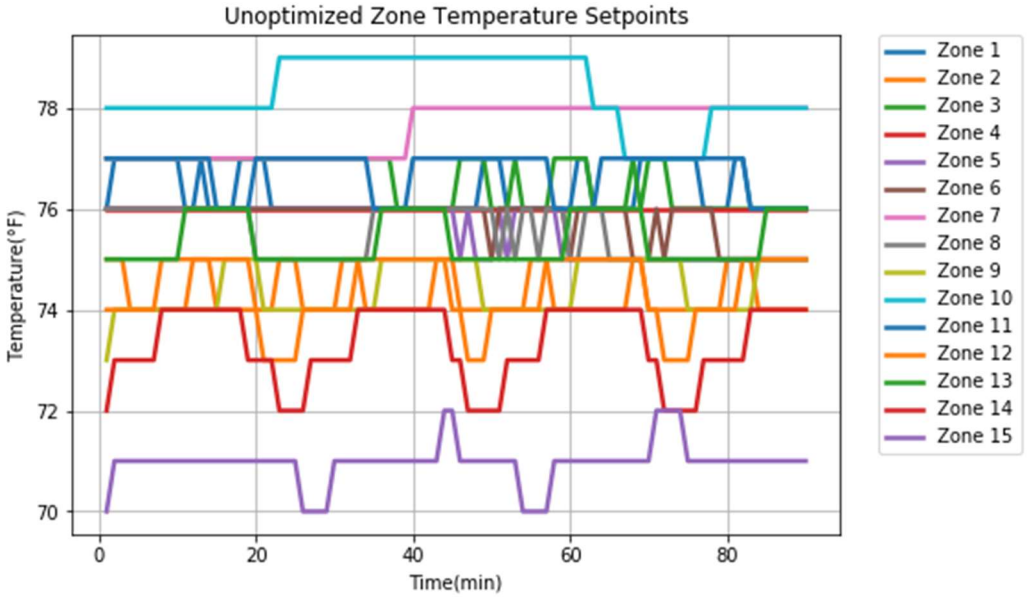

Figure 3-12 Unoptimized zone temperature setpoints

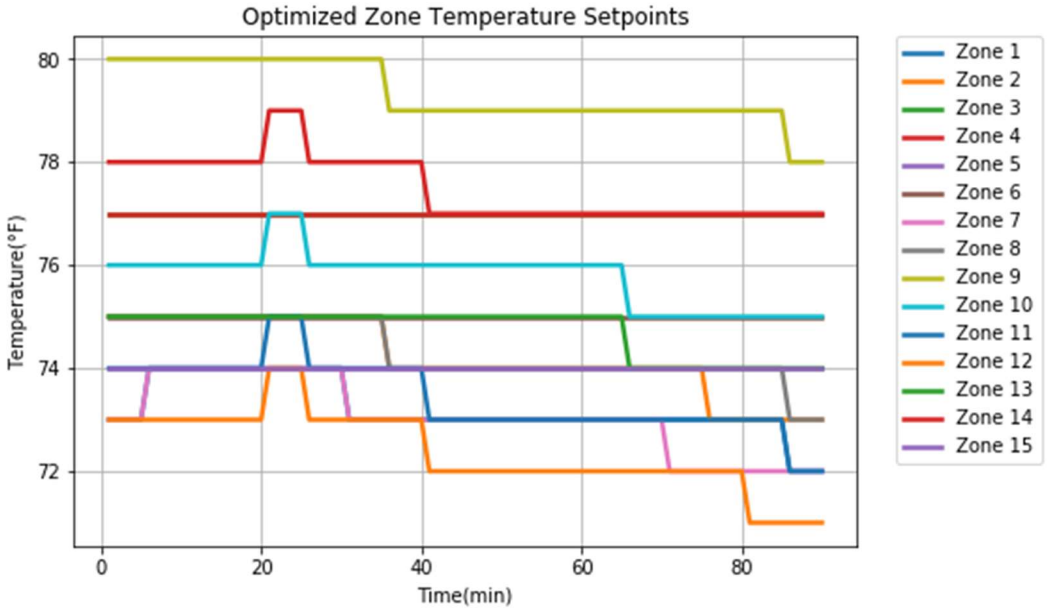

Figure 3-13 Optimized zone temperature setpoints

Zone 15 is an IT server room where the maintenance of the required lower temperature is a more important factor than human thermal comfort and thermal setpoint requirements are different from other zones. The optimization problem is run again excluding zone 15 and the resulting load profile is presented in figure 7. The energy savings in this scenario is 3.71% and the peak reduction here is 5.45%.

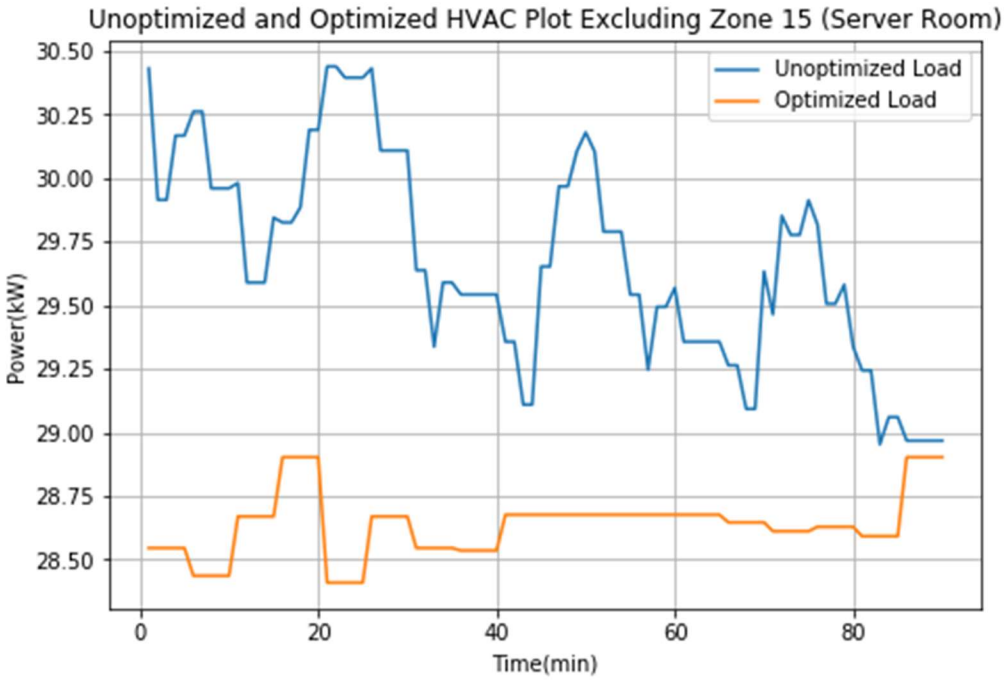

Figure 3-14 Unoptimized and Optimized HVAC Load excluding Zone 15

The savings from the optimization results in both economic and environmental benefits. For example, if the percentage of energy savings documented in the first case above can be implemented throughout the US, then a total of 13.62 billion kWh energy consumption will be reduced per year. The average price per kWh of electricity in the commercial sector of the US is 10.66 cents [120]. The total annual dollar saving would be $1.45 billion for this price rate. Commercial Air Conditioning is responsible for

approximately 125,000 MW of the total peak load in the US. The 5.55% peak reduction attained in the case above would facilitate a peak demand reduction of 6,891 MW. Though demand charge varies highly among regions, utilities, and customer types, the average maximum demand charge in the US is $15.07/kW, which is equivalent to $1.246 billion worth of savings each year [121]. In addition, reducing peak demand relieves transmission line congestion and avoids the construction of additional transmission lines and new generation facilities. The kWh savings also helps the environment by reducing 611 million kg of CO_2 emission [122].

3.5 Conclusions

In this chapter, a comprehensive optimization framework has been developed for commercial buildings equipped with DERs such as solar generation and BESS, to capture the diversity in utility tariff types. The utility tariffs were categorized into six universal commercial tariff types. Then, for each of the types, a cost function was formulated which were used to construct a universal cost function. Using this cost function and the system model an optimization problem was formulated along with an algorithm to apply it on commercial buildings with solar generation and BESS to generate the optimal BESS operation profile. The optimization was done on four buildings using all of the categorized types. Results showed that TOU demand charges and CPP charges cause higher unoptimized costs. High On-Peak energy values with noon to evening On-Peak periods provide higher savings from solar generation. TOU energy charge with single monthly peak demand provides the best savings from BESS optimization while TOU demand charges reduce such savings. Adding BESS with solar would also be beneficial for

commercial buildings under CPP tariffs. Flat energy rates with monthly peak demand provide the lowest BESS optimization savings as the only possible savings is from peak reduction whereas other tariffs also provide savings opportunity from energy shifting.

Different changes in utility tariffs were also analyzed to examine their impact the optimization. The price change analysis revealed that adding solar alone is more beneficial than adding BESS with it if the energy charge increase is dominant. Comparison is drawn between impacts of demand charge heavy and energy charge heavy tariffs on high and low load factor buildings. It showed that buildings with low load factor can lower their costs under energy heavy option and buildings with high load factor can do that by choosing demand heavy option. Buildings with low load factor can achieve considerably higher savings percentage by adding solar in either option than a buildings with high load factor. Contrary to common perception any noticeable difference in percentage savings from BESS was not identified for building with high or low load factor. Though it was confirmed that under energy heavy charges savings from solar was higher while savings from BESS was higher under demand heavy charges. The shifts in time periods were also analyzed. The results revealed that the new rate introduced by the utilities does not help much to achieve the intended flexible ramping in the net load "duck curve" feature. While the rate proposed in this paper offers a significant improvement over that.

This chapter also presented detailed thermal modeling for a multi-zone commercial building with VAV type HVAC units. A nonconvex optimization problem was formulated to model the VAV type HVAC extensively. The aggregated power consumption of the HVAC units is minimized by using that model. The results exhibited that fair amount of

energy and peak reduction can be achieved through the optimization. On top of that, the zone temperature setpoints became more stable as a consequence of the optimized operation while not violating the temperature limit of human thermal comfort. The energy and peak reduction obtained from the optimization can further reduce the energy consumption and peak demand which can lead to economic and environmental benefits through dollar savings, CO2 emission reduction. In addition, peak reduction also help prevent blackouts.

4 Data Driven Maintenance and Monitoring of DER Component of a Commercial Building Microgrid: Battery Energy Storage System

4.1 Background and Problem Statement

Previous chapter presented optimization of commercial building loads using DERs. The DER component that implemented the optimization strategy was the BESS. Regular maintenance is required for assuring proper functioning of BESS. While savings from the electricity cost optimizations helps in offsetting the investment cost of DERs, proper maintenance and monitoring can help increase the life of DERs and make sure they keep generating savings for a long time.

As discussed in chapter 2, the maintenance of BESS is an important issue for reliable and safe operation. But most works are on the online fault detection while predictive maintenance can help prevent any major failures during critical operating times. The few works that are on the predictive maintenances consider only the electrical property or need interruption of regular operation. Predictive maintenance through identification of bad cells in the BESS that uses easily available data and doesn't require interruption of operation is hence useful for proper BESS operation.

For SOC estimation of BESS, machine learning methods have been discussed. In those works the use of conventional and nonconventional features have also been discussed. Some of the features mentioned, which are present in both conventional and nonconventional approaches, are highly correlated. Sometimes this leads to a phenomenon

called multicollinearity. Ridge regression and lasso regression methods have shown to give good performance in case of multicollinearity [90-91]. But these methods have not been explored for SOC estimation.

Section 2 of this chapter proposes a method for bad cell identification by using actual thermal and electrical property data from a Utility-Scale BESS through a probabilistic approach for predictive maintenance. A detailed formulation is presented for the development of the proposed method. Then an analysis is done by utilizing the data from a utility-scale BESS and the results obtained from the analysis are exhibited. All of the topics mentioned above are discussed in detail in different subsections of section 4.2.

In section 4.3, the effects of lasso and ridge regression methods are studied along with the other methods mentioned and their performance comparison is presented to see which method gives the best results for SOC estimation. Both conventional and non-conventional features have been used for this study. The easily available conventional features like voltage, current, etc. and the selected non-conventional features suggested in [82] are derived and applied to see how their performance varies.

4.2 Predictive Maintenance through Identification of Bad Cells by Statistical Analysis of Electrical and Thermal Properties

4.2.1 Methodology

The key properties of cells in BESS can be classified among three major groups. These are:

a) electrical properties,

b) thermal properties, and

c) chemical properties.

The electrical properties of a cell signify its operational performance. The thermal properties of a cell can indicate the risk of fire hazards. While the chemical properties of a cell can denote both of those along with cell aging and degradation. Any of the abovementioned types of properties can be used for the detection of a bad cell in a BESS. Though there are instruments available that can be used to test the chemical properties of a cell, these are highly expensive and usually capable of testing a single cell at a time, which makes routine testing costly and difficult. It also requires the cell under test to be electrically isolated from the rest of the BESS, which makes the process even more inconvenient.

Typically, most of the BESS used in utility-scale applications integrate BMS for monitoring and recording the performance and safety of the battery operation. Almost all of them measure and log individual cell voltage and cell temperature data. Cell voltage and cell temperature rise rate can be labeled as the most important electrical and thermal property of a BESS cell, respectively, and can be used for the analysis to identify the bad cells. As BMS collects and stores the data required for the analysis, the tedious process of going through testing all the cells individually to carry out predictive maintenance of the BESS is not required. Accessing the logged data from the BMS and analyzing them using the method described in subsection 4.2.2 is sufficient for this purpose. Thus, the bad cell identification process is made much easier. Moreover, it also eliminates the possibility of human error, making the process more refined. While cell voltage data can be readily

available and accessible, the cell temperature rise rate can also be calculated very easily using the recorded data at a number of timestamps.

The proposed method uses the cell voltage and cell temperature data to perform a statistical analysis of how an individual cell is staying within the manufacturer specified limits of these properties or how they are varying compared to other cells. The University of California, Riverside's research facility College of Engineering- Center for Environmental Research and Technology (CE-CERT) has its own utility-scale 100 kW/500 kWh BESS. The BESS has a total of 143 Li-ion cells connected in series, each having a capacity of 1000Ahr. The BESS is monitored through an integrated BMS. The BMS collects cell voltage and cell temperature data using voltmeters and thermistor modules and logs them every one minute. Logged data are stored on CE-CERTs own database server. Using these data, the statistical analysis is executed. The formulation for the analysis is shown in the next subsection along with the algorithm to calculate the cell temperature rise rates.

4.2.2 Formulation for Analysis

Let us assume we have N number of cells in the BESS considered and we are analyzing the data recorded in total T number of timestamps. Each of the cells is assigned a unique cell ID i =1,2,…..*N*, and the timestamps are labeled as t =0,1,……*T*-1. We can define two sets containing the cell IDs $\boldsymbol{C}$ and timestamps $\boldsymbol{T}$ as:

$$\boldsymbol{C} = \{1,2, \dots \dots, N\} \tag{4.1}$$

$$\boldsymbol{T} = \{0,1, \dots \dots, T-1\} \tag{4.2}$$

4.2.2.1 Cell Temperature Rise-Rate Analysis

Let the cell temperature data for an individual cell having cell ID i at some timestamp t be $\theta_i(t)$ for total N cells and T timestamps where $i \in \boldsymbol{C}$ and $t \in \boldsymbol{T}$. The problem with the BMS data is that all the $\theta_i(t)$ can take integer values only. So, if we evaluate the temperature rise rates at each timestep, then we would only get zero values until the very timestep θ_i changes to a different integer value when a sharp change will be observed. Whereas the temperature may have been rising steadily over this duration of time. To obtain the actual rise rate at each timestep we propose an algorithm. By following the algorithm shown in figure 1, we can get the cell temperature rise rates $\Delta\theta_i(t)$ for N cells and T timestamps.

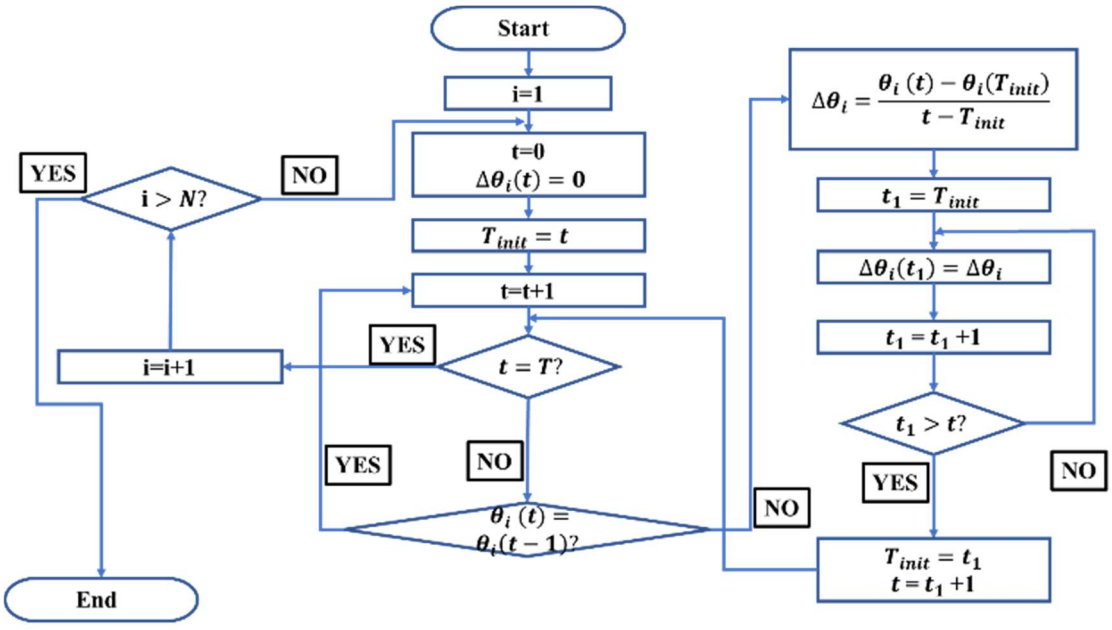

Figure 4-1 Algorithm to determine the cell temperature rise rates

In the algorithm the calculation of cell temperature rise-rates begins with cell ID 1. From timestep 0 it is checked if any change happens in the $\theta_i(t)$. A variable T_{init} is

initialized as zero as well as the value of $\Delta\theta_i(t)$. If any change is found in the value of $\theta_i(t)$ the cell temperature rise rate is calculated between the time T_{init} and current timestep *t*. Then the cell temperature rise-rates between T_{init} and *t* are updated with the calculated value. Then T_{init} is updated as the next timestep value and the current timestamp is advanced as the next value of updated T_{init}. Then this whole process is repeated for the cell until it reaches the final timestep. Then for each of the following cells the same process is carried out until the rise rates are calculated for all the cells.

After we have calculated the cell temperature rise rates $\Delta\theta_i(t)$ for all the cells and all timestamps we can define the set of cell temperature rise rates at some timestamp t as:

$$\Delta\boldsymbol{\theta}(t) = \{\Delta\theta_i(t) \mid i \in \boldsymbol{C}\} \tag{4.3}$$

We can find out the maximum cell temperature rise rate at some timestamp *t* using the following equation:

$$\Delta\theta_{max}(t) = \max_i(\Delta\boldsymbol{\theta}(t)) \tag{4.4}$$

Now the cell ID of the maximum cell temperature rise rate at that particular timestamp can be written as:

$$i_{max,\Delta\theta}(t) = arg\max_i \Delta\theta_{max}(t) \tag{4.5}$$

Let $f_i(t)$ be a function which determines if a cell ID i has the highest temperature rise rate at timestamp *t*:

$$f_i(t) = \begin{cases} 1, & i = i_{max,\Delta\theta}(t) \\ 0, & i \neq i_{max,\Delta\theta}(t) \end{cases} \tag{4.6}$$

Now let *I* be the random variable that represents the probability of the bad cell in the BESS. So, we can write the probability of i-th cell being bad as:

$$\mathbf{Pr}(I = i) = \frac{\sum_{t=0}^{T-1} f_i(t)}{T} \tag{4.7}$$

4.2.2.2 Cell Voltage Analysis

Let $V_i(t)$ represent the cell voltage for the cells in the BESS at some timestamp where $i \in \boldsymbol{C}$ and $t \in \boldsymbol{T}$.

In the BESS considered here, all the cells are in series connection. Then in this case the total voltage $V_{sys}(t)$ of the system at timestep *t* can be written as:

$$\sum_{i=1}^{N} V_i(t) \ = V_{sys}(t) \tag{4.8}$$

Ideally, all the cells should have the same voltage value at any time and should be equal to the average voltage of the system at that time. If the average voltage of the system at timestamp *t* is $V_{avg}(t)$, then in ideal case:

$$V_i(t) = V_{avg}(t) = \frac{V_{sys}(t)}{N} \qquad \forall i \in \boldsymbol{C} \tag{4.9}$$

But in reality, all the cells do not have the same voltage value at the same time. The deviation from average voltage for cell *i* at timestamp *t* can be defined as follows:

$$\Delta V_{avg,i}(t) = V_i(t) - V_{avg}(t) \tag{4.10}$$

These deviations of the cells must be within a reasonable range. The more they are out of this range, the more likely the corresponding cell is to degrade and be bad. We can determine this range from the distribution of these cell voltage deviation values.

Using all the voltage deviation values we can plot the probability density function (PDF) of it. Figure 4-2 shows the PDF of the cell voltage deviation of the BESS. We should note that, the PDF values here have values higher than one which is possible, contrary to

common perception [123]. The properties of PDF say that the values must be nonnegative and the area under the curve should be equal to one, which this distribution maintains. PDF is not a function that maps probability rather maps the rate of change of probability with respect to the random variable.

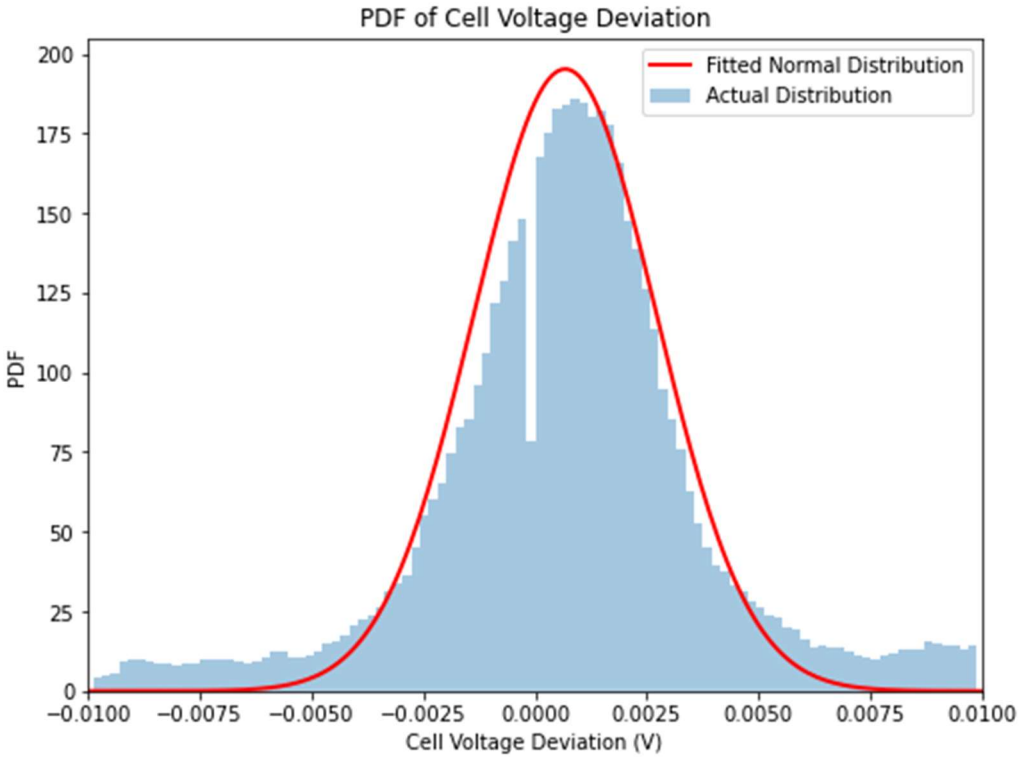

Figure 4-2 Actual and fitted distribution curve of cell voltage deviation

Since the shape of the PDF shown here resembles that of normal distribution, we can fit it with a normal distribution. We can assume that the cell voltage deviation follows the fitted normal distribution and write it as:

$$\Delta V_{avg} \sim N(\mu_{\Delta V}, {\sigma_{\Delta V}}^2) \tag{4.11}$$

Where, $\mu_{\Delta V}$ is the mean and $\sigma_{\Delta V}$ is the standard deviation of the cell voltage deviations. We can find the mean $\mu_{\Delta V}$ and the standard deviation $\sigma_{\Delta V}$ with the following formulae:

$$\mu_{\Delta V} = \frac{\sum_{t=0}^{T-1} \sum_{i=1}^{N} \Delta V_{avg,i}(t)}{TN} \tag{4.12}$$

$$\sigma_{\Delta V} = \sqrt{\frac{\sum_{t=0}^{T-1} \sum_{i=1}^{N} (\Delta V_{avg,i}(t) - \mu_{\Delta V})^2}{TN}} \tag{4.13}$$

We can validate our assumption through D'Agostino's skewness and kurtosis test for normality [124]. The coefficients of skewness and kurtosis $\sqrt{\beta_1}$ and β_2 are defined as follows:

$$\sqrt{\beta_1} = \frac{m_3}{m_2^{3/2}} \tag{4.14}$$

$$\beta_2 = \frac{m_4}{m_2^2} \tag{4.15}$$

Where, m_k is the k-th central moment which we can find using the following formula:

$$m_k = \frac{\sum_{t=0}^{T-1} \sum_{i=1}^{N} (\Delta V_{avg,i}(t) - \mu_{\Delta V})^k}{TN} \tag{4.16}$$

We can check the normality of the cell voltage deviation distribution by measuring how close the values $\sqrt{\beta_1}$ and $(\beta_2 - 3)$ are to zero. In this case $\sqrt{\beta_1} = -0.136$ and $(\beta_2 - 3) = -0.066$. So, the validity of our assumption is proved.

Now, as we have proven the normality of the distribution for the cell voltage deviations, we set the significance level α as 5%. For a two-tailed test, we find the critical

z-scores and consequently the limits of the range. Let the z score for 97.5% and 2.5% probability be $Z_{0.975}$ and $Z_{0.025}$, respectively. The lower limit $\Delta V_{avg,low}$ and the upper limit $\Delta V_{avg,up}$ can be found using the following equations:

$$\Delta V_{avg,low} = Z_{0.025} \times \sigma_{\Delta V} + \mu_{\Delta V} \tag{4.17}$$

$$\Delta V_{avg,up} = Z_{0.975} \times \sigma_{\Delta V} + \mu_{\Delta V} \tag{4.18}$$

We define a function $g_i(t)$ such that it shows if cell *i* at timestamp *t* violates this limit:

$$g_i(t) = \begin{cases} 1, & \Delta V_{avg,i}(t) > \Delta V_{avg,up} \; or \; V_{avg,i}(t) < \Delta V_{avg,low} \\ 0, & otherwise \end{cases} \tag{4.19}$$

The probability of *i*-th cell being bad can be represented as:

$$\mathbf{Pr}(I = i) = \frac{\sum_{t=0}^{T-1} g_i(t)}{\sum_{j=1}^{N} \sum_{t=0}^{T-1} g_j(t)} \tag{4.20}$$

4.2.3 Results

The analysis method described in subsection 4.2.2 was applied to the data from the BMS of the BESS mentioned in subsection 4.2.1. As it was mentioned earlier, the BESS in consideration is a property of a research center and is primarily used for research purposes. So, the operating hours and operation pattern change from time to time as required. A full month's data were collected when a research experiment was being conducted and the BESS operations with the grid were done more frequently. Figure 4-3 shows the state of charge (SOC) of the BESS for the month in consideration to give an idea about the operation. The sharp changes in SOC indicate charging or discharging operation at a very high rate while slow changes indicate operation at a lower rate.

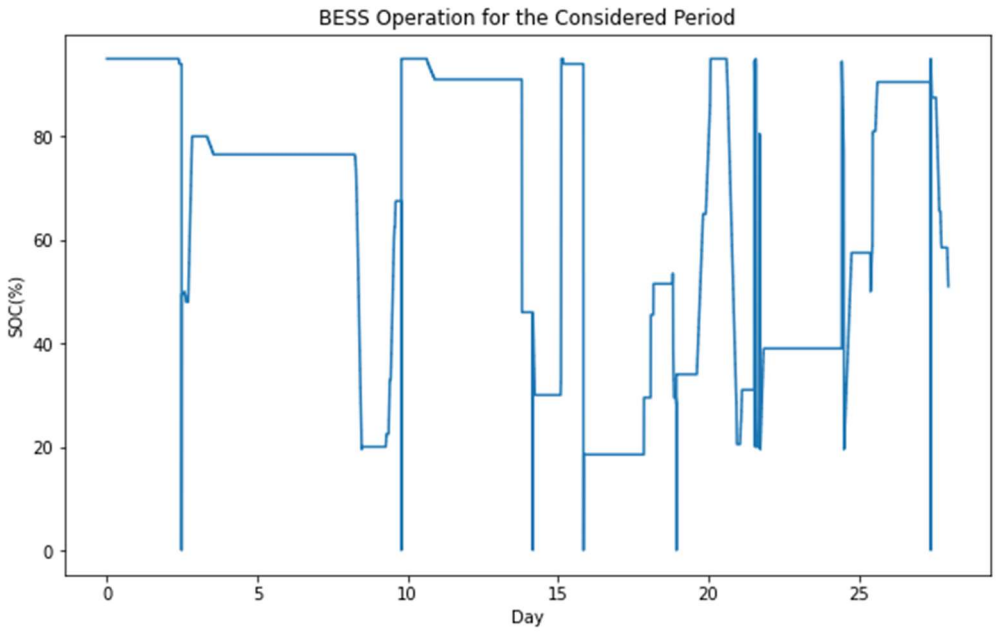

Figure 4-3 BESS Operation for the period considered for analysis

After collecting the cell temperature data for the period considered, the cell temperature rise rates were calculated using the algorithm shown in figure 4-1. Then, the cell temperature rise rates were used to analyze and find the probabilities of cells in the BESS being a bad cell. Figure 4-4 shows these probabilities from the cell temperature rise rate, i.e., thermal property analysis. We can see that cell 50 has the highest probability, 0.177 from the analysis which is a notably larger value than the probability of all the other cells. The other cells with a much lower probability than cell 50 but relatively higher than the rest of the cells are cell 71, 101, 102, and 125. Their respective probability values are 0.042, 0.049, 0.053 and 0.063.

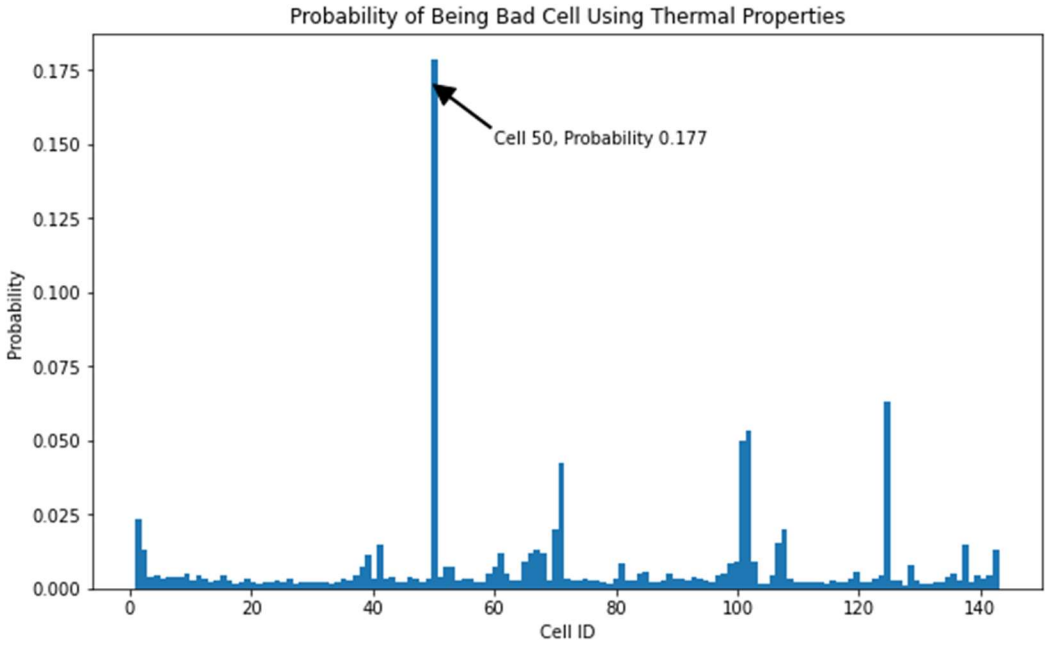

Figure 4-4 Probability of Being Bad Cell Using Thermal Properties

To validate our analysis cell temperature data for a heatwave day were collected when the BESS was non-operational, and the cell temperature rise rates were calculated using the algorithm in figure 4-1. The result showed that even without any BESS operation, only by gaining heat from the environment, cell 50 again had the highest number of occurrences for the cell which had the maximum cell temperature rise rate at any timestamp. This result is presented in figure 4-5.

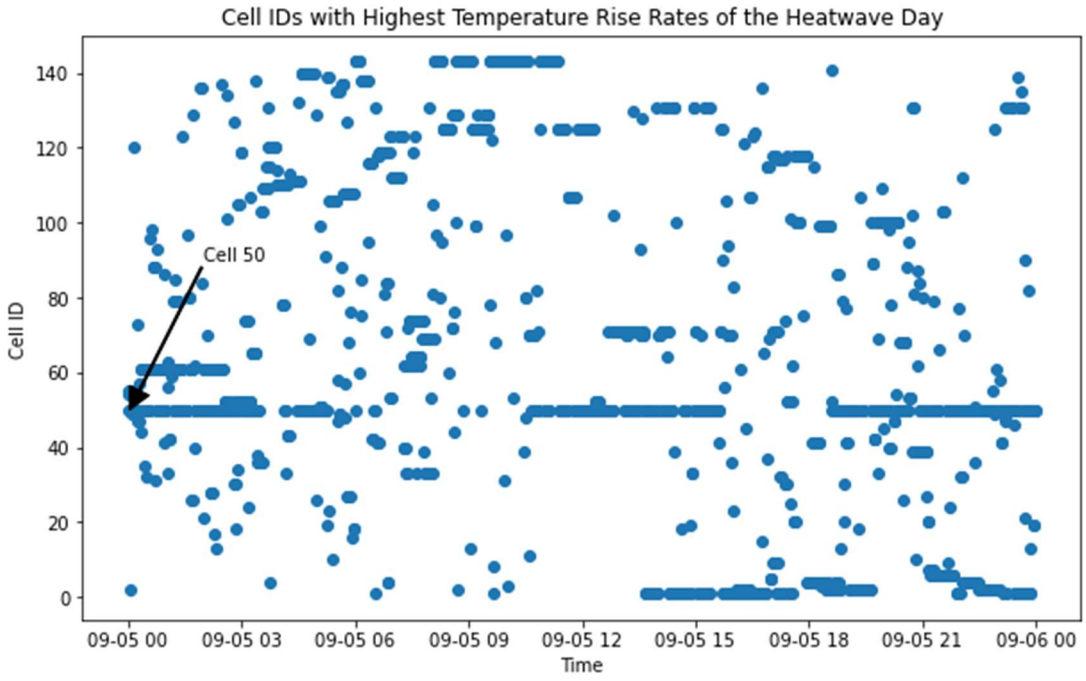

Figure 4-5 Cell IDs having the Highest Temperature Rise Rates of the Heatwave Day

Figure 4-6 shows the probabilities of the cells in the BESS being a bad cell by analyzing the electrical properties, i.e., cell voltage data. We can see that cell 122 is the most likely to be a bad cell with a probability of 0.278. The probability value is significantly higher than others, indicating it is a bad cell. The other cells that do not have as high a probability as cell 122 but still have a relatively higher likelihood of failure than the rest of the cells in the BESS are cell 28, cell 93, and cell 113 with probabilities 0.112, 0.116, and 0.13, respectively.

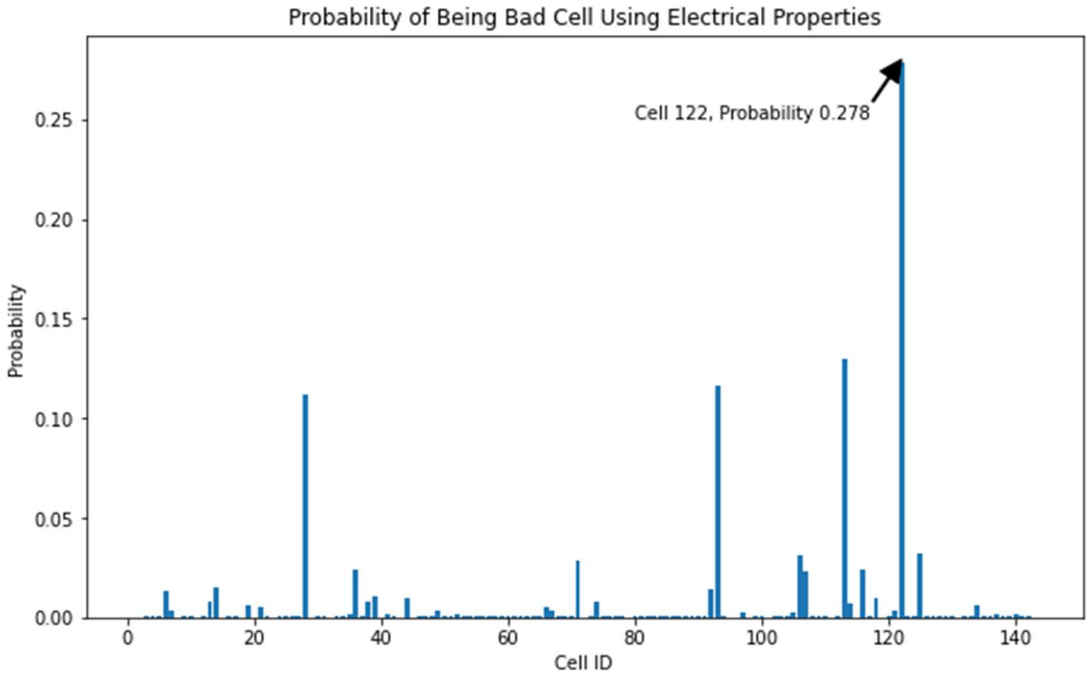

Figure 4-6 Probability of Being Bad Cell Using Electrical Properties

Cell 122 was tested for validation of the analysis, and it was found that it was a bad cell with reduced capacity. A replacement of the cell is being planned. Some of the possible reasons behind the thermal defect of cell 50 can be side reactions due to over-charging/over-discharging or internal/external short circuit, loose contact of the connector, over-deintercalation of anode, etc. [125]. Even though cell 50 is not under consideration for replacement at this moment, it is kept under close observation and will be replaced in the future.

According to a report published by the United States Department of Energy (DOE), the annualized operational and maintenance (O&M) costs for energy storage with Li-ion technology are $2.91/kWh and $11.47/kW [126]. So, for UCR's 100 kW/500kWh BESS, the O&M cost for each year would be $2,602. Assuming a 25-year expected life the total

cost incurred would end up being $65,050. For a larger Utility-Scale BESS with higher power and energy capacity, this cost can be significantly greater. This analysis has the potential to lower the O&M costs of a BESS by accomplishing effective predictive maintenance. Thus, it can offer huge economic benefits to customers who use BESS for cost reduction or take part in providing ancillary services to the grid. In addition, both utility companies and other parties with stakes in grid infrastructures can also benefit financially.

4.3 Performance Comparison of Machine Learning Methods to Estimate State of Charge (SOC)

4.3.1 Multicollinearity and Its Effect on SOC Estimation

Multicollinearity, or collinearity, is the existence of near-linear relationships among the independent variables in a multiple regression model. When there is perfect linear relationship, it creates a division by zero problem which causes the regression model to terminate. When there is a near-linear relationship though the regression is not terminated, it will cause distortion in the regression. Some of the effects that are caused by multicollinearity are: (i) inaccurate estimates of the regression coefficients, (ii) inflating the standard errors of the regression coefficients, (iii) deflating the partial t-tests for the regression coefficients, (iv) giving false, non-significant p-values and (v) degrading the predictability of the model.

To solve this problem some suggested solutions are: (i) collecting additional data, (ii) simplifying the model, (iii) removing observations that induce multicollinearity, (iv) selecting the variables carefully and (v) applying ridge regression or lasso regression.

Usually, the features that are used for SOC estimation purpose have near linear relationship and suffer from multicollinearity. To offset the effect of multicollinearity in SOC estimation, ridge and lasso regression has been applied here to examine the outcome.

4.3.2 Applied Methods

The methods that are applied in this project for battery state of charge estimation are: linear regression, ridge regression, lasso regression, support vector machine and artificial neural network. How these methods work are described in the following subsections [127-128].

4.3.2.1 Linear Regression

Let us assume that, we want to find a linear relationship between inputs $X_1, X_2, X, \ldots \ldots X_p$ and output y in the form of

$$Y = f(X) = \beta_0 + \sum_{j=1}^{p} X_j \beta_j \tag{4.21}$$

Given a set of training data (x_1, y_1), (x_2, y_2) , (x_3, y_3) . . . (x_N, y_N) from which to estimate the parameters β. Each $x_i = (x_{i1}, x_{i2}, \ldots, x_{ip})^T$ is a vector of feature measurements for the i-th case. The most popular estimation method is least squares, in which we pick the coefficients $\beta = (\beta_0, \beta_1, \ldots, \beta_p)^T$ to minimize the residual sum of squares:

$$\sum_{i=1}^{N} (y_i - f(x_i))^2 = \sum_{i=1}^{N} (y_i - \beta_0 - \sum_{j=1}^{p} x_{ij} \beta_j)^2 \tag{4.22}$$

Here the solution for β has a unique closed form solution. Assuming X is a full rank matrix we get:

$$\beta = (X^T X)^{-1} X^T y \tag{4.23}$$

4.3.2.2 Ridge Regression

Ridge regression is a type of regression that shrinks the regression coefficients by imposing a penalty on their size. The ridge coefficients minimize a penalized residual sum of squares:

$$\hat{\beta} = \underset{\beta}{\operatorname{argmin}}\{\sum_{i=1}^{N}(y_i - \beta_0 - \sum_{j=1}^{p} x_{ij}\,\beta_j)^2 + \lambda \sum_{j=1}^{p} \beta_j^2\} \tag{4.24}$$

Ridge regression is also called regularized linear regression. The parameter λ is called the regularization parameter.

4.3.2.3 Lasso Regression

The lasso is a shrinkage method like ridge, with subtle but important differences. Not only it can shrink the coefficients, but also can remove unnecessary variables by making the corresponding coefficients zero. The lasso estimate is defined by:

$$\hat{\beta} = \underset{\beta}{\operatorname{argmin}}\{\sum_{i=1}^{N}\left(y_i - \beta_0 - \sum_{j=1}^{p} x_{ij}\,\beta_j\right)^2 + \sum_{j=1}^{p} \lambda\,|\beta_j|\,\} \tag{4.25}$$

4.3.2.4 Support Vector Machine (SVM)

Let the training data consists of N pairs (x_1, y_1), (x_2, y_2) , (x_3, y_3) . . . (x_N, y_N), with $x_i \in \mathbb{R}^p$ and $y_i \in \{-1, 1\}$. Suppose that there is no overlapping between classes. Let us define a hyperplane by:

$$\{x : f(x) = x^T\beta + \beta_0 = 0\,\} \tag{4.26}$$

A classification rule induced by function f(x) can be stated as:

$$G(x) = sign(x^T\beta + \beta_0) \tag{4.27}$$

We can find such a hyperplane that creates the biggest margin between the training points for classes 1 and −1 found by using G(x). An optimization problem can be formulated that gives the solution for β for this hyperplane. It can be written as:

$$\max_{\beta,\beta_0} \frac{1}{||\beta||} \tag{4.28}$$

$$subject\ to\ y_i({x_i}^T\beta + \beta_0) \geq \frac{1}{||\beta||}, i = 1,2, \ldots \ldots .. N$$

Which can be rewritten as:

$$min\ ||\beta|| \tag{4.29}$$

$$subject\ to\ y_i({x_i}^T\beta + \beta_0) \geq 1, i = 1,2, \ldots \ldots .. N$$

The solution for this optimization problem provides the β for which the margin between the classes is the largest.

Now let us consider that the classes overlap. Then we define slack variables $\xi = \xi_1, \xi_1, \ldots, \xi_N$ such that $\sum_{i=1}^{N} \xi_1 \leq constant\ and\ \xi_i \geq 0, \forall i$. Then we can modify the constraint as:

$$y_i({x_i}^T\beta + \beta_0) \geq 1 - \xi_i \tag{4.30}$$

Now we can write the optimization problem as:

$$\min_{\beta,\beta_0} \frac{1}{2}||\beta||^2 + C\sum_{i=1}^{N} \xi_i \tag{4.31}$$

$$subject\ to\ \xi_i \geq 0, y_i({x_i}^T\beta + \beta_0) \geq 1 - \xi_i\ \forall i$$

The Lagrangian primal L_p and dual L_d can be written as:

$$L_p = \frac{1}{2}||\beta||^2 + C\sum_{i=1}^{N} \xi_i - \sum_{i=1}^{N} \alpha_i[y_i({x_i}^T\beta + \beta_0) - (1 - \xi_i)] - \sum_{i=1}^{N} \mu_i\xi_i \tag{4.32}$$

$$L_d = \sum_{i=1}^{N} \alpha_i - \frac{1}{2}\sum\nolimits_{i=1}^{N} \sum_{i'=1}^{N} \alpha_i\alpha_{i'}\, y_i y_{i'} x_i^T x_{i'} \tag{4.33}$$

Using the Karush-Kuhn-Tucker (KKT) conditions the solution is found to be:

$$\hat{\beta} = \sum_{i=1}^{N} \hat{\alpha}_i y_i x_i \tag{4.34}$$

where, $\hat{\alpha}_i$ are the nonzero coefficients for which the conditions are met.

4.3.2.5 Artificial Neural Network (ANN)

In machine learning, neurons are computational units that take $x_1, x_2, \ldots . x_n$ (and a +1 intercept term) as input, and outputs $h_{W,b}(x) = f(W^T x) = f(\sum_{i=1}^{n} W_i x_i + b)$ as shown in figure 4-7, where f is the activation function.

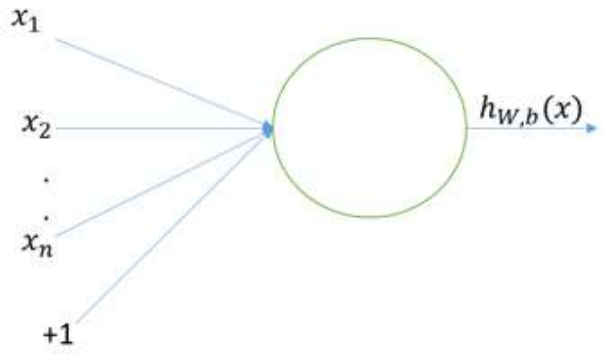

Figure 4-7 A computational neuron in a neural network

An artificial neural network is a collection of many neurons. Figure 4-8 shows the organization of a neural network. The circles labeled "+1" are called bias units and correspond to the intercept term. The leftmost layer of the network is called the input layer, the rightmost layer with only one node is the output layer and the middle layer is called the hidden layer. This neural network has 3 input units (not counting the bias unit), 3 hidden units, and 1 output unit.

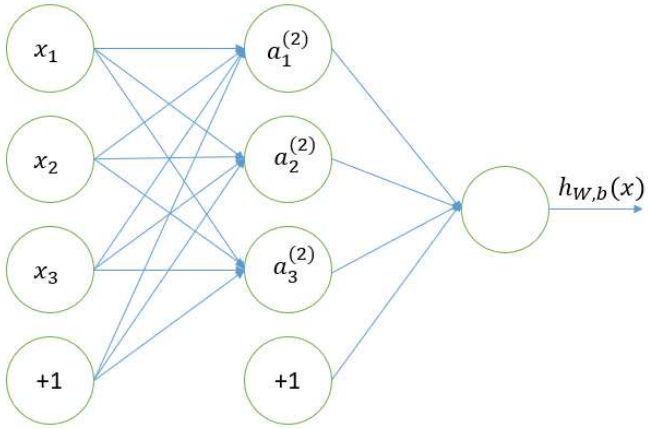

Figure 4-8 An artificial neural network structure

Let n_l denotes the number of layers in this network and s_l denote the number of nodes in layer l excluding the bias unit; thus n_l=3 in the example above. Layer l is labeled as L_1, so layer L_1 is the input layer, and layer L_{nl} is the output layer. The neural network has parameters (W,b) = $(W^{(1)}, b^{(1)}, W^{(2)}, b^{(2)} \ldots W^{(n_l)}, b^{(n_l)})$, where $W_{ij}^{(l)}$ denotes the parameter (or weight) associated with the connection from unit j in layer l to unit i in layer l +1, where $W^{(l)} \in \mathbb{R}^{s_{l+1} \times s_l}$. Also, $b_i^{(l)}$is the bias associated with unit i in layer l+1.

Let $a_i^{(l)}$ be the output of unit i in layer l. For input layer it can be written $a_i^{(1)} = x_i$. For the hidden layers and output layer the outputs are:

$$a_i^{(l+1)} = h_{W,b}(x) = f(\sum_{j=1}^{s_l} W_{ij}^{(l)} a_j^{(l)} + b_i^{(l)}) \tag{4.35}$$

To find the weights and the bias terms, first they are randomly assumed and then they are fed into the network to find the output. This is called the feedforward operation. The cost function can be defined as:

$$J(W,b;x,y) = \frac{1}{2}||h_{W,b}(x) - y||^2 \tag{4.36}$$

where, λ is the regularization parameter. Then we update the weights and bias terms using gradient descent method as:

$$W_{ij}^{(l)} = W_{ij}^{(l)} - \alpha \frac{\partial J(W,b)}{\partial W_{ij}^{(l)}} \tag{4.37}$$

$$b_i^{(l)} = b_i^{(l)} - \alpha \frac{\partial J(W,b)}{\partial b_i^{(l)}} \tag{4.38}$$

where, α is the learning rate of the gradient descent process. This part is called the backpropagation operation. Then using the updated weights and bias terms we do the feedforward operation and then backpropagation again and again until we converge to a reasonable solution.

4.3.3 Data and Features

The battery data are collected from CE-CERT's battery management system (BMS) database. The data is collected for 32 days and has a resolution of one minute. The readily available variables that are obtained from the BMS database are used as features to estimate the SOC and considered as conventional features here. They are: (i) charge rate, (ii) terminal voltage, (iii) open circuit voltage, (iv) current, (v) resistance, and (vi) mode of operation (Charging/Discharging/Idle/Disconnected). As suggested in [4] the nonconventional features are derived from using the data of the BMS database. These are: (i) current, (ii) terminal voltage, (iii) ampere hour, (iv) time average voltage (tav= $\frac{1}{T}\int_{t=0}^{T} v dt$), (v) twice time average voltage (ttav=$\frac{1}{T_2}\int_{T_1=0}^{T_2}(\frac{1}{T_1}\int_{t=0}^{T_1} v dt)dT_1$), (vi) time derivative of voltage (dvt=$\frac{dv}{dt}$), and (vii) second time derivative of voltage (ddvt=$\frac{d^2v}{dt^2}$). Then, both type of features are used separately for each of the machine learning algorithms to see

how they perform. The data is split into 60%, 20% and 20% portions to make training, validation, and test sets. Table 4-1 lists the battery specifications that are used in this work.

Table 4-1 BATTERY SPECIFICATIONS

Item	Specification
Type	Lithium Iron Phosphate with Yttrium (LiYFePO4)
Capacity	1000 Ah
Energy (kWh)	3.25 (11375 kWh lifetime)
Life cycle at 0.5 C discharge rate	17500 at 20% DOD | 7000 at 50% DOD | 3500 at 80% DOD
Discharge rate (continuous)	500 A
Nominal cell voltage	3.25 V per cell
Maximum cell voltage	4.0 V per cell
Minimum cell voltage	2.5 V per cell
Maximum discharge rate	1000 A (60 s)
Operating temperature	-20 °F to 150 °F
Charge/Discharge efficiency	96%
Self-discharge rate	1-2% per month
Max storage voltage	3.4 V at 82 °F
Shelf storage life	5 years at 60 % SOC

4.3.4 Results

The machine learning algorithms mentioned above are trained and validated with the training and validation data sets. After training and validation, the selected hypothesis functions are then applied to predict the test data. Figure 4-9 shows the prediction on test data when conventional features are used and figure 4-10 shows the same for the nonconventional features.

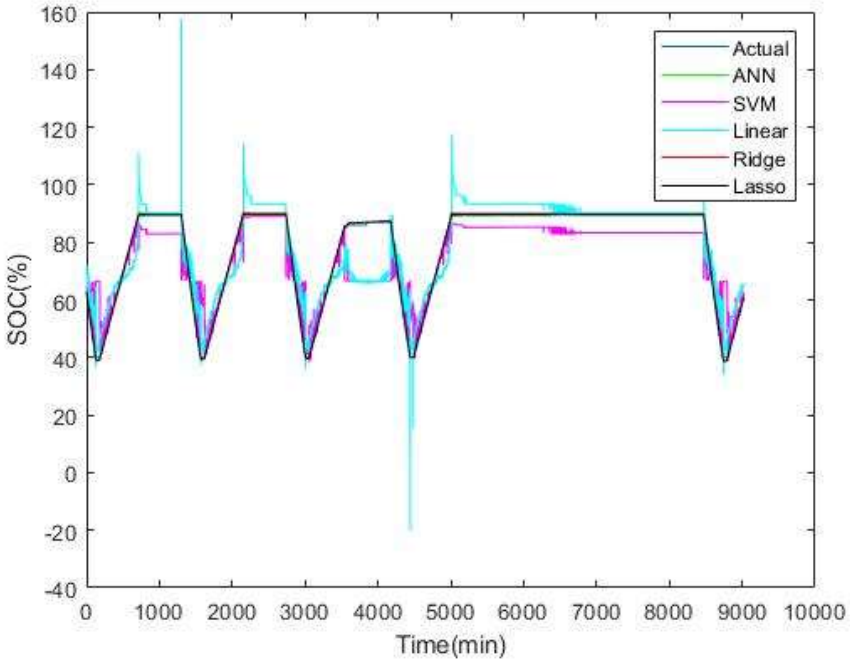

Figure 4-9 Estimated SOC for different methods using conventional features

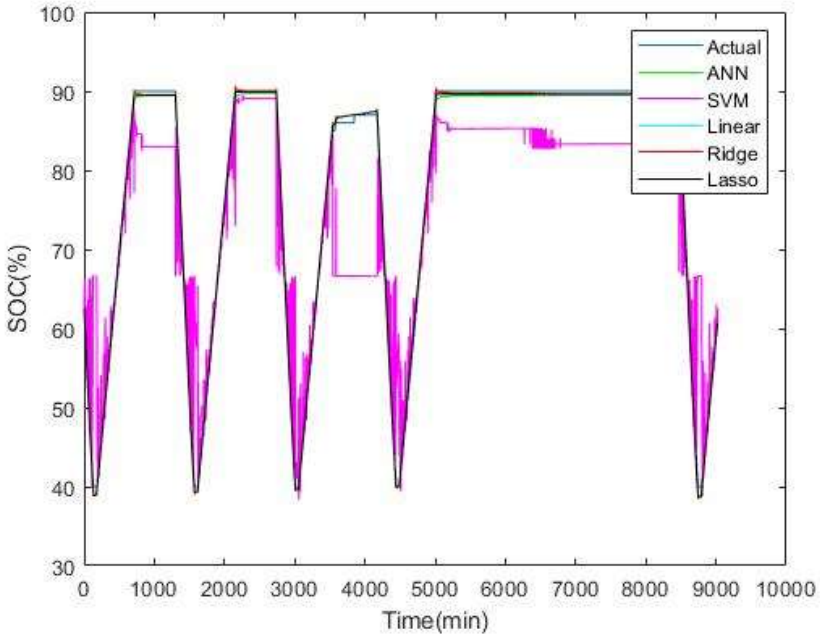

Figure 4-10 Estimated SOC for different methods using nonconventional features

While estimating SOC of battery accuracy is important but as it is desired to estimate the battery SOC in real time for practical application, time is also crucial. So, the best choice of machine learning method for SOC estimation must not only has to be accurate but also must be fast. For this reason, both accuracy and time is taken into account for performance comparison of these methods. To compare the accuracy, three error metrics have been chosen. They are mean absolute error (MAE), root mean square error (RMSE) and mean absolute percentage error (MAPE). Table 4-2 shows the performance comparison of the methods for both conventional and nonconventional features based on accuracy.

Table 4-2 PERFORMANCE COMPARISON TABLE-Accuracy

Feature	Conventional			Nonconventional		
Method	MAE	RMSE	MAPE (%)	MAE	RMSE	MAPE (%)
ANN	1.4506	2.2550	2.2011	0.4974	0.5648	0.6956
SVM	1.3917	2.2149	2.1601	5.7000	8.1399	7.8831
Linear	4.9729	7.2088	7.2880	0.3871	0.4738	0.5633
Ridge	4.9733	7.2098	7.2885	0.3871	0.4738	0.5634
Lasso	5.1468	7.4956	7.7093	0.4219	0.4932	0.6054

Table 4-3 shows the performance comparison of the methods for both conventional and nonconventional features based on time.

Table 4-3 PERFORMANCE COMPARISON TABLE- Time

Feature	Conventional	Nonconventional
Method	Time (s)	Time (s)
ANN	8.584929	1.026187
SVM	25.124698	206.024141
Linear	0.004201	0.004705
Ridge	0.003027	0.003441
Lasso	0.013549	0.010694

From the results we see that, in terms of accuracy using conventional features SVM produces the best result and using nonconventional features linear regression and ridge regression produce the best result. Ridge regression performs faster than the other methods in both cases and SVM is the slowest method in both cases. Except for SVM, nonconventional feature improves accuracy for all methods significantly. Non-conventional features make ANN and lasso regression perform faster, while making ridge regression and SVM perform slower. Though for ridge regression the difference is not much, and it still is the fastest method. But for SVM the difference is significant making it almost eight times slower. The reason behind the poor performance of the SVM taking a significantly higher time than other methods is due to the computational complexity of this method. For n training data samples the computational complexity is in the order of $O(n^2)$, leading to significant time increase. For methods other than ANN this complexity is in the order of $O(n)$. The complexity of ANN is mainly dependent on the number of layers and features, so it has a different order than other methods [129]. The possible reason behind the increased error of SVM using non-conventional method could be increased value of

hyperparameter C in equation (4.31) causing the model to overfit the training set leading to a good prediction on training set while poor results on the test set [130].

4.4 Conclusions

This chapter proposes and formulates a method for identifying bad cells by analyzing cell temperature rise rate and cell voltage data. Results are generated and validated applying the proposed method. The potentiality of economic benefits through this analysis is also discussed.

This chapter also analyzes the performances of different machine learning techniques using both conventional features that can be obtained readily and nonconventional features that can be derived using the conventional features. Since the speed of the calculation for SOC estimation is a crucial factor it has also been taken into account for performance evaluation. The results show that for all the cases except one, the applied machine learning algorithms achieve higher accuracy when nonconventional features are used. Nonconventional features also enhance the speed of these methods in most cases. Taking both accuracy and time into consideration, it can be concluded that ridge regression with nonconventional feature should be chosen for SOC estimation as it produces the best result among all scenarios.

5 Demonstration of Resiliency through Distributed Energy Resources in a Commercial Building Microgrid

5.1 Background and Motivation

While previous two chapters deal with the optimization and maintenance of commercial building microgrids with DERs, this chapter describes a real world demonstration of such microgrid operation in both islanded and grid connected settings.

As discussed in chapter 2, to make the grid more resilient in situations like rotating blackouts or PSPS events, significant grid infrastructure upgrade is needed which may require significant amount of time and resources. Also, there may be a lot redundant resources. While microgrids and DERs can increase the grid resiliency without such large scale upgradation. When the grid power is disrupted or unavailable, an islanded microgrid with DERs can sustaining itself through the period and is able to continue the essential operations without any interruption. As EVs are becoming more prevalent and is expected to dominate the transportation sector, enabling them as a DER asset through V2G and deploying them to sustain islanded microgrids presents great potential for increased grid resiliency.

This chapter shows the demonstration of V2G operation within an islanded microgrid with its own renewable solar generation, battery energy storage and different types of loads. This demonstration proves the ability of V2G operation to sustain a

microgrid which is islanded from the utility grid and shows the interaction of different components of the microgrid.

5.2 Experimental Setup

The Microgrid considered here is a commercial building with its own renewable generation and energy storage. It is situated at the University of California, Riverside's (UCR) research facility called College of Engineering - Center for Environmental Research and Technology (CE-CERT). The building area is about 20,000 square feet and is one storied. This building is used for housing the offices of the administrative staffs and researchers of CE-CERT and is referred as Admin building. The details of the microgrid system configuration along with two other building integrated microgrids are discussed in [131]. The different components of the microgrid associated with this demonstration are shown in figure 5-1 and discussed below in the following subsections.

Figure 5-1 Different components of the microgrid

5.2.1 Solar Photovoltaic (PV) Generation

CE-CERT has 500kW parking lot structure solar photovoltaic (PV) system array for the entire facility and a dedicated 180 kW inverter serves the mentioned building microgrid. The inverter can be controlled remotely to perform solar generation curtailment.

5.2.2 Battery Energy Storage System (BESS)

The battery energy storage system (BESS) is composed of 143 cells with a total 500 kWh storage capacity connected to a 100 kW bidirectional inverter. This battery energy storage (BES) inverter is capable of both working with a grid (Grid Mode) or an islanded microgrid (Critical Load Mode). In grid mode, it can be controlled to send power to or receive power from the grid when a power value and power factor value command is set in the inverter. In critical load mode, it can be used to form a microgrid by working as a load following inverter where it senses the load requirement and delivers power accordingly. The whole setup is inside a mobile trailer so it can be moved anywhere and can be connected where there is an appropriate plug point inlet.

5.2.3 Vehicle to Grid (V2G) Inverter and Electric Vehicles (EV)

The vehicle to grid (V2G) inverter is a bidirectional 30 kW inverter that can charge or discharge an EV. It does not have the load following capability like the BES inverter. There are two 2013 Nissan Leafs that are available for use in the microgrid experiment. Each of the EVs have nominal battery energy storage capacity of 24 kWh.

5.2.4 Load Bank

The load bank is a three-phase adjustable resistive load that can be set to value up to 100 kW in 1 kW steps.

5.2.5 Microgrid Connections

All components mentioned in the above subsections and the building loads are connected to a 480V, 3-phase electrical busbar inside the building's electrical room through breakers and switches. The busbar itself is connected to the grid through a utility meter and two main breakers. One of the breakers is outside of the building and the other one is inside the electrical room. Three transformers are connected to the busbar that serve the loads in the building. Transformer T1 serves 16 Heating, Ventilation and Air-Conditioning (HVAC) units. Transformer T2 serves the plug loads, four level two EV chargers outside the building and some of the lighting loads. A small transformer serves most of the lighting loads in the building. The PV inverter is also connected to the busbar. A junction box outside the building is connected to the busbar through a breaker. The other components can be connected to the busbar using the junction box. The junction box connection also serves a level 3 DC Fast Charger (DCFC), which is not used in this experiment. Figure 5-2 below shows the one line connection diagram of the microgrid experiment. Meter M1 is the utility meters and meters M2 to M5 were connected for data collection of the experiment.

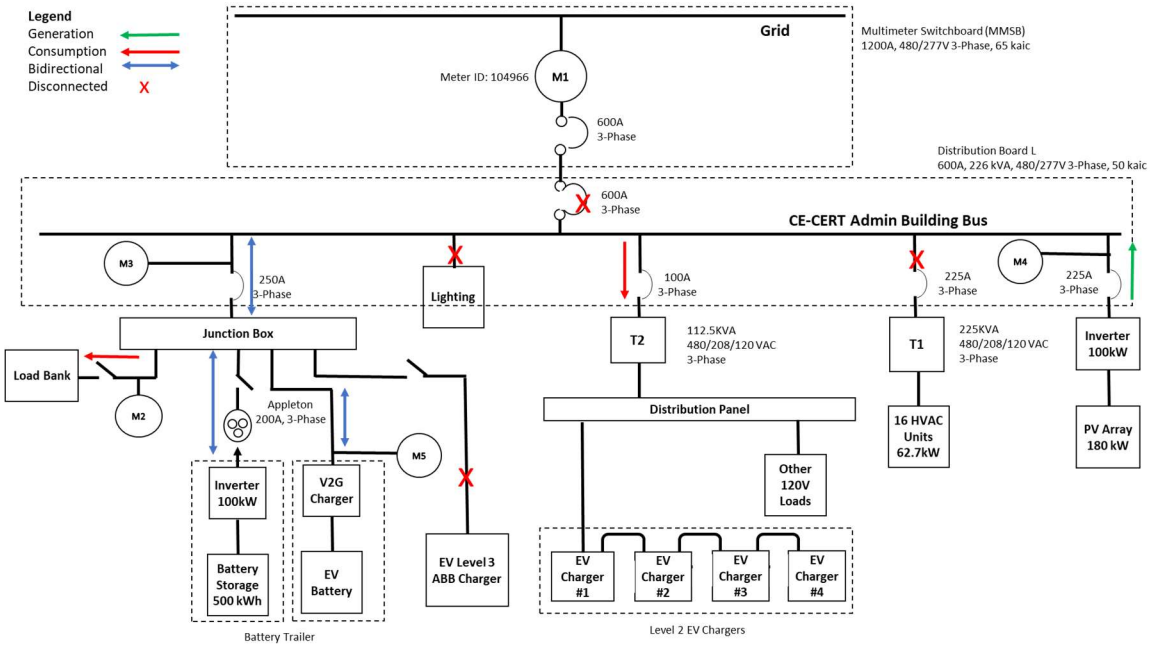

Figure 5-2 One Line Connection Diagram of the Microgrid System with Power Flow Direction

5.3 Experiment Design and Methodology

To obtain the desired results from the experiment different operations need to be executed in a specific manner considering the capabilities and limitations of the DERs. For example, the solar kW capacity is much larger than the building load since this building is a net-zero energy building exporting surplus solar power to the grid to be imported back at night. But the critical load port of the BES inverter which delivers the power to the microgrid in grid-forming mode allows up to 5 kW power to charge the batteries. The remaining solar power after serving the building load and charging the BESS in islanded operation has no grid to absorb this surplus power. Therefore, the system frequency increases and the PV inverter trips when it goes above the upper limit of the allowable

frequency value. Similarly, SOC of the energy storages are another constraint that limits the duration of operation. The experiment was designed in way that complies to the limitations and requirements of the system. The tasks were divided among four phases. At first phase, we execute the preparations needed to carry out the experiment. Then in second phase, we disconnect the main breaker making the microgrid islanded and keep running the island with the help of two of the DERs, PV and BESS. Then in third phase, we bring in the EV and test both charging and discharging of EV, acting as load and DER, in the microgrid, respectively. Then in the final phase, we collect the data and analyze them to obtain and present the results. Figure 5-3 shows the steps of the experiment design for each of the phases.

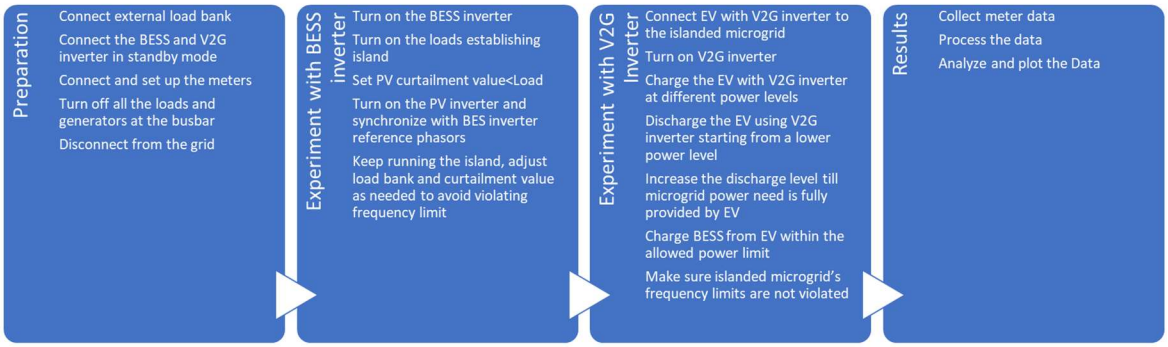

Figure 5-3 Tasks at Different Phases of the Experiment

We perform many of the steps in the experiment based on several conditions that emerge from the system constraints. We develop a flowchart of the experiment that

represents them and generates a set of instructions to carry out the experiment. Figure 5-4 illustrates the flowchart of the experiment steps.

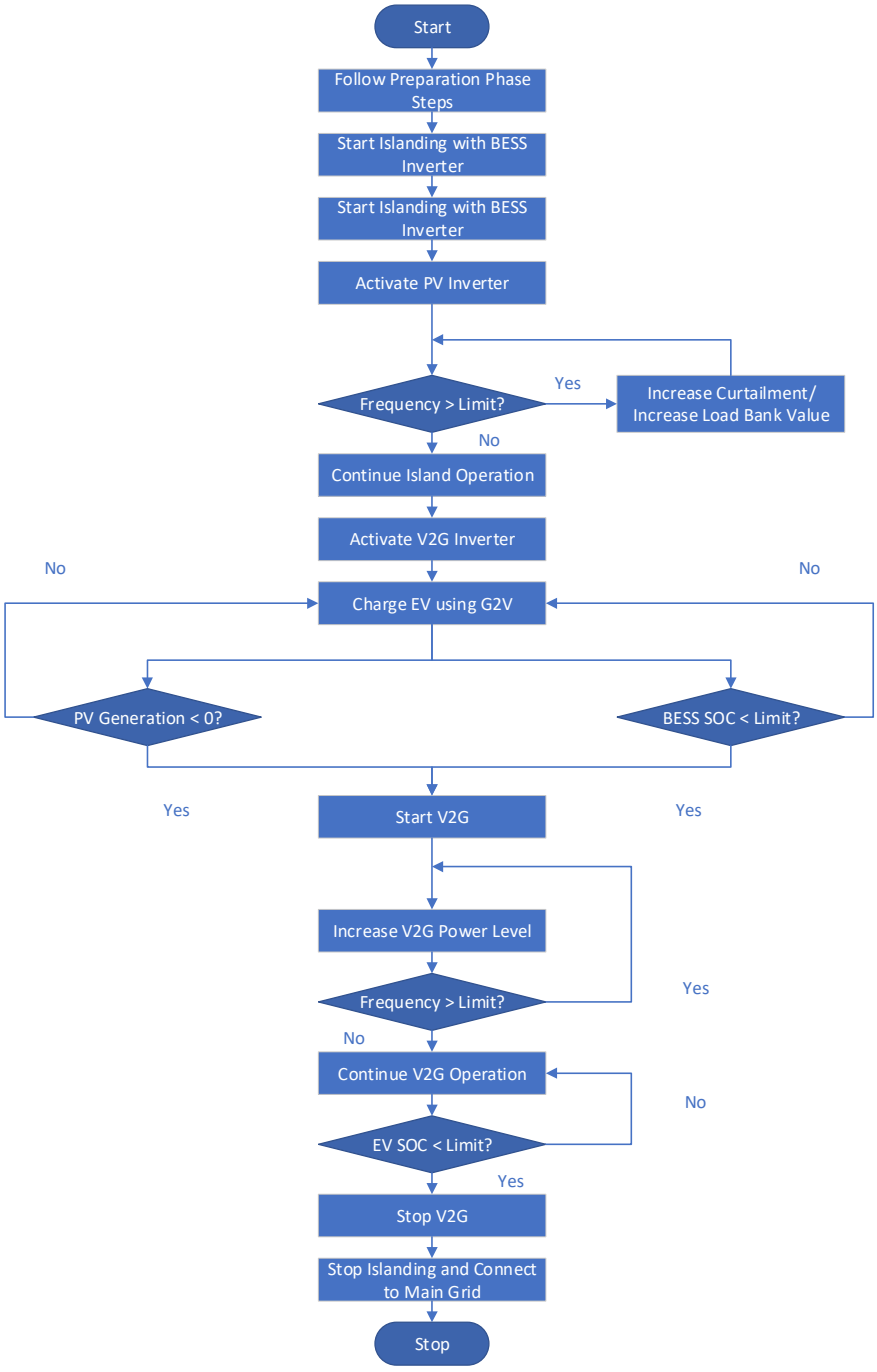

Figure 5-4 Flowchart of the Experiment Steps

This flowchart acts a guideline for conducting the tasks in a systematic manner and helps the experiment to be successful without any complications.

5.4 Results

Power plots of the experiment are shown in figures 5-5 and 5-6 with the sequences of important actions and events labeled accordingly. The results are discussed in detail with the steps of the experiment.

5.4.1 Preliminary Testing with the Grid

To confirm proper functioning of BES and V2G inverters, preliminary testing were performed initially with grid. Transformers T1, T2 and lighting were turned off to eliminate load variations during this part of the experiment. A controllable three-phase load bank was connected to achieve loading as needed. With this reduced loading condition, PV curtailment was set at a lower value, producing about 17 kW. At first the BES inverter was charged from the grid, kept idle and discharged to the grid, respectively, with 5-minute duration each. Same testing was repeated for the V2G inverter operation. Then at 12:42, the testing was done for both the inverters with one charging and the other discharging, keeping both idle and then alternating the charging and discharging of the inverters, for 5-minute duration each. This last experiment demonstrated that BES and vehicle batteries can exchange energy with each other without increasing the loading on the grid distribution feeder. This type of system configuration can help solve the distribution line limitations faced by many potential charging sites for rapid charging of medium duty and heavy duty (MDHD) EVs. These actions are shown in the pink labeled portion of figure 5-5.

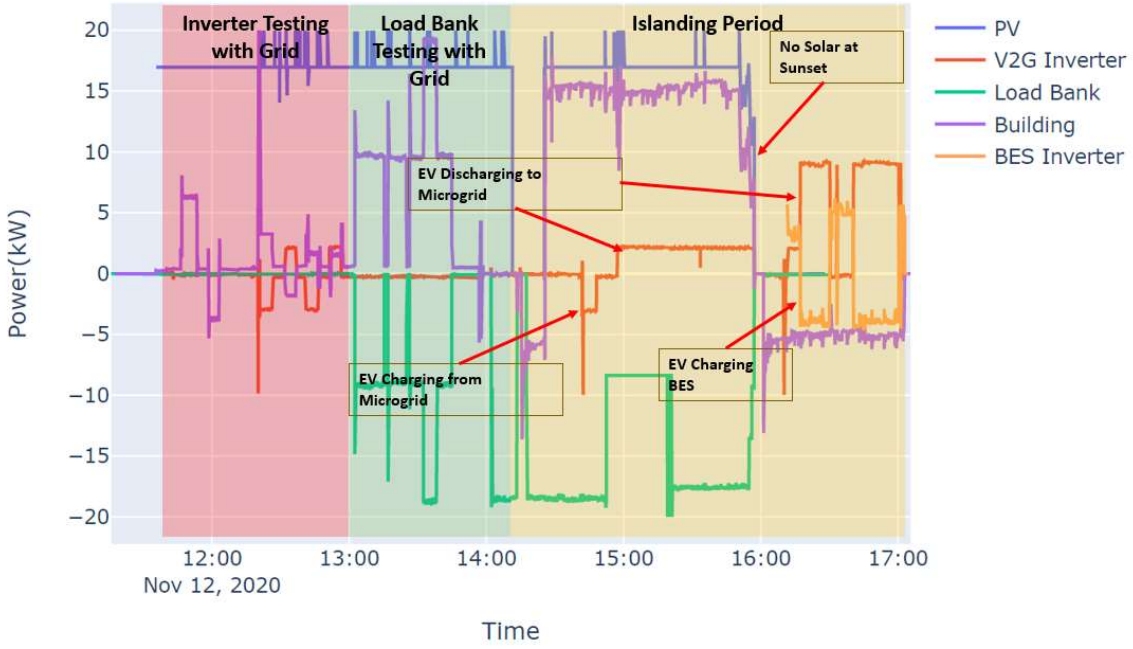

Figure 5-5 Power plots for the System including V2G, BES, PV, Building Load and Islanding

5.4.2 Solar Inverter and Load Bank Testing with the Grid

The second shaded portion in figure 5-3 shows curtailed solar production along with various settings of the load bank. This was needed to accommodate typical fixed power production of PV inverters potentially creating surplus power causing severe frequency variation in islanded operation. For a system with large inertia, the effect on the variation of frequency is small due to a single generation source or some load variations. But in islanded microgrids this could pose a serious problem as it could violate the operational limits and cause failure of islanded operation. The load balancing and over-generation curtailment example shown here can help solve the frequency variation problems of islanded microgrids.

5.4.3 Microgrid Islanding

As shown in the yellow shaded potion in figure 5-5, at 14:11, the PV inverter was shut off and the main grid breaker was disconnected. Then at 14:15 the plug load transformer T2 was turned on, establishing the islanded microgrid, as T2 load was supplied by the BES inverter. At 14:17, the load bank was set at 20 kW, in addition to the T2 load. At 14:20, the PV inverter was turned on again. After 5 minutes it synchronized with the phasor from BES inverter and started supplying power to the islanded microgrid. Such islanded microgrids can power the critical loads without interrupting operation during rotating blackouts or PSPS events with the help of DERs with one of the inverters working as primary source providing necessary reference phasors.

5.4.4 V2G Operation

As shown in figure 5-5, at 14:42, the V2G inverter was activated with charging value set at 2.5 kW, charging the EV from the islanded microgrid. After a few minutes, the V2G inverter was set at idle mode before switching to discharge mode with a set value of 2.5 kW. The delivered EV power is now partly helping to carry the islanded microgrid load along with power delivered by BES and PV inverters. The solar generation started to reduce later in the day requiring load bank set values to be adjusted accordingly thereby avoiding mismatch of power between generation and demand. Both PV and load bank were inactive after 15:57. The V2G activities beyond 16:11 are presented in detail in figure 5-6.

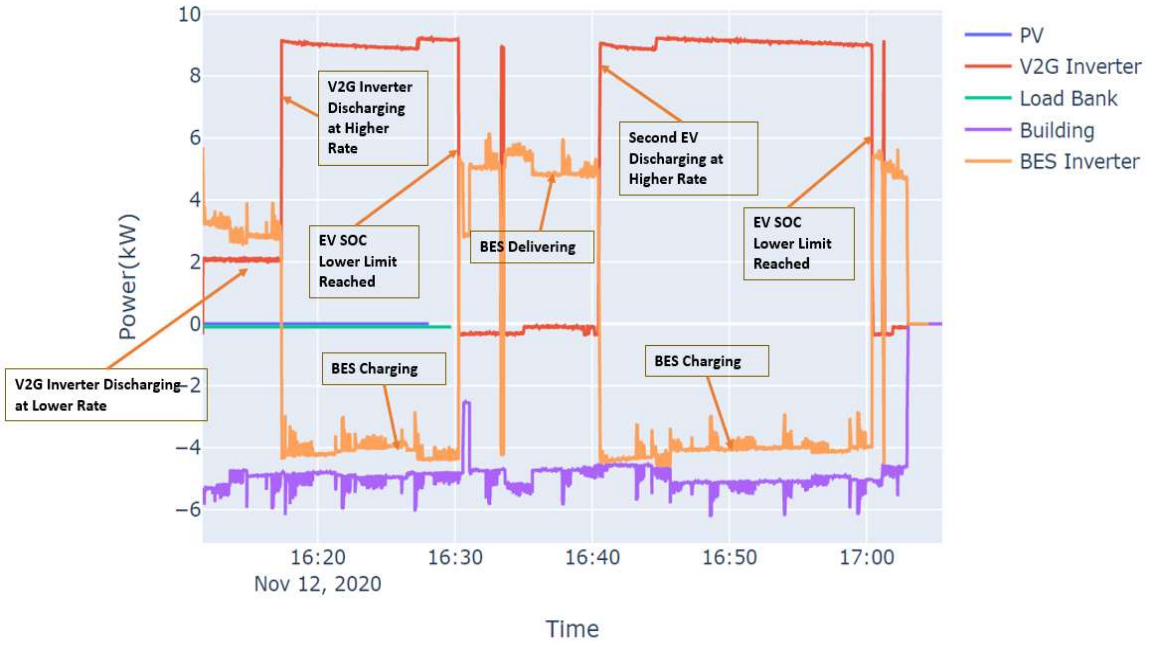

Figure 5-6 V2G operation with Vehicle Sustaining Islanded Microgrid with Load and Battery Charging

To evaluate the V2G inverter's ability to support the islanded microgrid load alone, the discharge rate was increased to a value of 10 kW. As typical T2 load was about 5 kW, the power supplied by the vehicle through V2G was more than the required load at that time. The remaining power was flowing through the BES inverter to the storage batteries. The charging of batteries continued till low SOC limit for the V2G inverter was reached. Next a second EV was plugged with the same 10 kW discharge command, allowing it to carry the load and charge the BES batteries again. Meanwhile, the building load was automatically carried by the BES inverter. The second EV's V2G operation continued till it reached its low SOC limit.

This V2G operation demonstrates the potential of EVs as DER assets in islanded microgrid systems. Not only it supported the islanded microgrid at lower discharging rate, but also it exhibited the ability to exchange power with the BESS at higher discharging rate by charging the BESS. This ability offers more flexibility in DER operation of microgrids and can contribute to improved resiliency.

5.5 Validation

To validate resiliency of the islanded microgrid, we use some of the electric power distribution reliability indices suggested by IEEE [132]. The indices considered are:

(i) System Average Interruption Duration Index (SAIDI), and (ii) Customer Average Interruption Duration Index (CAIDI).

These indices can be represented as:

$$SAIDI = \frac{\sum_i r_i N_i}{N_T} \tag{5.1}$$

$$CAIDI = \frac{\sum_i r_i N_i}{\sum_i N_i} \tag{5.2}$$

Where,

N_i= Number of interrupted customers for each sustained interruption event during the reporting period.

N_T= Total number of customers served for the area.

r_i= Restoration time for each interruption event

SAIDI indicates the total duration of interruption for an average customer within some specific period. CAIDI expresses the average time required for restoration of power.

Another important related concept is the Major Event Day (MED). Major Events occurs when the electric power system exceeds its reasonable design and operation limits. MEDs are those days when the system SAIDI exceeds some threshold value T_{MED}. This threshold value is determined from the statistical analysis of the historical SAIDI values of a certain period, usually last five years.

For our analysis SAIDI and CAIDI values for latest reported ten years (2010-2019) were collected from three major utility companies in California, namely Southern California Edison (SCE), San Diego Gas and Electric (SDG&E) and Pacific Gas and Electric (PG&E) [133-135]. Tables 5-1 and 5-2 show the SAIDI and CAIDI values of these utilities including and excluding the MEDs for the most recent reported ten years, respectively.

Table 5-1 SAIDI for Last Reported 10 Years

Year	Including MED			Excluding MED		
	SCE	PG&E	SDG&E	SCE	PG&E	SDG&E
2010	140.91	250.4	85.37	98.69	130.3	63.36
2011	232.39	279.5	567.59	108.15	109.6	53.43
2012	108.13	141.1	64.36	100.7	110.7	64.36
2013	102.61	117	75.03	94.48	95.8	59.96
2014	112.1	131.9	75.81	92.3	91	64.6
2015	114.83	131.8	58.11	100.15	80.7	57.92
2016	134.48	106.8	86.01	109.98	93.9	72.75
2017	139.73	357.9	117.49	91.72	97.4	64.51
2018	136.82	282.9	121.02	71.25	99.9	77.76
2019	177.97	1365.1	122.96	90.75	117.7	68.64

Table 5-2 CAIDI for Last Reported 10 Years

Year	Including MED			Excluding MED		
	SCE	PG&E	SDG&E	SCE	PG&E	SDG&E
2010	134.56	179.6	130.99	120.99	117.8	121.8
2011	223.75	219.1	385.63	118.3	112.5	113.44
2012	121.1	124.9	120.78	117.76	106.8	120.78
2013	112.76	109.3	133.84	107.85	98.9	127.03
2014	116.04	126.2	119.88	106.82	103.5	107.06
2015	125.4	136.3	109.68	116.56	102.5	110.09
2016	122.26	104.5	126.99	110.69	99.8	117.43
2017	117.19	244	200.87	105.4	110.9	125.92
2018	156.61	267.9	183.88	99.58	103.8	123.84
2019	171.17	728.5	192.38	104.75	116.5	115.23

An analysis was done to show the effect of the BESS and V2G operation based on the resiliency indices of the collected data. The analysis includes a total of 8 scenarios where it is assessed what would be the resource required to sustain the microgrid in each scenario. In each scenario either the maximum or the average SAIDI or CAIDI is used to evaluate the amount of resource needed to withstand the interruption. Results show three cases: if only BESS is present, if only EV is present and if both are present. The hourly load of the building microgrid for the year 2019 was collected and used. For the first four scenarios the average SAIDI and CAIDI values were used with the average building load

for the whole year. For the next four scenarios the maximum SAIDI and CAIDI values were used along with the maximum monthly average load value. The first four scenarios show assessment for a typical interruption condition while the rest show them for the worst cases. Table 5-3 presents the results of the analysis. For the BESS we assumed that the usable range is from 20% to 90% of the total storage capacity and for the EVs we assumed that the usable range of the battery capacity is from 20% to 100% of the total storage capacity. Another assumption is made that when both the BESS and the EVs are used, the EVs deliver energy only after the total usable capacity of the BESS has been utilized.

Table 5-3 Results from the Analyzed Scenarios

Scenario	Index	Index Value (min)	Load (kW)	BESS Usable Capacity (kWh)	EV Capacity (kWh)	Resource Needed to Sustain Microgrid		
						Only BESS Capacity (%)	Only EV (Count)	Both EV and BESS
1	Avg SAIDI including MED	197.94	28.57	350	19.2	26.9	5	BESS 26.9%, 0 EVs
2	Avg SAIDI excluding MED	87.75	28.57	350	19.2	11.9	3	BESS 11.9%, 0 EVs
3	Avg CAIDI including MED	178.20	28.57	350	19.2	24.2	5	BESS 24.2%, 0 EVs
4	Avg CAIDI excluding MED	112.14	28.57	350	19.2	15.3	3	BESS 15.3%, 0 EVs
5	Max SAIDI including MED	1365.1	39.21	350	19.2	254.9	47	BESS 100%, 29 EVs
6	Max SAIDI excluding MED	130.3	39.21	350	19.2	24.3	5	BESS 24.3%, 0 EVs
7	Max CAIDI including MED	728.5	39.21	350	19.2	136.0	25	BESS 100%, 7 EVs
8	Max CAIDI excluding MED	127.03	39.21	350	19.2	23.7	5	BESS 23.7%, 0 EVs

Results show that the microgrid considered here would be able to survive most of the outage scenarios presented here. The results of the analysis as summarized in table 5-3 showed that out of the 8 scenarios it would be able to sustain operation in 6 of them, supported by the BESS or EV only. The other two cases are the worst-case scenarios, where the SAIDI and CAIDI values are almost 7 times and 8 times of their average counterparts ,respectively, and are extremely rare cases. From these results it is evident that this microgrid setup is able to deal with the regular outages seen in California. The extreme outages that happen rarely can also be managed with upgradation of the system. The number of EVs required to sustain the microgrid solely using V2G in the regular outage scenarios are also limited up to 5 EVs which is very much feasible considering current EV penetration rate and widespread deployment of chargers with V2G provision.

To find the impact of both renewable energy and energy storage, a resiliency simulation of the microgrid under consideration was executed using National Renewable Energy Laboratory's Reopt [106]. Fifty precent of the total load was assumed as the critical load of the system and the maximum SAIDI from table III value was considered as the outage duration. The optimal BESS size for the base case, financially most feasible case and case considering resiliency was determined considering the existing load and solar PV system. The optimal storage size for the resiliency was 35 kW/217 kWh system. The existing BESS is sufficient for such a system. Though 10 more EVs are required with V2G inverter upgraded to 35 kW if the microgrid is solely dependent on the V2G operation. A total of 8,760 outage simulations are run, one for each hour of the year. The average and maximum resiliency are calculated as the average and maximum time survived during the

simulated outages. The hourly microgrid load for year 2019 was used here. The outage start date is assumed as the day when the highest peak load happens (May 5). Table 5-4 shows the results of comparison among the three cases. Figure 5-5 displays the zoomed in version of the microgrid operation focusing on the outage hours. Optimal resource allocation of solar PV and BESS during the outage duration that would result in the most cost-effective outcome is shown in this figure. On May 5, before the outage started most of the load was served by PV while the remaining portion was from the grid. A small amount was delivered to the BESS. The microgrid starts operating as an island when the outage starts. To compensate for the lost grid power, the battery starts providing power to the load as shown in blue shaded area in figure 5-7. BESS SOC starts dropping until next day's solar production is large enough to supply both load and BESS. This optimized operation shows that even with lower rated DERs the microgrid island can be sustained for the most extreme scenario of the analyzed eight scenarios when we run only the critical loads instead of all the loads run at usual times.

Table 5-4 Results from the Simulation

Scenario	Business as Usual	Financial	Resilience
PV Size (kW)	100	100	100
BESS Size	-	-	35 kW/ 217 kWh
Life Cycle Cost ($)	108,562	108,619	176,963
Average Resiliency (hrs)	2	2	220
Maximum Resiliency (hrs)	12	12	1,125

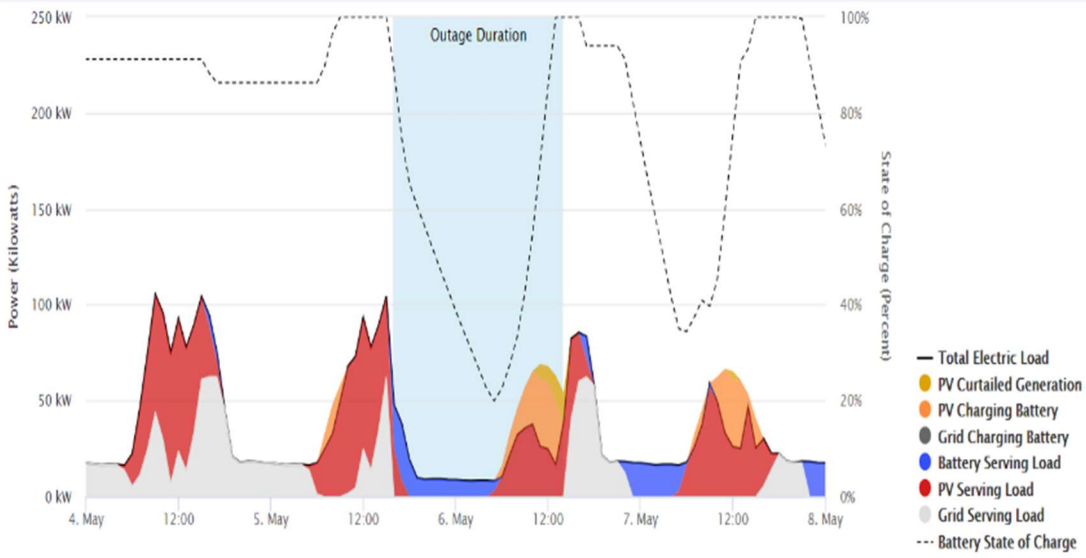

Figure 5-7 System Performance During Outage

5.6 Conclusions

This chapter describes a successful implementation and demonstration of an islanded microgrid for an office building with EV delivering power to support microgrid

operation. An islanded microgrid was formed using, a stationary battery energy storage inverter, solar PV inverter and building loads. Both charging and discharging of EV energy into the islanded microgrid was demonstrated. It showed that not only an EV can be charged from a microgrid that is not connected to the main grid, but also it can be used to help a microgrid receive energy complementing other available generation sources. With the help of a load following inverter providing necessary reference phasors for establishing this islanded microgrid, more inverters can be brought in parallel with it to sustain an islanded microgrid for a longer duration. The island sustained for 2 hours 45 minutes, which is longer than the recent rotating blackout durations of August 2020 and could have stayed active for longer time using the full storage capacity of BESS. This can also improve resiliency and reliability by providing power during PSPS incidents. An analysis validating the effectiveness of the microgrid in such outage conditions are also presented. The EVs used here were 2013 Nissan Leafs subject to storage capacity degradation and reduced limits on rate and duration of delivered battery energy. With newer vehicle models, higher discharge power value and duration can be obtained. Medium duty and heavy duty (MDHD) EV's can help us to achieve that to higher extent. Results of this demonstration showed that one EV with enough storage capacity and a properly sized inverter can sustain a residential microgrid by itself, while multiple EV's can do that for a commercial building sized microgrid. Standard PV and V2G inverters deliver set values of power and are not able to respond to continuous changing building load.

6 Conclusions and Future Works

6.1 Conclusions

In this dissertation, several methods have been developed, and experiments were conducted that can improve the cost-effectiveness, reliability, and resiliency of commercial building microgrids. The specific and novel outcomes of this study are summarized below:

- A novel comprehensive optimization framework was developed that is applicable to a commercial building microgrid equipped with renewable generation and BESS under any type of commercial utility tariff. These tariffs contain diverse energy and demand charge components such as, time independent peak demand, TOU, CPP, etc, that are analyzed to develop a universal cost function for the optimization. Through the optimization of building loads savings potential from different tariff types are compared to obtain best investment decision for the consumers. These comparisons revealed that differences in tariff types and charge components can have a huge impact on the monthly billing and optimization results. Different changes in tariffs, such as, changes in prices, time periods and options are taken into account and their impacts on the optimization results are examined. The findings reveal which price components have higher or lower impact on the savings from different DERs and how choice between energy and demand heavy charges impact the percentage savings from different DERs for buildings with different load factors. Benefits of this optimization from utility's perspective are also

presented through demand reduction possibilities and a dynamic tariff was proposed that showed it can alleviate “Duck Curve” ramp rate requirements.

- A data-driven predictive maintenance method for BESS was developed using easily accessible data. The method was found to be effective in detecting faulty BESS cells. Potential financial gains from this method were discussed. The best machine learning based BESS SOC estimation method in terms of accuracy and time was sought through comparison of different machine learning methods with the best selection of features. The Ridge Regression method was identified as the best method for SOC estimation in terms of both aspects.
- A microgrid islanding methodology was developed and implemented in a commercial building microgrid. This implementation included combination and coordination of several DERs such as BESS, PV and EVs with V2G. Resiliency of the microgrid was examined under several constrains, such as, operational limits of system frequency and SOC of both BESS and EV battery storages. A number of resiliency indices of different outage scenarios were utilized to validate the results. The results and validation revealed that the mentioned microgrid would have been able to withstand even the worst outage in California that occurred during these last ten years and all the other outages could have been easily handled just by using the partial capacity of the of the microgrid through following developed strategy properly.

6.2 Selected Publications from This Research

- A. Hasan, J. Yusuf, L. Contreas, and S. Ula, “Bad Cell Identification of Utility-Scale Battery Energy Storage System through Statistical Analysis of Electrical and Thermal Properties”, IEEE PES Innovative Smart Grid Technologies Europe, (ISGT Europe), 2021 (received best paper award).
- A. Hasan, L. Contreas, J. Yusuf, and S. Ula, “A Comprehensive Building Load Optimization Method from Utility Rate Structure Perspective with Renewables and Energy Storage”, International Conference on Smart Energy Systems and Technologies (SEST), 2021.
- A. Hasan, J. Yusuf, L. Contreas, M. Barth and S. Ula, "Demonstration of Microgrid Resiliency with Vehicle to Grid (V2G)," IEEE Transportation Electrification Conference and Expo (ITEC), 2021.
- A. Hasan, J. Yusuf and S. Ula, "Nonconvex Thermal Modelling and Energy Optimization for Multizone Commercial Buildings with VAV Type HVAC Units," International Conference on Smart Grids and Energy Systems (SGES), 2020.
- A. Hasan, J. Yusuf and R. B. Faruque, "Performance Comparison of Machine Learning Methods with Distinct Features to Estimate Battery SOC," IEEE Green Energy and Smart Systems Conference (IGESSC), 2019.

6.3 Future Works

There are several outcomes derived from this dissertation that contributes toward the improvement of commercial building microgrids with DERs, however, further

improvements may be possible by extending this research into the future. Some of the possible future works that can done to bring these improvements are listed below:

- The optimization in chapter 3 uses building load and solar generation data assumed perfect prediction. However, forecasted values may have some inaccuracies which can introduce some discrepancy in the optimization results. Future work can be carried out to see how the level of inaccuracy associate with the level of discrepancy in the optimization results. Increasing EV adoption and on-site EV charging infrastructures in workplaces along with V2G capabilities have significant impact on commercial building loads. Sometimes these EV charging is metered individually or aggregated under the main meter. Separately metered EV charging fall under separate EV tariffs. Further works can be done considering these aspects. Effects of load deferral under different demand response schemes and prospects of other grid ancillary services besides flexible ramping can also be investigated.
- The work in section 4.2 can be further expanded by adding other factors to the analysis such as cell aging and chemical properties from spectroscopy data, if available. The application of different machine learning techniques with performance comparison can further improve this work.
- The microgrid with V2Gs are typically relatively small size. Future development work is needed to involve integrating and combining DERs of various capacities for larger V2G impact in microgrids, thereby potentially maximizing the benefits from grid ancillary services.

Bibliography

[1] U.S. Department of Energy—Energy Information Administration. International Energy Outlook 2019.

[2] IPCC (2014). Climate Change 2014: Mitigation of Climate Change. Contribution of Working Group III to the Fifth Assessment Report of the Intergovernmental Panel on Climate Change [Edenhofer, O., R. Pichs-Madruga, Y. Sokona, E. Farahani, S. Kadner, K. Seyboth, A. Adler, I. Baum, S. Brunner, P. Eickemeier, B. Kriemann, J. Savolainen, S. Schlömer, C. von Stechow, T. Zwickel and J.C. Minx (eds.)]. Cambridge University Press, Cambridge, United Kingdom and New York, NY, USA

[3] 2020. Renewables 2020: Analysis and forecast to 2025. International Energy Agency.

[4] "Frequently asked questions (faqs) - U.S. energy information administration (EIA)," Frequently Asked Questions (FAQs) - U.S. Energy Information Administration (EIA). [Online]. Available: https://www.eia.gov/tools/faqs/faq.php?id=92&t=1. [Accessed: 09-Apr-2022].

[5] U.S. Department of Energy—Energy Information Administration. Quadrennial Technology Review 2015: AN ASSESSMENT OF ENERGY TECHNOLOGIES AND RESEARCH OPPORTUNITIES. 2015.

[6] "Accomplishments," Energy.gov. [Online]. Available: https://www.energy.gov/eere/better-buildings-neighborhood-program/accomplishments#:~:text=Saved%20consumers%20%24730%20million%20in,million%20worth%20of%20energy%20upgrades. [Accessed: 09-Apr-2022].

[7] Confronting the duck curve: How to address over-generation of Solar Energy," Energy.gov. [Online]. Available: https://www.energy.gov/eere/articles/confronting-duck-curve-how-address-over-generation-solar-energy. [Accessed: 29-Jan-2022].

[8] U.S. Department of Energy—Energy Information Administration. Annual Energy Outlook 2020.

[9] "About the Commercial Buildings Integration Program," Energy.gov. [Online]. Available: https://www.energy.gov/eere/buildings/about-commercial-buildings-integration-program. [Accessed: 08-Apr-2022].

[10] U.S. Department of Energy, "Using distributed energy resources," Distributed Generation & Alternative Energy Journal, pp. 37–66, 2002.

[11] D. T. Ton and M. A. Smith, “The U.S. Department of Energy's microgrid initiative,” The Electricity Journal, vol. 25, no. 8, pp. 84–94, 2012.

[12] K. Mongird, V. V. Viswanathan, P. J. Balducci, M. J. Alam, V. Fotedar, V. S. Koritarov, and B. Hadjerioua, “Energy Storage Technology and Cost Characterization Report,” 2019.

[13] M. Moghimi, R. Garmabdari, S. Stegen, and J. Lu, “Battery energy storage cost and capacity optimization for University Research Center,” 2018 IEEE/IAS 54th Industrial and Commercial Power Systems Technical Conference (I&CPS), 2018.

[14] M. Razmara, G. R. Bharati, M. Shahbakhti, S. Paudyal and R. D. Robinett, "Bilevel Optimization Framework for Smart Building-to-Grid Systems," in IEEE Transactions on Smart Grid, vol. 9, no. 2, pp. 582-593, March 2018.

[15] L. Yu, D. Xie, C. Huang, T. Jiang, and Y. Zou, “Energy optimization of HVAC systems in commercial buildings considering indoor air quality management,” IEEE Transactions on Smart Grid, vol. 10, no. 5, pp. 5103–5113, 2019.

[16] F. Wang, L. Zhou, H. Ren, X. Liu, S. Talari, M. Shafie-khah, and J. P. Catalao, “Multi-objective optimization model of source–load–storage synergetic dispatch for a building energy management system based on tou price demand response,” IEEE Transactions on Industry Applications, vol. 54, no. 2, pp. 1017–1028, 2018.

[17] J. Wang, X. Chen, and J. Xiao, “Robust optimization for power consumption strategy of commercial building considering uncertainty of environmental factors,” 2019 IEEE 3rd Conference on Energy Internet and Energy System Integration (EI2), 2019.

[18] C. Xu, D. Wang, C. Ma, R. Xu, J. Wu, T. Yu, and B. Liu, “Optimization for commercial building energy management of Multi-Energy Fusion,” 2018 IEEE 8th Annual International Conference on CYBER Technology in Automation, Control, and Intelligent Systems (CYBER), 2018.

[19] J. Yusuf and S. Ula, "Impact of Building Loads on Cost Optimization Strategy for a Plug-in Electric Vehicle Operation," 2019 IEEE Transportation Electrification Conference and Expo (ITEC), Detroit, MI, USA, 2019.

[20] J. Yusuf and S. Ula, "A Comprehensive Optimization Solution for Buildings with Distributed Energy Resources and V2G Operation in Smart Grid Applications," 2020 IEEE Power & Energy Society Innovative Smart Grid Technologies Conference (ISGT), Washington, DC, USA, 2020, pp. 1-5.

[21] M. Tavakoli, F. Shokridehaki, M. Marzband, R. Godina, and E. Pouresmaeil, “A two stage hierarchical control approach for the optimal energy

management in commercial building microgrids based on local wind power and Pevs," Sustainable Cities and Society, vol. 41, pp. 332–340, 2018.

[22] T. V. Christiaanse, R. C. G. M. Loonen, and R. Evins, "Techno-economic optimization for grid-friendly rooftop PV systems – a case study of commercial buildings in British Columbia," Sustainable Energy Technologies and Assessments, vol. 47, p. 101320, 2021.

[23] T.Y. Lee and C.L. Chen, "Effects of photovoltaic generation system on the contract capacity selection of time-of-use rate industrial users," 2007 International Conference on Intelligent Systems Applications to Power Systems, 2007.

[24] N. Wu, J. Xiao, Y. Feng, H. Bao, R. Lin, and W. Chen, "Economic Feasibility Analysis of User-Side Battery Energy Storage Based on Three Electricity Price Policies," iSPEC 2020 - Proc. IEEE Sustain. Power Energy Conf. Energy Transit. Energy Internet, no. 202008290000001, pp. 2034–2039, 2020.

[25] C. J. Meinrenken and A. Mehmani, "Concurrent optimization of thermal and electric storage in commercial buildings to reduce operating cost and demand peaks under time-of-use tariffs," Applied Energy, vol. 254, p. 113630, 2019.

[26] M. Sun, C.-L. Chang, J. Zhang, A. Mehmani, and P. Culligan, "Break-even analysis of battery energy storage in buildings considering time-of-use rates," 2018 IEEE Green Technologies Conference (GreenTech), 2018.

[27] T. A. Nguyen and R. H. Byrne, "Maximizing the cost-savings for time-of-use and net-metering customers using behind-the-meter energy storage systems," 2017 North American Power Symposium (NAPS), Morgantown, WV, 2017, pp. 1-6.

[28] Z. L. Hurwitz, Y. Dubief, and M. Almassalkhi, "Economic efficiency and carbon emissions in multi-energy systems with flexible buildings," International Journal of Electrical Power & Energy Systems, vol. 123, p. 106114, 2020.

[29] J. Yusuf, A. Hasan and S. Ula, "Impacts Analysis & Field Implementation of Plug-in Electric Vehicles Participation in Demand Response and Critical Peak Pricing for Commercial Buildings", 2021 IEEE Texas Power and Energy Conference, Austin, Texas, USA, 2021.

[30] R. A. Biroon, Z. A. Biron, and R. Hadidi, "Commercial load profile sensitivity analysis to electricity tariffs and battery characteristics," IEEE Trans. Ind. Appl., vol. 56, no. 2, pp. 1021–1030, 2020.

[31] R. A. Biroon, Z. Abdollahi, and R. Hadidi, "Effect of Tariff on Commercial Load Profile Optimization in Presence of the Battery," 2019 IEEE Ind. Appl. Soc. Annu. Meet. IAS 2019, pp. 1–8, 2019.

[32] M. Grzanic, J. M. Morales, S. Pineda, and T. Capuder, “Electricity cost-sharing in energy communities under dynamic pricing and uncertainty,” IEEE Access, pp. 1–1, 2021, [Online]. Available: https://ieeexplore.ieee.org/document/9354638/.

[33] P. Paudyal and Z. Ni, “Smart home energy optimization with incentives compensation from inconvenience for Shifting Electric Appliances,” International Journal of Electrical Power & Energy Systems, vol. 109, pp. 652–660, 2019.

[34] K. Aurangzeb, S. Aslam, S. M. Mohsin, and M. Alhussein, “A Fair Pricing Mechanism in Smart Grids for Low Energy Consumption Users,” IEEE Access, vol. 9, pp. 22035–22044, 2021.

[35] B. Alaskar, A. Alhadlaq, A. Alabdulkareem, and A. Alfadda, “On the optimality of electricity tariffs for Saudi Arabia’s residential sector considering the effect of der,” IEEE PES Innov. Smart Grid Technol. Conf. Eur., vol. 2020-October, pp. 1060–1064, 2020.

[36] N. Li, R. A. Hakvoort, and Z. Lukszo, “Segmented energy tariff design for flattening load demand profile,” IEEE PES Innov. Smart Grid Technol. Conf. Eur., vol. 2020-October, pp. 849–853, 2020.

[37] G. Connolny, "California grid warns of rotating power outages amid ‘rare and possibly fatal’ heatwave ", The Independent, September 6, 2020. [Online]. Available: https://www.independent.co.uk/news/california-heatwave-power-outage-rolling-blackout-wildfire-b404679.html [Accessed December 9, 2020]

[38] J. Llyod, " FAQ: What to Know About Flex Alerts and Power Emergencies in California", NBC Los Angeles, August 15, 2020. [Online]. Available: https://www.nbclosangeles.com/news/california-news/california-power-grid-electricity-outages-rotating-outages-blackouts-flex-alert/2413427/ [Accessed December 9, 2020] pp. 1-6.

[39] California ISO - Supply, today's outlook. [Online]. Available: https://www.caiso.com/TodaysOutlook/Pages/supply.html. [Accessed: 30-May-2022].

[40] California ISO - Final Root Cause Analysis: Mid-August 2020 Extreme Heat Wave.

[41] “U.S. Energy Information Administration - EIA - independent statistics and analysis,” Use of energy in commercial buildings in depth - U.S. Energy Information Administration (EIA). [Online]. Available: https://www.eia.gov/energyexplained/use-of-energy/commercial-buildings-in-depth.php. [Accessed: 08-May-2022].

[42] Q. Hu and F. Li, "Hardware Design of Smart Home Energy Management System With Dynamic Price Response," in IEEE Transactions on Smart Grid, vol. 4, no. 4, pp. 1878-1887, Dec. 2013, doi: 10.1109/TSG.2013.2258181.

[43] M. Manganelli, G. Greco and L. Martirano, "Design of a New Architecture and Simulation Model for Building Automation Toward Nearly Zero Energy Buildings," in IEEE Transactions on Industry Applications, vol. 55, no. 6, pp. 6999-7007, Nov.-Dec. 2019, doi: 10.1109/TIA.2019.2920233.

[44] D. T. Vedullapalli, R. Hadidi and B. Schroeder, "Combined HVAC and Battery Scheduling for Demand Response in a Building," in IEEE Transactions on Industry Applications, vol. 55, no. 6, pp. 7008-7014, Nov.-Dec. 2019, doi: 10.1109/TIA.2019.2938481.

[45] L. Martirano, E. Habib, A. Giuseppi and A. Di Giorgio, "Nearly Zero Energy Building Model Predictive Control for efficient heating," 2018 IEEE Industry Applications Society Annual Meeting (IAS), Portland, OR, 2018, pp. 1-6, doi: 10.1109/IAS.2018.8544632.

[46] M. Maasoumy and A. Sangiovanni-Vincentelli, "Total and Peak Energy Consumption Minimization of Building HVAC Systems Using Model Predictive Control," in IEEE Design & Test of Computers, vol. 29, no. 4, pp. 26-35, Aug. 2012, doi: 10.1109/MDT.2012.2200871.

[47] M. Cai, S. Ramdaspalli, M. Pipattanasomporn, S. Rahman, A. Malekpour and S. R. Kothandaraman, "Impact of HVAC Set Point Adjustment on Energy Savings and Peak Load Reductions in Buildings," 2018 IEEE International Smart Cities Conference (ISC2), Kansas City, MO, USA, 2018, pp. 1-6, doi: 10.1109/ISC2.2018.8656738.

[48] V. L. Erickson, M. Á. Carreira-Perpiñán and A. E. Cerpa, "OBSERVE: Occupancy-based system for efficient reduction of HVAC energy," Proceedings of the 10th ACM/IEEE International Conference on Information Processing in Sensor Networks, Chicago, IL, 2011, pp. 258-269.

[49] D. Zhang, S. Li, M. Sun and Z. O'Neill, "An Optimal and Learning-Based Demand Response and Home Energy Management System," in IEEE Transactions on Smart Grid, vol. 7, no. 4, pp. 1790-1801, July 2016, doi: 10.1109/TSG.2016.2552169.

[50] A. Kusiak, M. Li, and F. Tang, "Modeling and optimization of HVAC energy consumption," Applied Energy, vol. 87, no. 10, pp. 3092–3102, 2010.

[51] T. Wei, Yanzhi Wang and Q. Zhu, "Deep reinforcement learning for building HVAC control," 2017 54th ACM/EDAC/IEEE Design Automation Conference (DAC), Austin, TX, 2017, pp. 1-6, doi: 10.1145/3061639.3062224.

[52] T. Wei, S. Ren and Q. Zhu, "Deep Reinforcement Learning for Joint Datacenter and HVAC Load Control in Distributed Mixed-Use Buildings," in IEEE Transactions on Sustainable Computing, doi: 10.1109/TSUSC.2019.2910533.

[53] Z. Zhang, A. Chong, Y. Pan, C. Zhang, S. Lu, K. P. Lam, "A Deep Reinforcement Learning Approach to Using Whole Building Energy Model For HVAC Optimal Control", 2018 Building Performance Modeling Conference and SimBuild co-organized by ASHRAE and IBPSA-USA, Chicago, IL, September 26-28, 2018.

[54] Center for Sustainable Systems, University of Michigan. 2021. "U.S. Energy Storage Factsheet." Pub. No. CSS15-17.

[55] "Battery storage in the United States: An update on market trends." [Online]. Available: https://www.eia.gov/analysis/studies/electricity/batterystorage/pdf/battery_storage.pdf. [Accessed: 09-May-2022].

[56] 2019. Grid Scale Battery Storage: Frequently Asked Questions, National Renewable Energy Laboratory.

[57] A. Oudalov, T. Buehler and D. Chartouni, "Utility Scale Applications of Energy Storage," 2008 IEEE Energy 2030 Conference, Atlanta, GA, USA, 2008, pp. 1-7, doi: 10.1109/ENERGY.2008.4780999.

[58] Y. Zhang et al., "Grid-Level Application of Electrical Energy Storage: Example Use Cases in the United States and China," in IEEE Power and Energy Magazine, vol. 15, no. 5, pp. 51-58, Sept.-Oct. 2017.

[59] A. Castillo and D. F. Gayme, "Grid-scale energy storage applications in renewable energy integration: A survey," Energy Conversion and Management, vol. 87, pp. 885–894, 2014.

[60] D. M. Davies, M. G. Verde, O. Mnyshenko, Y. R. Chen, R. Rajeev, Y. S. Meng, and G. Elliott, "Combined economic and technological evaluation of battery energy storage for grid applications," Nature Energy, vol. 4, no. 1, pp. 42–50, 2018.

[61] R. Carnegie, D. Gotham, D. Nderitu, and P. V. Preckel, "Utility Scale Energy Storage Systems Benefits, Applications, and Technologies," Jun. 2013.

[62] S. Moazeni, W. B. Powell and A. H. Hajimiragha, "Mean-Conditional Value-at-Risk Optimal Energy Storage Operation in the Presence of Transaction Costs," in IEEE Transactions on Power Systems, vol. 30, no. 3, pp. 1222-1232, May 2015.

[63] R. Barzin, J. J. J. Chen, B. R. Young, and M. M. Farid, "Peak load shifting with energy storage and price-based control system," Energy, vol. 92, pp. 505–514, 2015.

[64] P. L. Denholm, J. Nunemaker, W. J. Cole, and P. J. Gagnon, “The Potential for Battery Energy Storage to Provide Peaking Capacity in the United States,” 2019.

[65] S. Chen, T. Zhang, H. B. Gooi, R. D. Masiello and W. Katzenstein, "Penetration Rate and Effectiveness Studies of Aggregated BESS for Frequency Regulation," in IEEE Transactions on Smart Grid, vol. 7, no. 1, pp. 167-177, Jan. 2016.

[66] Z. Wu, D. W. Gao, H. Zhang, S. Yan and X. Wang, "Coordinated Control Strategy of Battery Energy Storage System and PMSG-WTG to Enhance System Frequency Regulation Capability," in IEEE Transactions on Sustainable Energy, vol. 8, no. 3, pp. 1330-1343, July 2017.

[67] C. K. Das, T. S. Mahmoud, O. Bass, S. M. Muyeen, G. Kothapalli, A. Baniasadi, and N. Mousavi, “Optimal sizing of a utility-scale energy storage system in transmission networks to improve frequency response,” Journal of Energy Storage, vol. 29, p. 101315, 2020.

[68] I. Beil, A. Allen, A. Tokombayev and M. Hack, "Considerations when using utility-scale battery storage to black start a gas turbine generator," 2017 IEEE Power & Energy Society General Meeting, Chicago, IL, USA, 2017, pp. 1-5.

[69] J. Hu, M. R. Sarker, J. Wang, F. Wen, and W. Liu, “Provision of flexible ramping product by battery energy storage in day-ahead energy and reserve markets,” IET Generation, Transmission & Distribution, vol. 12, no. 10, pp. 2256–2264, 2018.

[70] R. van Haaren, M. Morjaria, and V. Fthenakis, “An energy storage algorithm for ramp rate control of utility scale PV (photovoltaics) plants,” Energy, vol. 91, pp. 894–902, 2015.

[71] A. Shahmohammadi, R. Sioshansi, A. J. Conejo, and S. Afsharnia, “The role of energy storage in mitigating ramping inefficiencies caused by variable renewable generation,” Energy Conversion and Management, vol. 162, pp. 307–320, 2018.

[72] 2019. Innovation landscape brief: Utility-scale batteries, International Renewable Energy Agency.

[73] R. Xiong, R. Yang, Z. Chen, W. Shen and F. Sun, "Online Fault Diagnosis of External Short Circuit for Lithium-Ion Battery Pack," in IEEE Transactions on Industrial Electronics, vol. 67, no. 2, pp. 1081-1091, Feb. 2020.

[74] W. Gao, Y. Zheng, M. Ouyang, J. Li, X. Lai and X. Hu, "Micro-Short-Circuit Diagnosis for Series-Connected Lithium-Ion Battery Packs Using Mean-Difference Model," in IEEE Transactions on Industrial Electronics, vol. 66, no. 3, pp. 2132-2142, March 2019.

[75] X. Kong, Y. Zheng, M. Ouyang, L. Lu, J. Li, and Z. Zhang, “Fault diagnosis and quantitative analysis of micro-short circuits for lithium-ion batteries in battery packs,” Journal of Power Sources, vol. 395, pp. 358–368, 2018.

[76] M. M. Kiani, "Online detection of faulty battery cells in energy storage systems via impulse response method," 2011 IEEE Vehicle Power and Propulsion Conference, Chicago, IL, USA, 2011, pp. 1-6.

[77] Z. Song, F. P. Delgado, J. Hou, H. Hofmann and J. Sun, "Individual Cell Fault Detection for Parallel-Connected Battery Cells Based on the Statistical Model and Analysis," 2020 American Control Conference (ACC), Denver, CO, USA, 2020, pp. 1155-1160.

[78] H. Akhavan-Hejazi, Z. Taylor, and H. Mohsenian-Rad, “Optimal cell removal to enhance operation of aged grid-tied battery storage systems,” IEEE Transactions on Sustainable Energy, vol. 12, no. 1, pp. 739–742, 2021.

[79] Electropaedia: Battery and Energy Technologies, “State of Charge (SOC) Determination”. [Online] . Available: https://www.mpoweruk.com/soc.htm

[80] M. Ismail, R. Dlyma, A. Elrakaybi, R. Ahmed, S. Habibi, “Battery state of charge estimation using an Artificial Neural Network”, 2017 IEEE Transportation Electrification Conference and Expo (ITEC), June 2017.

[81] S. Tong, J. H. Lacap, J. W. Park, “Battery state of charge estimation using a load-classifying neural network”, Journal of Energy Storage, Volume 7, August 2016.

[82] C. H. Cai, D. Du, Z. Y. Liu, H. Zhang, “Artificial neural network in estimation of battery state of-charge (SOC) with nonconventional input variables selected by correlation analysis”, International Conference on Machine Learning and Cybernetics, Nov. 2002.

[83] X. Liu, D. Liu, Y. Zhang, Q. Wang, H. Wang, F. Zhang, “Least squares support vector machine based lithium battery capacity prediction”, 2014 International Conference on Mechatronics and Control (ICMC), July 2014.

[84] H. Sheng, J. Xiao, “Electric vehicle state of charge estimation: Nonlinear correlation and fuzzy support vector machine”, Journal of Power Sources, Volume 281, 1 May 2015.

[85] P. H. Michel, V. Heiries, “An Adaptive Sigma Point Kalman Filter Hybridized by Support Vector Machine Algorithm for Battery SoC and SoH Estimation”, 2015 IEEE 81st Vehicular Technology Conference (VTC Spring), May 2015.

[86] J. Du, Z. Liu and Y. Wang, “State of charge estimation for Li-ion battery based on model from extreme learning machine”, Control Engineering Practice, Volume 26, May 2014.

[87] A. Densmore, M. Hanif, “Determining battery SoC using Electrochemical Impedance Spectroscopy and the Extreme Learning Machine”, 2015 IEEE 2nd International Future Energy Electronics Conference (IFEEC), Nov. 2015.

[88] C. S. Chin, Z. Gao, “State-of-Charge Estimation of Battery Pack under Varying Ambient Temperature Using an Adaptive Sequential Extreme Learning Machine”, Energies 2018.

[89] C. Hu, G. Jain, P. Zhang, C. Smidt, P. Gomadam, T. Gorka, “Data-driven method based on particle swarm optimization and k-nearest neighbor regression for estimating capacity of lithium-ion battery”, Applied Energy, Volume 129, 15 September 2014.

[90] NCSS Statistical Software Documentation, “Chapter 335: Ridge Regression”. [Online]. Available: https://www.ncss.com/wp-content/themes/ncss/pdf/Procedures/NCSS/Ridge_Regression.pdf

[91] Statistics How To, “Lasso Regression”. [Online]. Available: https://www.statisticshowto.datasciencecentral.com/lasso-regression/

[92] “U.S. Department of Energy Combined Heat and power and microgrid installation databases,” U.S. Department of Energy Combined Heat & Power and Microgrid Installation Databases. [Online]. Available: https://doe.icfwebservices.com/microgrid. [Accessed: 09-May-2022].

[93] “Sacramento Municipal Utility District Microgrid Demonstration Project” [Online]. Available: https://www.smud.org/-/media/Documents/Corporate/About-Us/Energy-Research-and-Development/research-microgrid-demonstration-project.ashx. [Accessed: 10-May-2022].

[94] W. Feng, M. Jin, X. Liu, Y. Bao, C. Marnay, C. Yao, and J. Yu, “A review of microgrid development in the United States – A decade of progress on policies, demonstrations, controls, and software tools,” Applied Energy, vol. 228, pp. 1656–1668, 2018.

[95] California Energy Commission, “Borrego Springs: California's first renewable energy- based community microgrid,” California Energy Commission. [Online]. Available: https://www.energy.ca.gov/publications/2019/borrego-springs-californias-first-renewable-energy-based-community-microgrid. [Accessed: 09-May-2022].

[96] “Welcome to Alcatraz: One of the largest microgrids in the United States,” Energy.gov. [Online]. Available: https://www.energy.gov/eere/articles/welcome-alcatraz-one-largest-microgrids-united-states. [Accessed: 09-May-2022].

[97] T. Lehtola and A. Zahedi, "Vehicle to grid system in frequency regulation for securing electricity network stability," 2015 IEEE PES Asia-Pacific Power and Energy Engineering Conference (APPEEC), Brisbane, QLD, 2015, pp. 1-4.

[98] T. Ersal, C. Ahn, I. A. Hiskens, H. Peng and J. L. Stein, "Impact of controlled plug-in EVs on microgrids: A military microgrid example," 2011 IEEE Power and Energy Society General Meeting, Detroit, MI, USA, 2011, pp. 1-7.

[99] M. Jun and A. J. Markel, "Simulation and analysis of vehicle-to-Grid operations in microgrid," 2012 IEEE Power and Energy Society General Meeting, San Diego, CA, 2012, pp. 1-5.

[100] P. A. Mendoza-Araya, P. J. Kollmeyer and D. C. Ludois, "V2G integration and experimental demonstration on a lab-scale microgrid," 2013 IEEE Energy Conversion Congress and Exposition, Denver, CO, 2013, pp. 5165-5172.

[101] M. A. Masrur et al., "Military-Based Vehicle-to-Grid and Vehicle-to-Vehicle Microgrid—System Architecture and Implementation," in IEEE Transactions on Transportation Electrification, vol. 4, no. 1, pp. 157-171, March 2018.

[102] R. Villafáfila-Robles et al., "Electric vehicles in power systems with distributed generation: Vehicle to Microgrid (V2M) project," 11th International Conference on Electrical Power Quality and Utilisation, Lisbon, 2011, pp. 1-6.

[103] J. Cho, H. Kim, Y. Cho, H. Kim and J. Kim, "Demonstration of a DC Microgrid with Central Operation Strategies on an Island," 2019 IEEE Third International Conference on DC Microgrids (ICDCM), Matsue, Japan, 2019, pp. 1-5.

[104] T. Gabderakhmanova et al., "Demonstrations of DC Microgrid and Virtual Power Plant Technologies on the Danish Island of Bornholm," 2020 55th International Universities Power Engineering Conference (UPEC), Torino, Italy, 2020, pp. 1-6.

[105] J. Yusuf, A. S. M. J. Hasan and S. Ula, "Impacts of Plug-in Electric Vehicles on a Distribution Level Microgrid," 2019 North American Power Symposium (NAPS), 2019, pp. 1-6, doi: 10.1109/NAPS46351.2019.9000195.

[106] “REopt Lite: REopt Energy Integration & Optimization,” NREL. [Online]. Available: https://reopt.nrel.gov/tool. [Accessed: 16-Mar-2021].

[107] System Advisor Model Version 2020.11.29 (SAM 2020.11.29). National Renewable Energy Laboratory. Golden, CO. Accessed December 27, 2020. https://sam.nrel.gov.

[108] “BU-802b: What does Elevated Self-discharge Do?,” Elevating Self-discharge - Battery University. [Online]. Available:

https://batteryuniversity.com/learn/article/elevating_self_discharge. [Accessed: 13-Mar-2021].

[109] Michael Grant and Stephen Boyd. CVX: Matlab software for disciplined convex programming, version 2.0 beta. http://cvxr.com/cvx, September 2013.

[110] Eia.gov. 2017. CBECS 2012: Trends In Lighting In Commercial Buildings. [online] Available at: <https://www.eia.gov/consumption/commercial/reports/2012/lighting/> [Accessed 12 July 2020].

[111] Carrier Air Conditioning Company. 1965a. Handbook of Air Conditioning System Design, pp 1-99 to 1-100. New York: McGraw Hill

[112] Carrier Air Conditioning Company. 1965b. Handbook of Air Conditioning System Design, pp 1-100, Table # 48. New York: McGraw Hill.

[113] Engineering ToolBox, (2004). Met - Metabolic Rate. [online] Available at: https://www.engineeringtoolbox.com/met-metabolic-rate-d_733.html [Accessed 12 July 2020].

[114] K. Ouyang and F. Haghighat, "A procedure for calculating thermal response factors of multi-layer walls—State space method," Building and Environment, vol. 26, no. 2, pp. 173–177, 1991.

[115] D. C. Hittle and R. Bishop, "An improved root-finding procedure for use in calculating transient heat flow through multilayered slabs," International Journal of Heat and Mass Transfer, vol. 26, no. 11, pp. 1685–1693, 1983.

[116] Engineering ToolBox, (2004). Transmission Heat Loss through Building Elements. [online] Available at: https://www.engineeringtoolbox.com/heat-loss-transmission-d_748.html [Accessed 12 July 2020].

[117] Wikipedia contributors, 'Heat transfer coefficient', Wikipedia, The Free Encyclopedia, 14 June 2020, 22:35 UTC, <https://en.wikipedia.org/w/index.php?title=Heat_transfer_coefficient&oldid=962585129> [Accessed 12 July 2020]

[118] ASHRAE. 2001. Handbook of Fundamentals, pp 29.8-29.13, Atlanta: ASHRAE.

[119] Gurobi. 2020. Non-Convex Quadratic Optimization - Gurobi. [online] Available at: <https://www.gurobi.com/resource/non-convex-quadratic-optimization/> [Accessed 12 July 2020].

[120] 2020. Electric Power Monthly. U.S. Energy Information Administration.

[121] 2017. Identifying Potential Markets For Behind-The-Meter Battery Energy Storage: A Survey Of U.S. Demand Charges. National Renewable Energy Laboratory.

[122] Eia.gov. 2020. Frequently Asked Questions (Faqs) - U.S. Energy Information Administration (EIA). [online] Available at: <https://www.eia.gov/tools/faqs/faq.php?id=74&t=11#:~:text=In%202018%2C%20total%20U.S.%20electricity,of%20CO2%20emissions%20per%20kWh.> [Accessed 12 July 2020].

[123] A. Leon-Garcia, "The probability density function," in Probability, statistics, and random processes for electrical engineering, 3rd ed., Upper Saddle River, NJ: Pearson Prentice Hall, Pearson Education International, 2016.

[124] R. B. D'agostino, A. Belanger, and R. B. D'agostino, "A Suggestion for Using Powerful and Informative Tests of Normality," The American Statistician, vol. 44, no. 4, pp. 316–321, 1990.

[125] X. Hu, K. Zhang, K. Liu, X. Lin, S. Dey and S. Onori, "Advanced Fault Diagnosis for Lithium-Ion Battery Systems: A Review of Fault Mechanisms, Fault Features, and Diagnosis Procedures," in IEEE Industrial Electronics Magazine, vol. 14, no. 3, pp. 65-91, Sept. 2020.

[126] K. Mongird, V. V. Viswanathan, P. J. Balducci, M. J. Alam, V. Fotedar, V. S. Koritarov, and B. Hadjerioua, "Energy Storage Technology and Cost Characterization Report," 2019.

[127] T. Hastie, R. Tibshirani, J. Friedman, "The Elements of Statistical Learning: Data Mining, Inference and Prediction", 2nd edition, Springer, 2017.

[128] UFLDL Tutorial, "Multi-Layer Neural Network". [Online]. Available: http://ufldl.stanford.edu/tutorial/supervised/MultiLayerNeuralNetworks/

[129] Computational complexity of machine learning algorithms, The Kernel Trip. (2018). https://www.thekerneltrip.com/machine/learning/computational-complexity-learning-algorithms/ (accessed June 11, 2022).

[130] Supporting vector machine, why if C is large the training error ..., (n.d.). https://www.researchgate.net/post/Supporting-vector-machine-why-if-C-is-large-the-training-error-decrease-but-the-test-error-increase (accessed June 11, 2022).

[131] S. Ula, J. Yusuf, A. S. M. J. Hasan, " Development and Deployment of an Integrated Microgrid Incorporating Solar PV, Battery Energy Storage and EV Charging," Conference Proceedings of MIT Applied Energy Symposium: A+B, Boston, MA, USA, 2019.

[132] "IEEE Guide for Electric Power Distribution Reliability Indices," in IEEE Std 1366-2012 (Revision of IEEE Std 1366-2003) , vol., no., pp.1-43, 31 May 2012.

[133] ANNUAL SYSTEM RELIABILITY REPORT. (2019). Southern California Edison.

[134] ELECTRIC SYSTEM RELIABILITY ANNUAL REPORT 2019. (2019). San Diego Gas and Electric.

[135] 2019 ANNUAL ELECTRIC RELIABILITY REPORT. (2019). Pacific Gas and Electric.